Dynamical flows through dark matter haloes - II. One- and two-point statistics at the virial radius

Laurence Voutquenne-Nazabadioko, Christophe Pichon

Mon. Not. R. Astron. Soc. **374,** 877–909 (2007) doi:10.1111/j.1365-2966.2006.11203.x

Dynamical flows through dark matter haloes – II. One- and two-point statistics at the virial radius

Dominique Aubert[1,2,3]★ and Christophe Pichon[1,3]

[1]*Observatoire Astronomique de Strasbourg, 11 rue de l'Universite, 67000 Strasbourg, France*
[2]*Service d'Astrophysique, CEA Saclay, 91191 Gif-Sur-Yvette, France*
[3]*Institut d'Astrophysique de Paris, 98 bis boulevard Arago, 75014 Paris, France*

Accepted 2006 October 12. Received 2006 October 9; in original form 2006 July 23

ABSTRACT

In a series of three papers, the dynamical interplay between environments and dark matter haloes is investigated, while focusing on the dynamical flows through the virtual virial sphere. It relies on both cosmological simulations, to constrain the environments, and an extension to the classical matrix method to derive the responses of the halo. A companion paper (Paper I) showed how perturbation theory allows us to propagate the statistical properties of the environment to an ensemble description of the dynamical response of the embedded halo. The current paper focuses on the statistical characterization of the environments surrounding haloes, using a set of large-scale simulations; the large statistic of environments presented here allows us to put quantitative and statistically significant constrains on the properties of flows accreted by haloes.

The description chosen in this paper relies on a 'fluid' halocentric representation. The interactions between the halo and its environment are investigated in terms of a time-dependent external tidal field and a source term characterizing the infall. The former accounts for fly bys and interlopers. The latter stands for the distribution function of the matter accreted through the virial sphere. The method of separation of variables is used to decouple the temporal evolution of these two quantities from their angular and velocity dependence by means of projection on a 5D basis.

It is shown that how the flux densities of mass, momentum and energy can provide an alternative description to the 5D projection of the source. Such a description is well suited to regenerate synthetic time lines of accretion which are consistent with environments found in simulations as discussed in the Appendix. The method leading to the measurements of these quantities in simulations is presented in detail and applied to 15 000 haloes, with masses between 5×10^{12} and $10^{14}\,\mathrm{M}_{\odot}$ evolving between $z = 1$ and 0. The influence of resolution, class of mass, and selection biases are investigated with higher resolution simulations. The emphasis is put on the one- and two-point statistics of the tidal field, and of the flux density of mass, while the full characterization of the other fields is postponed to Paper III.

The net accretion at the virial radius is found to decrease with time. This decline results from both an absolute decrease of infall and a growing contribution of outflows. Infall is found to be mainly radial and occurring at velocities $\sim$0.75 times the virial velocity. Outflows are also detected through the virial sphere and occur at lower velocities $\sim 0.6 V_{\mathrm{c}}$ on more circular orbits. The external tidal field is found to be strongly quadrupolar and mostly stationary, possibly reflecting the distribution of matter in the halo's near environment. The coherence time of the small-scale fluctuations of the potential hints a possible anisotropic distribution of accreted satellites. The flux density of mass on the virial sphere appears to be more clustered

★E-mail: aubert@astro.u-strasbg.fr

than the potential, while the shape of its angular power spectrum seems stationary. Most of these results are tabulated with simple fitting laws and are found to be consistent with published work, which rely on a description of accretion in terms of satellites.

Key words: methods: *N*-body simulations – galaxies: formation – galaxies: kinematics and dynamics.

1 GALAXIES IN THEIR ENVIRONMENT

Examples of galaxies interacting with their environments are numerous. The Antennae, the Cartwheel Galaxy and M51 are among the most famous ones. One of our closest neighbours, M31, exhibits a giant stellar stream which may be associated with its satellites (e.g. McConnachie et al. 2003). Even the Milky Way shows relics of past interactions with material coming from the outskirts, such as the Sagittarius dwarf (Ibata, Gilmore & Irwin 1995). It appears clearly that the evolution of galactic systems cannot be understood only by considering their internal properties but also by taking into account their environment. From a dynamical point of view, it is still not clear, for example, if spirals in galaxies are induced by intrinsic unstable modes (e.g. Lynden-Bell & Kalnajs 1972; Kalnajs 1977) or if they are due to gravitational interactions with satellites or other galaxies (e.g. Toomre & Toomre 1972). Similarly, normal mode theories of warps have been proposed (Hunter & Toomre 1969; Sparke & Casertano 1988) but failed to reproduce long-lived warps in a live halo for example (e.g. Binney, Jiang & Dutta 1998). Since warped galaxies are likely to have companions (Reshetnikov & Combes 1998), it is natural to suggest satellite tidal forcing as a generating mechanism (e.g. Weinberg 1998; Tsuchiya 2002). Another possibility is angular momentum misalignment of infalling material (e.g. Ostriker & Binney 1989; Jiang & Binney 1999). The existence of the thick disc may also be explained by past small mergers (e.g. Quinn et al. 1993; Walker, Mihos & Hernquist 1996; Velazquez & White 1999). Conversely, very thin discs put serious constraints on the amplitude of the interactions they may have experienced in the past.

On a larger scale, dark matter haloes are built in a hierarchical fashion within the cold dark matter (CDM) model. Some of the most serious challenges these models are now facing – the overproduction of dwarf galaxies in the Local Group (e.g. Klypin et al. 1999; Moore et al. 1999), the cuspide crisis of Navarro–Frenk–White (NFW)-like haloes (e.g. Flores & Primack 1994; Moore 1994), the overcooling problem and the momentum crisis for galactic discs (e.g. Navarro & Steinmetz 1997) – occur at these scales; it is therefore important to study the effects of the cosmological paradigm on the evolution of galaxies in order to address these issues.

In fact, the properties of galaxies naturally present correlations with their environments. For example, Tormen (1997) showed that the shape of haloes tends to be aligned with the distribution of surrounding satellites. Also, the halo's spin is sensitive to recently accreted angular momentum (e.g. van Haarlem & van de Weygaert 1993; Aubert, Pichon & Colombi 2004). More generally, haloes inherit the properties of their progenitors.

At this point, a question naturally arises; 'what is the dynamical response of a galactic system (halo + disc) to its environment?'. One way to address this issue is to compute high-resolution simulations of galaxies into a given environment (e.g. Abadi et al. 2003; Gill et al. 2004; Knebe et al. 2004). However, if one is interested in reproducing the variety of dynamical responses of galaxies to various environments, the use of such simulations becomes rapidly tedious. An alternative way to investigate this topic is presented here, which should complement both high-resolution simulations and large cosmological simulations. In a series of three papers, a hybrid approach is presented to investigate the interplay between environments and haloes. It relies on both cosmological simulations (to constrains the environments) and a straightforward extension of the classical tools of galactic dynamics (to derive the haloes' response). A companion paper (Pichon & Aubert 2006, hereafter Paper I) describes the analytic theory which allows us to assess the dynamics of haloes in the open, secular and non-linear regimes. The purpose of the current paper is to set out a framework in which to describe statistically the environments of haloes and present results on the tidal field and the flux density of matter. Paper III (Aubert & Pichon, in preparation) will conclude the complete description of the environments of dark haloes.

1.1 Galactic infall as a cosmic boundary

Clearly, a number of problems concerning galactic evolution can only be tackled properly via a detailed statistical investigation. Let us briefly make an analogy to the cosmological growth of density fluctuations. Under certain assumptions, one can solve the equations of evolution of those overdensities in an expanding universe (e.g. Peebles 1980, see Bernardeau et al. 2002 for an extensive review). Their statistical evolution due to gravitational clustering follows, given the statistical properties of the initial density field. For example, the power spectrum, $P(z, k)$, may be computed for various primordial power spectra, $P_{\rm prim}(k)$, and for various cosmologies. In other words, the statistical properties of the initial conditions are *propagated* to a given redshift through an operator $\aleph$ given by the non-linear dynamical equations of the clustering:

$$P(z, k) = \aleph(P_{\rm prim}(k), z). \quad (1)$$

In a similar way, how would the statistical properties of environments be propagated to the dynamical properties of galactic systems? This is clearly a daunting task: the previous analogy with the cosmological growth of perturbation is restricted to its principle. For example, the assumption of a uniform and cold initial state cannot be sustained for galaxies and haloes. While spatial isotropy is clearly not satisfied by discs, and hot, possibly triaxial haloes, the velocity tensor of galaxies may also be anisotropic. Environments also share these inhomogeneous and anisotropic features since they are also the product of gravitational clustering and cannot be simply described as Gaussian fields. These boundary conditions are not pure 'initial conditions' since they evolve with time and in a non-stationary manner (e.g. the accretion rate decreases with time). A whole range of mass must be taken into account, each with different statistical properties. Finally, trajectories cannot be considered as ballistic (even in the linear regime) and must be integrated over long periods. Notwithstanding the above specificities of the galactic framework, two questions have to be answered.

(i) What is the 'galactic' equivalent of $P_{\rm prim}(k)$, i.e. how does one describe statistically the boundary conditions?

(ii) What is the 'galactic' equivalent of $\aleph$, i.e. how does one describe the inner galactic dynamics?

The second point is discussed extensively in Paper I and is briefly summarized in Section 2. In that paper, it is shown how a perturbative theory can describe the dynamics of haloes which experience both accretion and tidal interactions (see also Aubert et al. 2004). Within this formalism, the environment is described by the external gravitational potential and a source function. The former describes fly bys and the tidal field of neighbouring large-scale structures. The latter describes the flows of dark matter, i.e. the exchanges of material between the halo and the 'interhalo' mediums. The knowledge of these two quantities fully characterizes the boundary condition. The focus here is on well-formed haloes which do not undergo major merger between $z = 1$ and 0. This bias is consistent with a galactocentric description in which a perturbative description of the inner dynamics is appropriate and equal mass mergers are explicitly ignored. As briefly explained in Section 2, this formalism provides a link between the statistical properties of environments to the statistical distributions of the responses of haloes: this link is referred to as statistical propagation. In this manner, the distribution of haloes' dynamical state can be directly inferred from the statistical properties of environments, without relying on the follow up of individual interacting haloes. The observed distributions of dynamical features provide information on the cosmic boundaries which influence haloes. This, together with the perturbative formalism described in Paper I, should allow us to address statistically the recurrent 'nurture or nature' problem of structure formation within galactic systems.

This statistical formalism is complementary to methods based on merger trees (which also couple environment and inner properties of galactic systems; see e.g. Kauffmann & White 1993; Roukema et al. 1997; Somerville & Kolatt 1999). These 'analytic' or 'semi-analytic' models, with prescription for the baryons contained in haloes, angular momentum transfer, cooling and star formation, may predict properties of galaxies given in their formation history (e.g. Cole et al. 1994). This history may be provided analytically using extended Press–Schechter formalism (see e.g. Bond et al. 1991; Lacey & Cole 1993) or using simulations (e.g. Kauffmann et al. 1999; Benson et al. 2001). Even though this technique now extends its field of application to subhaloes (see e.g. Blaizot et al. 2006), it remains somewhat limited for the purpose of dynamical applications. These require a detailed description of the geometrical configuration of the perturbations, and of the dynamical response of the halo. Both of these are difficult to reduce to simple recipes. Conversely, full analytic theories of the inner dynamics of interacting haloes were developed in e.g. Tremaine & Weinberg (1984), Weinberg (1998) and Murali (1999). Relying on the matrix method, these theories do take properly into account the resonant processes that occur when the halo is perturbed by an external potential. However, they usually do not account for the perturbations induced by the accretion of matter, while these authors generally considered test cases where a halo responds to a given configuration (or statistics; see e.g. Weinberg 2001) of perturbations. Paper I extended these theories to open stellar systems and, while relying on numerical simulations to constrain the environments, it reformulated them in terms of the statistics of the inner dynamics of a representative population of haloes.

Paper I presents a list of possible applications. For instance, gravitational lensing by haloes is affected by inner density fluctuations, which are induced by the halo's environment: hence the statistics of the lensing signal are be related to the statistics of halo's perturbations, therefore to the cosmological growth of structures. Paper I showed how this approach could be extended to other observables, such as X-ray temperature maps, SZ surveys or direct detection of dark matter. Statistical propagation allows us to relate cosmology to the inner properties of cluster and galaxies. Conversely, it should be possible to show if the perturbations measured in simulations are consistent with a secular drift towards a universal profile of haloes. Closer to us, the correlation of the numerous artefacts of past accretion in the Local Group, such as streams or tidal tails, can be understood in terms of statistics of environments. All processes which depend critically on the geometry of the interactions may be tackled in this framework.[1]

The statistical propagation relies on the knowledge of the properties of the environment and is stated by the point (i) mentioned above. This question is investigated the current paper by using a large set of simulations, where each halo provides a realization of the environment. From this large ensemble of interacting haloes, the aim is to extract the global properties of their 'cosmic neighbourhood'. Such a task requires an appropriate description of the source and the surrounding tidal field. It is the purpose of this work to implement this description which should both provide insights on the generic properties of cosmic environments and be useful in a 'dynamical' context. Specifically, a method is presented to constrain the exchanges between the halo and its neighbourhood, via the properties of accretion and potential measured on the virial sphere. The advantages, specificities and caveats (and the methods implemented to overcome them) provided by this *halocentric* approach will be presented in this paper.

As shown in the following sections, the source function is given by the phase-space distribution function (DF hereafter) of the advected material. As a consequence, its full characterization is a complex task since it involves sampling a five-dimensional space and relies on the projection of its DF on a suitable 5D basis. In particular, it is shown that how such a description can be used to constrain the kinematic properties of accretion by dark matter haloes in cosmological simulations. The detailed statistical characterization of the higher moments of the source is postponed to Paper III. An alternative description of the source is also presented; it relies on flux densities through the virial sphere, i.e. the moments of the source DF. Even though it is less suited to the dynamical propagation, this alternative description is easier to achieve numerically and to interpret physically. In particular, it illustrates how the source term may be characterized statistically via its moments. The link between these flux densities and the 5D projection of the source is discussed together with the one- and two-point statistics of the flux densities of mass through haloes in simulations. Also, the mean of reprojecting the effect of the external gravitational potential inside the halo (through Gauss's theorem) while knowing its properties on the virial sphere is discussed. The potential's one- and two-point statistics are also investigated around simulated haloes and interpreted.

Finally, Appendix F provides means of regenerating such flows *ab initio* from its tabulated statistical properties. Such tools yield a way to embed idealized simulations of galaxies into realistic cosmological environments.

[1] However, all departure to angular isotropy on the sphere will be ignored here (in contrast to what was stressed in Aubert et al. 2004), and its implications will be postponed to the discussions in Section 8.

The outline of the paper is as follows. Section 2 presents briefly the dynamics of open collisionless systems and states the principle of statistical propagation. Section 3 presents the procedure used to compute the source term, and illustrates its implementation on a given halo. The simulations and the corresponding selection biases of our sample are then described in Section 4.2. Sections 5 and 6 present the statistical measurements for one- and two-point statistics, respectively. Section 7 draws a global picture of galactic infall on $L^\star$ galaxies, while a discussion and conclusions follow in Section 8.

Among the different results described in this paper, the reader will find the following.

(i) A statistical description of the external gravitational field felt by haloes: the potential is found to be quadrupolar and stationary.

(ii) A study of the evolution of accretion: accretion by dark matter haloes decreases with time, while the outflows become more significant at recent times.

(iii) Constrains on the trajectory of infalling material: accretion is found to be essentially radial, while outflows are found to be more circular.

(iv) Results on the two-point statistics of the external potential measured on the viral sphere: the potential provides hints of an anisotropic perturbation of the halo.

(v) Results on the two-point statistics of the accretion's distribution on the virial sphere: accretion is dominated by small-scale fluctuations and has a shorter coherence than the external gravitational field.

2 DYNAMICS OF OPEN COLLISIONLESS SYSTEMS

The exchanges occurring between a halo and its environment can be characterized in several ways. One of the classical method involves building a merger tree where the whole history of formation of a halo is expressed in terms of global properties of its progenitors (e.g. Kauffmann & White 1993; Lacey & Cole 1993; Somerville & Kolatt 1999). While well suited to study the evolution of those characteristics, it cannot be directly applied to predict in detail the haloes' inner dynamic because of the lack of spatial information on these interactions. One could track the whole (six-dimensional) phase-space history of all the progenitors, but not only would it be difficult to store in practice it would also not give information on the influence of large-scale structures through their gravitational potential. In the present paper, following Aubert et al. (2004), it is suggested to measure the relevant quantities on a surface at the interface between the halo and the intergalactic medium. Accretion is described as a flux of particles through the haloes' external boundaries.

This section presents an extension of the formalism developed by e.g. Tremaine & Weinberg (1984) and Murali (1999) to open spherical collisionless systems. The dynamics of a dark matter spherical halo is obtained by solving the collisionless Boltzmann equation coupled with the Poisson equation

$$\partial_t F + \boldsymbol{v}\cdot\partial_{\boldsymbol{r}} F - \nabla\Psi\cdot\partial_{\boldsymbol{v}} F = 0, \tag{2}$$

$$\Delta\Psi = 4\pi G\int \mathrm{d}^3 v F(\boldsymbol{v}), \tag{3}$$

where $F(\boldsymbol{r}, \boldsymbol{v}, t)$ is the system's DF coupled to $\Psi(\boldsymbol{r}, t)\equiv\psi+\psi_{\rm e}$, the total gravitational potential (self-gravitating + external perturbation). Note that, in a somewhat unconventional manner, $\psi^{\rm e}$ refers here to the external potential, i.e. the tidal potential created by the perturbations *outside* the boundary. The gravitational field of incoming particles is accounted for by the source term. Equation (2) coupled with Hamilton's equations is a conservation equation

$$\partial_t F + \tilde{\nabla}(\boldsymbol{u}F) = 0, \tag{4}$$

where $\boldsymbol{u}\equiv(\boldsymbol{v}, -\nabla\Psi)$ and $\tilde{\nabla}\equiv(\partial_{\boldsymbol{r}}, \partial_{\boldsymbol{v}})$. As a consequence, considering a 'source of material' described by $f_{\rm e}(\boldsymbol{w})$ located on a surface $S(\boldsymbol{w})$ implies

$$\partial_t F + \tilde{\nabla}(\boldsymbol{u}F) = -\delta_{\rm D}[S(\boldsymbol{w})-a]\boldsymbol{u}\cdot\frac{\nabla S}{|\nabla S|} f_{\rm e}(\boldsymbol{w}), \tag{5}$$

where $\boldsymbol{w}\equiv(\boldsymbol{r}, \boldsymbol{v})$ describes the phase space and a defines the surface boundary of the studied system (here $\delta_{\rm D}$ stands for the Dirac delta function). If this boundary is defined as a spherical surface with radius R, then equation (5) becomes (e.g. Appel 2002)

$$\partial_t F + \tilde{\nabla}(\boldsymbol{u}F) = -\delta_{\rm D}(r-R)v_{\rm r} f_{\rm e}(\boldsymbol{w}) \tag{6}$$

$$\equiv -\delta_{\rm D}(r-R)s^{\rm e}(\boldsymbol{w}). \tag{7}$$

The function $s^{\rm e}$ will be hereafter referred to as the 'source' function. Formally, the right-hand side of equation (7) can be seen as an additional local rate of change of the system's DF. Note that equation (7) involves the external potential, $\psi^{\rm e}$, via $\boldsymbol{u}$.

2.1 Moments of the source term

Integrating equation (7) over velocities leads to the mass conservation relation

$$\partial_t\rho + \nabla(\boldsymbol{v}\rho) = -\delta_{\rm D}(r-R)(\rho v_{\rm r})_{\rm e} \equiv -\delta_{\rm D}(r-R)\varpi_\rho, \tag{8}$$

where the source appears as an external flux density of matter $(\rho\overline{v_{\rm r}})_{\rm e}$ or ϖ_ρ. Taking the next moment of equation (7) leads us to the Euler–Jeans equation

$$\partial_t\rho\boldsymbol{v} + \nabla\cdot(\rho\boldsymbol{v}\boldsymbol{v}) + \rho\nabla\Psi = -\delta_{\rm D}(r-R)(\rho v_{\rm r}\boldsymbol{v})_{\rm e}, \tag{9}$$

where the source adds a flux density of momentum, $\varpi_{\rho\boldsymbol{v}}$, to the conventional Jeans equation. Taking the successive moments of equation (7) will generically include a new term in the resulting equations.

2.2 Propagating the dynamics

Following Tremaine & Weinberg (1984), equation (7) can be solved along with Poisson's equation in the regime of small perturbations. In the spirit of Paper I, let us define the system's environment by the external perturbative potential $\psi^{\rm e}(\boldsymbol{r}, t)$ and the source $s^{\rm e}(\boldsymbol{r}, \boldsymbol{v}, t)$. Given this environment, the system's linear potential response $\psi(\boldsymbol{r}, t)$ can be computed. Writing the following expansions:

$$\psi(\boldsymbol{r}, t) = \sum_{\boldsymbol{n}} a_{\boldsymbol{n}}(t)\psi^{[\boldsymbol{n}]}(\boldsymbol{r}), \tag{10}$$

$$\psi^{\rm e}(\boldsymbol{r}, t) = \sum_{\boldsymbol{n}} b_{\boldsymbol{n}}(t)\psi^{[\boldsymbol{n}]}(\boldsymbol{r}), \tag{11}$$

$$s^{\rm e}(\boldsymbol{r}, \boldsymbol{v}, t) = \sum_{\boldsymbol{n}} c_{\boldsymbol{n}}(t)\phi^{[\boldsymbol{n}]}(\boldsymbol{r}, \boldsymbol{v}), \tag{12}$$

where $\phi^{[\boldsymbol{n}]}(\boldsymbol{r}, \boldsymbol{v})$ and $\psi^{[\boldsymbol{n}]}(\boldsymbol{r})$ are suitable basis functions, and solving the Boltzmann and Poisson's equations for $a_{\boldsymbol{n}}$, one finds (Aubert et al. 2004)

$$\boldsymbol{a}(t) = \int_{-\infty}^{\infty}\mathrm{d}\tau\boldsymbol{K}(\tau-t)\cdot[\boldsymbol{a}(\tau)+\boldsymbol{b}(\tau)] + \boldsymbol{H}(\tau-t)\cdot\boldsymbol{c}(\tau). \tag{13}$$

Table 1. Description of the various flux densities. The first 10, together with the external potential, are sufficient to characterize fully the environment as shown in Section 3.3.

	Flux density, ϖ	Flux, Φ	Motivation
Mass	$\rho v_{\rm r}$	$\mathrm{d}m/\mathrm{d}t$	Heating and cooling
Angular momentum	$\rho v_{\rm r} \boldsymbol{r} \times \boldsymbol{v}$	$\mathrm{d}L/\mathrm{d}t$	Warp, shape of haloes
Kinetic energy	$\rho v_{\rm r} \sigma_i \sigma_j$	$\mathrm{d}E/\mathrm{d}t$	Virialized objects
Shear	$\rho v_{\rm r}(\partial v_j/\partial x_l + \partial v_i/\partial x_j)$	$\mathrm{d}c/\mathrm{d}t$	Tidal field
Vorticity	$\rho v_{\rm r} \nabla \times \boldsymbol{v}$	$\mathrm{d}\omega/\mathrm{d}t$	Anisotropic accretion

The kernels $\boldsymbol{K}$ and $\boldsymbol{H}$ are functions of the equilibrium state DF, F_0, and of the two bases, $\phi^{[\boldsymbol{n}]}(\boldsymbol{r}, \boldsymbol{v})$ and $\psi^{[\boldsymbol{n}]}(\boldsymbol{r})$ only (see Paper I). As a consequence, they may be computed once and for all for a given equilibrium model. Since the basis function, $\psi^{[\boldsymbol{n}]}$, can be customized to the NFW-like profile of dark matter haloes, it solves consistently and efficiently the coupled dynamical and field equations so long as the entering fluxes of dark matter amount to a small perturbation in mass compared to the underlying equilibrium.

Assuming the linearity and knowledge of $\boldsymbol{K}$ and $\boldsymbol{H}$, one can see that the properties of the environments (through $\boldsymbol{b}$ and $\boldsymbol{c}$) are *propagated* exactly to the inner dynamical properties of collisionless systems. Note in particular that the whole phase-space response of the halo follows from the knowledge of $\boldsymbol{a}$. For example, taking the temporal Fourier transform of equation (13), the cross-correlation matrix is easily deduced:

$$\langle \hat{\boldsymbol{a}} \cdot \hat{\boldsymbol{a}}^{*^\top} \rangle = \langle (\boldsymbol{I} - \hat{\boldsymbol{K}})^{-1} \cdot [\hat{\boldsymbol{K}} \cdot \hat{\boldsymbol{b}} + \hat{\boldsymbol{H}} \cdot \hat{\boldsymbol{c}}] \cdot [\hat{\boldsymbol{K}} \cdot \hat{\boldsymbol{b}} + \hat{\boldsymbol{H}} \cdot \hat{\boldsymbol{c}}]^{\top *} \cdot (\boldsymbol{I} - \hat{\boldsymbol{K}})^{-1 *^\top} \rangle, \tag{14}$$

where $\hat{\boldsymbol{x}} = \hat{\boldsymbol{x}}(\omega)$ is the Fourier transform of $\boldsymbol{x}(t)$. The environment's two-points statistic, via $\langle \hat{\boldsymbol{b}} \cdot \hat{\boldsymbol{b}}^{*^\top} \rangle$, $\langle \hat{\boldsymbol{c}} \cdot \hat{\boldsymbol{c}}^{*^\top} \rangle$ and $\langle \hat{\boldsymbol{b}} \cdot \hat{\boldsymbol{c}}^{*^\top} \rangle$, modifies the correlation of the response of the inner halo.

Linear dynamics do not take into account the effects on the perturbation induced by dynamical friction. More generally the damping of incoming fluxes will ultimately require non-linear dynamics (since the relative temporal phases of the infall do matter in that context). It is also assumed in equation (13) that the incoming material does not modify the equilibrium state of the system. The secular evolution of the system should also be ultimately taken into account, through a quasi-linear theory for example (see e.g. Paper I).

Let us emphasize that, since the addressed problem is linear, the response, equation (13), can be recast into a formulation which only involve an 'external potential', namely the sum of $\psi^{\rm e}$ and the potential created by the entering particles described by $s^{\rm e}$. While formally simpler at the linear deterministic level, this alternative formulation does not translate well non-linearly or statistically (since it would require the full knowledge of the perturbation everywhere in space in a manner which is dependent upon the inner structure of the halo).

In the following sections, our aim is to describe how the two fields $\psi^{\rm e}(\boldsymbol{r}, t)$ and $s^{\rm e}(\boldsymbol{r}, \boldsymbol{v}, t)$ can be extracted from haloes in cosmological simulations. Then it will be shown how to characterize their statistical properties as a function of time via their expansion coefficients, $b_{\boldsymbol{n}}(t)$ and $c_{\boldsymbol{n}}(t)$.

2.3 Convention and notations

In what follows, let us characterize the properties of two fields, either angularly, kinematically, statistically or temporally, or any combination (for various classes of masses). For a given field, X, let us introduce the following notations for clarity:

$$\overline{X} \equiv \frac{1}{4\pi} \int X(\theta, \phi)\, \mathrm{d}\sin(\theta)\, \mathrm{d}\phi, \tag{15}$$

which represents the angular average of X over the sphere. Alternatively, let us define the temporal average over ΔT as

$$\underline{X} \equiv \frac{1}{\Delta T} \int_T^{T+\Delta T} X(t)\, \mathrm{d}t. \tag{16}$$

Finally, let us define the ensemble average as

$$\langle X \rangle \equiv \int X\, \mathcal{F}(X)\, \mathrm{d}X = E\{X\}, \tag{17}$$

where $\mathcal{F}$ is the density probability distribution of X. Here $E\{X\}$ stands for the expectation of X. In practice, in Section 5, an estimator for ensemble average of X measured for N haloes is given:[2]

$$\langle X \rangle_{_N} = \frac{1}{N} \sum_i^N X_i. \tag{18}$$

The underlying probability distributions are sometimes very skewed (when e.g. corresponding to a strong or weak accretion event around massive or smaller haloes), which requires special care when attempting to define statistical trends. Hence, let us also define $\langle\langle X \rangle\rangle$ as the *mode* (or most probable value) of the fitting distribution of $\mathcal{F}$.

All external quantities (flux densities, potential, etc.) will generally be labelled as $X^{\rm e}$. Let us introduce moments of the source over velocities, which correspond to flux densities, noted ϖ_X, and their corresponding fluxes, noted Φ_X. Table 1 gives a list of such flux densities and flux pairs. Finally, the harmonic transform of the field, X, will be written as $a^X_{\ell m}$ and its corresponding power spectrum C^X_ℓ, while the parameters relative to fitting the statistics of the field will be written as q_X. Note that the contrast of the field, X, was also introduced as

$$\delta_X \equiv \frac{X - \overline{X}}{\langle \overline{X} \rangle}, \tag{19}$$

and its corresponding harmonic transform, $\tilde{a}^X_{\ell m}$. A summary of all the notations can be found in Appendix H.

3 THE SOURCE OF INFALL

Let us first describe our strategy to fully characterize the source of cosmic infall at the virial radius via collisionless dark matter simulations, and enumerate the corresponding biases. In particular, let us illustrate our procedure on a template halo.

[2] An alternative would be to weight the sum by the relative number of objects in each halo, hereby down-weighting light haloes. It is found that this alternative estimator did not significantly affect our measurements.

3.1 Describing the source

As argued in Section 2, computing the response of an open system to infalling material requires the knowledge of the source function, $s^{\rm e}(\boldsymbol{r}, \boldsymbol{v}, t)$. Given the particles accreted by a halo, one possibility involves storing those phase-space properties for all particles. While feasible for a limited number of haloes, this task would become rapidly intractable for our large number of simulations. In order to compress the information, the accreted DF is projected here on a basis of function, following equation (12).

Since the measurement is carried at a fixed radius, the phase space is reduced from six to five degrees of freedom: two for the angular position on the sphere, described by two angles $(\theta, \phi) \equiv \boldsymbol{\Omega}$, and three for the velocity space described in spherical coordinates by $(v, \Gamma_1, \Gamma_2) = (v, \boldsymbol{\Gamma})$, where v is the velocity modulus and $\boldsymbol{\Gamma}$ are the two angles describing its orientation (see Fig. 1). The angle, Γ_1, indicates how radial is the velocity, with $\Gamma_1 > \pi/2$ for infalling dark matter and $\Gamma_1 < \pi/2$ for outflows. Γ_2 indicates the orientation of the tangential motion of the infall.

Recall that the two fields, $c_{\boldsymbol{n}}$ (hence $s^{\rm e}(\boldsymbol{\Omega}, \boldsymbol{\Gamma}, v, t)$) and $b_{\boldsymbol{n}}$ (hence $\psi^{\rm e}(\boldsymbol{\Omega}, t)$) are, respectively, five and two dimensional (as a function of mass and time). Note also that both $s^{\rm e}$ and $\psi^{\rm e}$ are statistically stationary with respect to $\boldsymbol{\Omega}$, while $s^{\rm e}$ is partially isotropic and not stationary with respect to $\boldsymbol{\Gamma}$; neither $\psi^{\rm e}$ and $s^{\rm e}$ is stationary with respect to the cosmic time.

3.1.1 *Harmonic expansion of the incoming fluxes*

The $\boldsymbol{\Omega}$ and $\boldsymbol{\Gamma}$ dependences are naturally projected on a basis of spherical harmonics, $Y_{\ell m}(\boldsymbol{\Omega})$ and $Y_{\ell' m'}(\boldsymbol{\Gamma})$. The velocity amplitude dependence is projected on a basis of Gaussian functions, $g_\alpha(v)$, with mean μ_α and a given rms σ. One can write

$$\phi^{[\boldsymbol{n}]}(\boldsymbol{r}, \boldsymbol{v}) = Y_{\boldsymbol{m}}(\boldsymbol{\Omega}) Y_{\boldsymbol{m}'}(\boldsymbol{\Gamma}) g_\alpha(v), \tag{20}$$

where $\boldsymbol{n} \equiv (\ell, m, \alpha, \ell', m') = (\boldsymbol{m}, \alpha, \boldsymbol{m}')$. The expansion coefficients, $c^{\boldsymbol{m}\alpha}_{\boldsymbol{m}'}(t)$, are given by

$$c^{\boldsymbol{m}}_{\boldsymbol{m}'\alpha}(t) = \left(\boldsymbol{G}^{-1} \cdot \boldsymbol{s}^{\boldsymbol{m}}_{\boldsymbol{m}'}\right)_\alpha, \tag{21}$$

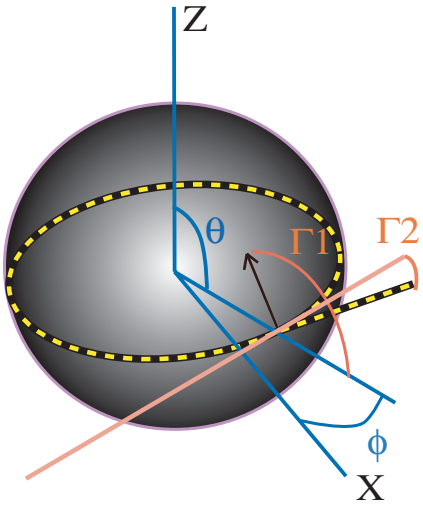

Figure 1. The angles $\boldsymbol{\Omega}$ and $\boldsymbol{\Gamma}$. The dot indicates the position of the particle on the sphere. The dashed ellipse represents the plane which contains both the particle and the sphere centre. X and Z are arbitrary directions defined by the simulation box. $(\theta, \phi) = \boldsymbol{\Omega}$ are the particle's angular coordinates on the sphere. $\boldsymbol{\Gamma} = (\Gamma_1, \Gamma_2)$ define the orientation of the particle's velocity vector (shown as an arrow).

where

$$\left(\boldsymbol{s}^{\boldsymbol{m}}_{\boldsymbol{m}'}\right)_\beta = \int {\rm d}\boldsymbol{\Omega}{\rm d}\boldsymbol{\Gamma}{\rm d}v v^2 g_\beta(v) Y^*_{\boldsymbol{m}}(\boldsymbol{\Omega}) Y_{\boldsymbol{m}'}(\boldsymbol{\Omega}) s^{\rm e}(v, \boldsymbol{\Omega}, \boldsymbol{\Gamma}, t), \tag{22}$$

given

$$\boldsymbol{G}_{\alpha,\beta} = \int {\rm d}v v^2 g_\alpha(v) g_\beta(v). \tag{23}$$

Note that the expansion defined in equation (12), where the coefficients are given by equation (21), involves five subscripts spanning the five-dimensional phase space, while the expansion in equation (10) only involves three subscripts. This description of the source term is reduced to a set of coefficients which depends on time only. Furthermore, this procedure requires parsing the particles only once, and all the momenta (e.g. mass flux density, probability distribution function, hereafter PDF, of impact parameter, etc.) of the source terms can be computed directly from these coefficients. As a consequence, the statistics of momenta follow linearly from the *statistics* of coefficients only, as shown in Section 4.2.

3.1.2 *Harmonic expansion of the external potential*

Let us call $b'_{\ell m}(t)$ the harmonic coefficients of the expansion of the external potential on the virial sphere. Following Murali (1999), let us expand the potential over the biorthogonal basis $(u^{\ell m}_n, d^{\ell, m}_n)$, so that

$$\begin{aligned}\psi^{\rm e}(r, \boldsymbol{\Omega}, t) &= \sum_{n,\ell,m} b'_{\ell m}(t)\, Y^m_\ell(\boldsymbol{\Omega}) \left(\frac{r}{R_{200}}\right)^\ell, \\ &= \sum_{\boldsymbol{n}} b_{\boldsymbol{n}}(t) \psi^{[\boldsymbol{n}]}(\boldsymbol{r}),\end{aligned} \tag{24}$$

where $\psi^{[\boldsymbol{n}]}(\boldsymbol{r}) \equiv Y^m_\ell(\boldsymbol{\Omega}) u^{\ell m}_j(r)$. The first equality in equation (24) corresponds to the inner solution of the three-dimensional potential whose boundary condition is given by $Y^\ell_m(\boldsymbol{\Omega}) b'_{\ell m}$ on the sphere of radius R_{200} (defined below). Since the basis is biorthogonal, it follows that

$$b_{\boldsymbol{n}}(t) = \left[\int d^{\ell m}_n(r) \left(\frac{r}{R_{200}}\right)^\ell {\rm d}r\right] b'_{\ell m}(t). \tag{25}$$

It is therefore straightforward to recover the coefficient of the 3D external potential from that of the potential on the sphere.

3.2 From simulations to expansion coefficients

Once a halo is detected, its outer 'boundary' is defined as a sphere centred on its centre of mass with a radius, R_{200} (or virial radius), defined implicitly by $3M/(4\pi R^3_{200}) = 200\rho_0$. This choice of radius is the result of a compromise between being a large distance to the halo centre, to limit the contribution of halo's inner material to fluxes, and being still close enough to the halo's border, to limit the simulation's fraction to be processed and avoid contributions of fly by objects. Let us emphasize that several definition of the virial radius can be found in the literature, involving e.g. the critical density, or a different contrast factor, where the latter may or may not depend on the cosmology. Hence, one should keep in mind that all the quantitative results presented in this article depend on our specific choice of a definition.

The time evolution of accretion is measured backwards in time by following the biggest progenitor of each halo detected at redshift $z = 0$. The positions and velocities of particles passing through the virial sphere between snapshots are then stored. All positions are measured

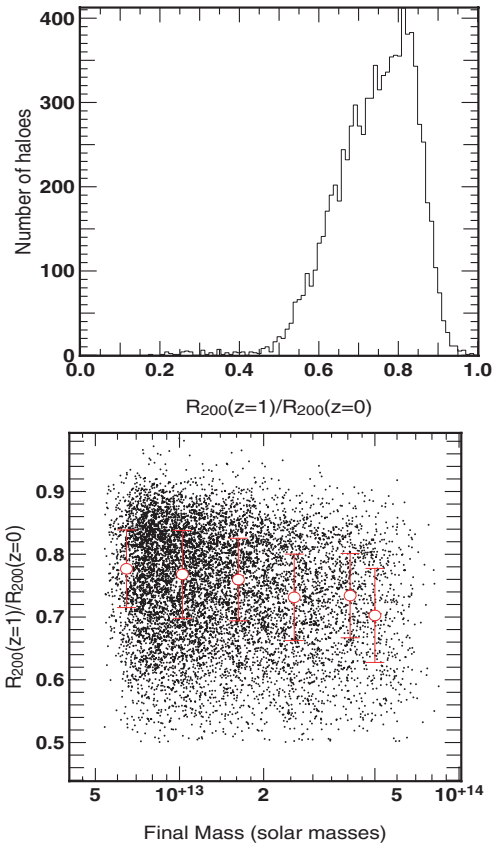

Figure 2. Top: the distribution of the ratio between the virial radii measured at $z = 1$ and 0. Bottom: the distribution of $R_{200}(z = 1)/R_{200}(z = 0)$ as a function of the halo's final mass. Each point represents one halo. Symbols stand for the median value of $R_{200}(z = 1)/R_{200}(z = 0)$ in six different classes of masses. Bars stand for the interquartile. The two measurements were performed on 9023 haloes which satisfy the selection criteria defined in Section 4.2.

relative to the biggest progenitor centre of mass, while velocities are measured relative to its average velocity, for each redshift z. In one of the simulation described below, the total comoving drift distance of the centre of mass was compared to the distance between the halo's positions measured at $z = 1$ and 0. The haloes were chosen to satisfy the criteria described in Section 4.2. It is found that the scattering of the motion of the centre of mass represents less than 10 per cent of the distance covered in 8 Gyr. The centre of mass of the biggest progenitor seems stable enough to be a reference.

Sticking to the previous definition of R_{200} would imply a changing outer boundary, and an 'inertial' flux through a moving surface would have to be taken into account. To overcome this effect, the sphere was kept constant in time at a radius equals to $R_{200}(z = 0)$. This choice corresponds to a reasonable approximation since the actual virial radius does not change significantly with time between $z < 2$ for a reasonably smooth accretion history. As shown in Fig. 2, the virial radius at $z = 1$ is only 20 per cent smaller than R_{200} measured at $z = 0$. Larger haloes have larger variations, but the median value of the difference between the two radii remains smaller than 30 per cent for final masses smaller than $10^{14}\,\mathrm{M}_{\odot}$. Finally, measurements were done using physical coordinates (and not comoving coordinates). These choices were partly guided by the fact that they simplify future applications of these results to the inner dynamic of the haloes (see Paper I).

3.2.1 *Sampling on the sphere*

As shown in Section 2, the source function s^{e} reads

$$s^{\mathrm{e}} \equiv f(\boldsymbol{r}, \boldsymbol{v}, t)v_{\mathrm{r}} = \sum_i \delta_{\mathrm{D}}^3[\boldsymbol{r} - \boldsymbol{r}_i(t)]\delta_{\mathrm{D}}^3[\boldsymbol{v} - \boldsymbol{v}_i(t)]v_{\mathrm{r},i}. \tag{26}$$

Switching to spherical coordinates leads us to

$$s^{\mathrm{e}} = \sum_i^N \frac{\delta_{\mathrm{D}}[R_{200} - r_i(t)]}{R_{200}^2}\frac{\delta_{\mathrm{D}}[v - v_i(t)]}{v^2} \times \frac{\delta_{\mathrm{D}}[\boldsymbol{\Omega} - \boldsymbol{\Omega}_i(t)]}{\sin\Omega_1}\frac{\delta_{\mathrm{D}}[\boldsymbol{\Gamma} - \boldsymbol{\Gamma}_i(t)]}{\sin(\Gamma_1)}v_{\mathrm{r},i}(t), \tag{27}$$

where i is the particle index. Now,

$$v_{\mathrm{r},i}\delta_{\mathrm{D}}[R_{200} - r_i(t)] = \sum_k v_{\mathrm{r},k,i}\left|\frac{\mathrm{d}t}{\mathrm{d}r}\right|\delta_{\mathrm{D}}(t - t_{200,k,i}), = \sum_k w_{k,i}\delta_{\mathrm{D}}(t - t_{200,k,i}), \tag{28}$$

where $t_{200,k,i}$ corresponds to the kth passage of the ith particle through the virtual boundary R_{200} (and $v_{\mathrm{r},k,i}$ is the corresponding radial velocity). In our conventions, the weight function $w_{k,i}$ takes the value 1 if the particle is entering and -1 if it is exiting the virial sphere. Given that our time resolution is finite, let us consider a time interval ΔT around t and define the (temporal) average phase-space flux density over ΔT:

$$\underline{s}^{\mathrm{e}}(t) \equiv \frac{1}{\Delta T}\int_t^{t+\Delta T}\mathrm{d}\tau s^{\mathrm{e}}(\tau). \tag{29}$$

Equation (28) becomes

$$\underline{s}^{\mathrm{e}}(t) = \sum_{i,k}^N \frac{\delta(v - v_{i,k})}{v^2\Delta T R_{200}^2}\frac{\delta(\boldsymbol{\Omega} - \boldsymbol{\Omega}_{i,k})}{\sin\Omega_1}\frac{\delta(\boldsymbol{\Gamma} - \boldsymbol{\Gamma}_{i,k})}{\sin(\Gamma_1)}w_{i,k}. \tag{30}$$

The simulations were sampled in time regularly in $\ln(z)$ [i.e. $\Delta\ln(z) = \text{constant}$]. From $z = 2$ to 0.1, 23 snapshots were taken (and a $z = 0$ snapshot was added to the sample). If Δt is small, the sum over k should mostly involve one passage, i.e.

$$\underline{s}^{\mathrm{e}}(t) \sim \frac{1}{\Delta T R_{200}^2}\sum_i^N \frac{\delta(v - v_i)}{v^2}\frac{\delta(\boldsymbol{\Omega} - \boldsymbol{\Omega}_i)}{\sin\Omega_1}\frac{\delta(\boldsymbol{\Gamma} - \boldsymbol{\Gamma}_i)}{\sin(\Gamma_1)}w_i. \tag{31}$$

Now, these measurements only give access to $(v, \boldsymbol{\Omega}, \boldsymbol{\Gamma})$ at fixed redshift, z, and at every varying redshift Δz. Consequently, these values need to be interpolated at the sought $t_{200,i}$ approximated by

$$t_{200,i} = t_i(z_n) + \frac{t(z_{n+1}) - t(z_n)}{r_i(z_{n+1}) - r_i(z_n)}[R_{200} - r_i(z_n)]. \tag{32}$$

Given these 'crossing' instant, the positions, $\boldsymbol{r}$, and velocities, $\boldsymbol{v}$, are also linearly interpolated. For instance, one gets for the x component of the velocity

$$v_{x,i}(t_{200}) = v_{x,i}(z_n) + \frac{v_{x,i}(z_n + 1) - v_{x,i}(z_n)}{t(z_{n+1}) - t(z_n)}[t_{200} - t(z_n)]. \tag{33}$$

Such an interpolation is not strictly self-consistent since a ballistic motion requires a constant velocity along the trajectory. The worst-case scenario would correspond to particles which have entered the virial sphere with an outflowing velocity vector and vice versa. As a simple but important check, the distribution of interpolated radial velocities was plotted (see Fig. 3). Those were computed from the whole history of accretion of a typical halo ($R_{200} = 860$ kpc,

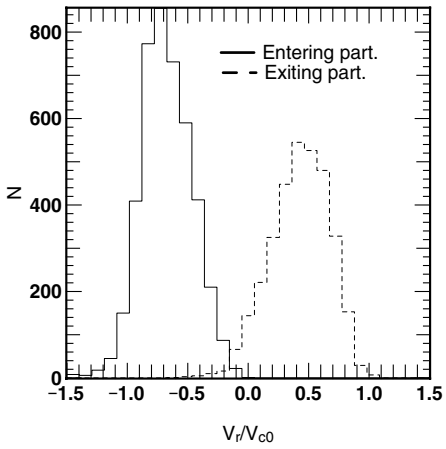

Figure 3. The distribution of interpolated radial velocities v_r of particles passing through the virial radius. Those particles were taken from the whole history of accretion of a typical halo [$R_{200} = 860$ kpc, $M(z = 0) = 3 \times 10^{13}\,\mathrm{M}_\odot$]. Entering particles (solid line) have $v_r < 0$, while exiting particles (dashed line) have $v_r > 0$, as it should be.

$M_{z=0} = 3 \times 10^{13}\,\mathrm{M}_\odot$). The two types of particles (entering/exiting) are confined in their radial velocity plane: entering (respectively exiting) particles have negative (respectively positive) radial velocities. Velocities are correctly interpolated. It also means that our time-steps are small enough to ensure a small variation of positions/velocities of particles, validating a posteriori our assumptions. A fraction of exiting particles do have a negative radial velocity but represent less than a few per cent of the total population. For safety, those particles are rejected from the following analysis.

One should note that the measured angular scales are sensitive to the time sampling (see Fig. 4). Increasing the sampling time tends to increase the apparent size of objects as measured in the sphere. Since this increase depends on the shape or the orientation of the objects, this effect *cannot* be simply time averaged. As a consequence, a varying time-step would induce a variation of typical spatial scale. The interpolation given by equation (32) allows also for a constant time-step resampling of the source term $\underline{s}^{\mathrm{e}}$. All reference to the time average will be dropped from now on.

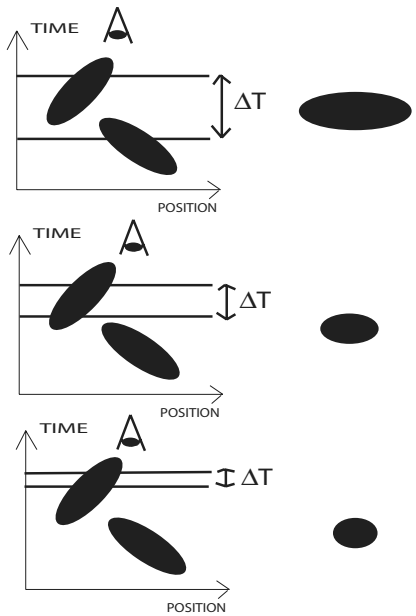

Figure 4. The impact of time averaging on the measured scales of dark matter passing through the sphere. On the left-hand side, time–position diagram of dark matter (black ellipses) as they pass through the sphere. Time integration is performed during ΔT (the two horizontal lines). On the right-hand side, the accreted dark matter as seen on the sphere. A longer integration time increases the length-scale of the incoming blob. If ΔT gets very large, different blobs may be seen as one (upper diagram).

Given equation (30), computing the expansions coefficients of s_{e} is straightforward:

$$c^{\boldsymbol{m}}_{\alpha,\boldsymbol{m}'} = \left[\boldsymbol{G}^{-1} \sum_i^N w_i \frac{\boldsymbol{g}(v_i) Y^*_{\boldsymbol{m}}(\boldsymbol{\Omega}_i) Y^*_{\boldsymbol{m}'}(\boldsymbol{\Gamma}_i)}{\Delta T R^2_{200}} \right]_\alpha . \tag{34}$$

It is expected that the above procedure is more accurate than the strategy presented in Aubert et al. (2004), where the flux densities were smoothed over a shell of finite thickness ($R_{200}/10$).

The harmonic expansion $b'_{\boldsymbol{m}}$ of the external potential $\psi^{\mathrm{e}}(R_{200}, \boldsymbol{\Omega})$ is computed directly from the positions of external particles (e.g. Murali & Tremaine 1998):

$$b'_{\ell,m}(t) = -\frac{4\pi G}{2\ell+1} \sum_j^N Y^*_{\ell m}[\boldsymbol{\Omega}_j(t)] \frac{R^\ell_{200}}{r_j^{\ell+1(t)}}, \tag{35}$$

where r_j and $\boldsymbol{\Omega}_j$ are the distance and the two angles defining the position of the jth external particles, respectively. The quantities $r_j(t)$ and $\boldsymbol{\Omega}_j(t)$ at time t are obtained by linear interpolation between two snapshots. Using equation (24), $\psi^{\mathrm{e}}(r < R_{200}, \boldsymbol{\Omega})$ can be reconstructed from the coefficients $b'_{\boldsymbol{m}}$.

Section 4.2 makes extensive use of equations (34) and (35) for *each* halo in our simulations to statistically characterize these two fields.

3.3 From flux densities to the 5D source

The description of the source term s^{e} involves time-dependent coefficients $c^{\ell m}_{\alpha \ell' m'}(t)$. Their computation from the particle coordinates is quite straightforward and as shown in the previous sections, the different margins can be recovered through the manipulation of these coefficients. Yet a projection of the source on an a priori basis is a complex operation. Here this projection aims at describing a 5D space for which little is known. As shown in the following sections, the distribution of incidence angles is quite smooth, while the distribution of velocities appears to be easily parametrized by Gaussians. The 5D basis presented in the current paper induces little bias, but it is very likely that a more compact basis exists and that the size of the expansions chosen can be reduced in the future.

Because of this large amount of information contained in the source, it is not always convenient to relate coefficients or their correlations to physical quantities, like the mass flux or the flux density of energy. An alternate description of the source term was presented in Aubert et al. (2004) with the following ansatz:

$$s^{\mathrm{e}}(\boldsymbol{r}, \boldsymbol{v}, t) = \sum_{\boldsymbol{m}} Y_{\boldsymbol{m}}(\boldsymbol{\Omega}) \frac{\hat{\varpi}_{\rho,\boldsymbol{m}} (2\pi)^{-3/2}}{\det(\hat{\varpi}_{\rho\sigma\sigma,\boldsymbol{m}}/\hat{\varpi}_{\rho,\boldsymbol{m}})} \times \exp\left[-\frac{1}{2} \left(\boldsymbol{v} - \frac{\hat{\varpi}_{\rho v,\boldsymbol{m}}}{\hat{\varpi}_{\rho,\boldsymbol{m}}} \right)^\top \left(\frac{\hat{\varpi}_{\rho\sigma\sigma,\boldsymbol{m}}}{\hat{\varpi}_{\rho,\boldsymbol{m}}} \right)^{-1} \left(\boldsymbol{v} - \frac{\hat{\varpi}_{\rho v,\boldsymbol{m}}}{\hat{\varpi}_{\rho,\boldsymbol{m}}} \right) \right]. \tag{36}$$

This representation of the source is by construction consistent with the first two velocity moments

$$\int \mathrm{d}^3\boldsymbol{v} s^{\mathrm{e}}(\boldsymbol{r}, \boldsymbol{v}) = \varpi_\rho(\boldsymbol{r}), \quad \int \mathrm{d}^3\boldsymbol{v}\boldsymbol{v} s^{\mathrm{e}}(\boldsymbol{r}, \boldsymbol{v}) = \varpi_{\rho v}(\boldsymbol{r}), \tag{37}$$

while

$$\int \mathrm{d}^3\boldsymbol{v}\left(v_i - \frac{\varpi_{\rho v,i}}{\varpi_\rho}\right)\left(v_j - \frac{\varpi_{\rho v,j}}{\varpi_\rho}\right)s^{\mathrm{e}}(\boldsymbol{r},\boldsymbol{v}) = \varpi_{\rho\sigma_i\sigma_j}(\boldsymbol{r}) - \frac{\varpi_{\rho v}(\boldsymbol{r})^2}{\varpi_\rho(\boldsymbol{r})} + \sum_{\boldsymbol{m}} Y_{\boldsymbol{m}}(\boldsymbol{\Omega})\delta(r - R_{200})\frac{\hat{\varpi}_{\rho v,\boldsymbol{m}}(t)^2}{\hat{\varpi}_{\rho,\boldsymbol{m}}(t)},$$

$$\approx \varpi_{\rho\sigma_i\sigma_j}(\boldsymbol{r}). \quad (38)$$

Obviously, the third moment is not fully recovered from the ansatz given by equation (36). This example should be taken as an illustration and highlights the possibility of building a source term from its moments. It is not unique and more realistic expressions could be found, which satisfies higher moments of the source. Still, the successive measurements on the sphere of the flux density of mass ϖ_ρ, momentum $\varpi_{\rho v}$ and velocity dispersion $\varpi_{\rho\sigma\sigma}$ allow a coherent description of the infall of matter. Unlike the coefficients, these flux densities are easier to interpret since they describe physical quantities and are directly involved in specific dynamical processes (see Table 3.3). Furthermore, these three flux densities are easily expressed in terms of coefficients, $c^{\ell m}_{\alpha\ell' m'}(t)$, or more precisely in terms of *a subset* of the source's coefficients, implying a smaller number of computations relative to a complete calculation of $c^{\ell m}_{\alpha\ell' m'}(t)$. Finally, these flux densities are particularly suited to the regeneration of synthetic environments. As shown in Appendix F, synthetic spherical maps can be generated from the two-point correlations and cross-correlations of these fields. Such environments would be consistent with the measurements in simulations and will allow us to easily embed simulated galaxies or haloes in realistic environments as a function of time.

The expression given in equation (36) has one important drawback: it is not of the form of equation (12), i.e. it would require a reprojection over a linear expansion for a dynamical propagation. Nevertheless, its capacity makes it easier to compute than the full set of coefficients and the associated strategy would be (i) to measure the flux densities from the simulation, (ii) to build a source term from e.g. equation (36) and (iii) to project over an appropriate 5D basis when needed, i.e. when the source is used as an input to the analytic description of the haloes' dynamics.

The following sections will make intensive use of the coefficients described by equations (34) and (35). In particular, it will show how the manipulation of these coefficients allows us to recover relevant physical quantities. In the current paper, only the first moment of the source, the flux density of mass ϖ_ρ, together with the external potential, will be fully assessed. The kinematical properties of the accreted material will in particular be investigated. The complete characterization of the $\boldsymbol{c}(t)$ coefficients is beyond the scope of the current paper and will be completed in Paper III. The full measurements of these 11 fields required by equation (36) and the comparisons between the two expressions of the source will also be assessed in the future paper as well. Appendices G1 and G2 describe how the other moments, the flux density of momentum $\varpi_{\rho v}$ or the flux density of energy $\varpi_{\rho\sigma^2}$ may be recovered from the source expansion.

3.4 A template halo

As an illustration, let us first apply the whole machinery to one typical halo. At $z = 0$, this 'template' halo has a mass M of $3.4 \times 10^{13}\,\mathrm{M}_\odot$, with a virial radius R_{200} of $800\,h^{-1}$ kpc. The corresponding circular velocity is $V_{\mathrm{c}0} = 600$ km s^{-1}. Its accretion history is shown in Fig. 5 for $z < 1$. Each point on the azimuth–time diagram represents one particle of the simulation passing through the virial sphere at a given azimuth and at a given time. Temporal space has been sampled using 15 equally spaced bins between $z = 1$ and 0 (see bottom panel in Fig. 5). For each time-step, the expansion coefficients $c^{\boldsymbol{m}'}_{\alpha,\boldsymbol{m}}(t)$ are computed from equation (34). The Gaussian basis $g_\alpha(v)$ involved 25 functions with mean μ_α equally distributed from $v = 0$ to 1.5 in $V_{\mathrm{c}0}$ units and with a rms $\sigma = 0.03$. The harmonic expansions were carried up to $\ell = 50$ in position space and $\ell' = 25$ in velocity space.

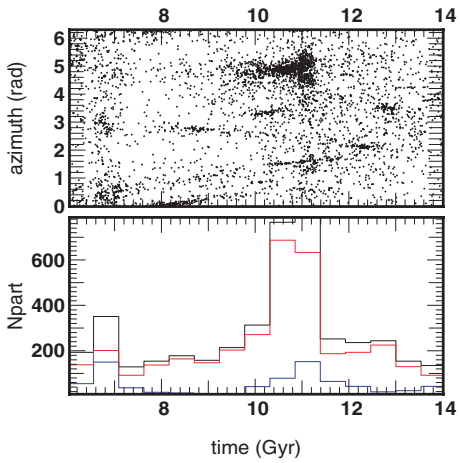

Figure 5. An example of accretion history. Top: azimuth–time diagram. Each point in the diagram represents one particle passing through the virial sphere at a given azimuth (y-axis) at a given time measured from the big bang (x-axis). Bottom: the distribution of crossing instances of particles (in black). Time increases from left to right. The infalling (respectively outflowing) particles distribution is shown in red (respectively blue).

3.4.1 *Advected mass: angular space (ϖ_ρ)*

The template halo accretes an object at $t_{\mathrm{s}} = 11$ Gyr (where $t = 14$ Gyr stands for $z = 0$) adding $7.5 \times 10^{12}\,\mathrm{M}_\odot$ to the system during a ∼1-Gyr interval. The corresponding spherical flux density field, $\varpi_\rho(\boldsymbol{\Omega}, t_{\mathrm{s}})$, is shown in Fig. 6. It represents the distribution of accreted particles as seen from a halocentric point of view. The field $\varpi_\rho(\boldsymbol{\Omega}, t_{\mathrm{s}})$ has been reconstructed from the coefficients (see equation 34). It reads

$$\varpi_\rho(\boldsymbol{\Omega}, t) = \int \mathrm{d}\boldsymbol{\Gamma}\mathrm{d}v v^2 s^{\mathrm{e}}(v, \boldsymbol{\Omega}, \boldsymbol{\Gamma}, t) = \sum_{\boldsymbol{m}} a_{\boldsymbol{m}}(t) Y_{\boldsymbol{m}}(\boldsymbol{\Omega}). \quad (39)$$

Since

$$\int \mathrm{d}\boldsymbol{\Gamma}\, Y_{\ell',m'} = \sqrt{4\pi}\delta_{\ell' 0}\delta_{m' 0}\,, \quad \text{and} \quad \int \mathrm{d}v v^2 g_\alpha(v) = \mu_\alpha^2 + \sigma^2. \quad (40)$$

It follows that

$$a_{\boldsymbol{m}}(t) = \sqrt{4\pi}\sum_\alpha (\mu_\alpha^2 + \sigma^2) c^{\boldsymbol{m}}_{\alpha,\boldsymbol{0}}(t), \quad (41)$$

allowing us to recover $\varpi_\rho(\boldsymbol{\Omega}, t_{\mathrm{s}})$. Also shown is the same field, but computed this time using directly the angular distribution of particles as described in Aubert et al. (2004) (see below). All the major features are well reproduced by the expansion coefficients (equations 34–41). Clearly, an object is 'falling' through the virial sphere. It is straightforward to obtain the angular power spectrum $C_\ell^{\varpi_\rho}$ from the $c^{\boldsymbol{m}}_{\alpha,\boldsymbol{m}'}$ coefficients via the definition of $a_{\ell m}$ in equation (41):

$$C_\ell^{\varpi_\rho} = \frac{1}{4\pi}\frac{1}{2\ell+1}\sum_m |a_{\ell m}|^2. \quad (42)$$

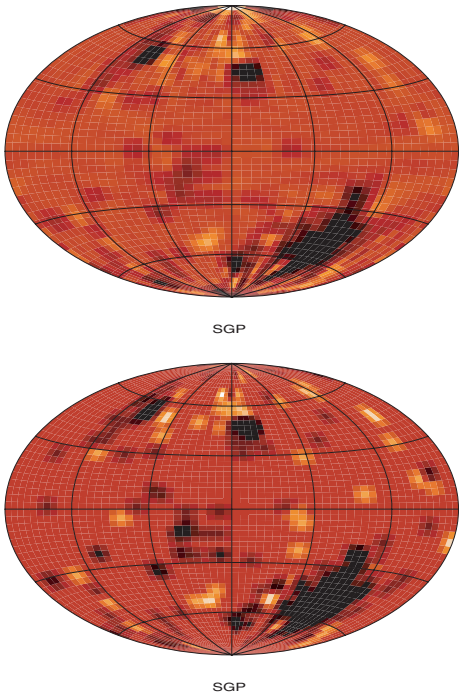

Figure 6. An example of a flux density reconstructed from the coefficients $c^{\boldsymbol{m}}_{\alpha,\boldsymbol{m}}$: the mass flux density, $\rho v_{\rm r}(\boldsymbol{\Omega})$. It represents the angular distribution of incoming mass as seen from a halocentric point of view. Here $t_{\rm s} \sim 11$ Gyr. Light regions correspond to strong infall, while darker regions stand for low accretion and outflows. Top: the spherical field obtained directly from the spatial distribution of particles. Bottom: the reconstructed spherical field from the coefficients (equation 34).

The angular power spectrum of $\varpi_\rho(\boldsymbol{\Omega}, t_{\rm s})$, derived from the expansion (equation 34), is shown in Fig. 7. From the positions and velocities of particles, it is also possible to evaluate $\varpi_\rho(\boldsymbol{\Omega}, t_{\rm s})$ on an angular grid and recover the angular power spectrum 'directly'. The agreement between the two $C_\ell^{\varpi_\rho}$ is good, though for the smallest scales ($\ell \geqslant 30$), the power spectrum computed from the coefficients is slightly larger than the one derived directly from the particles.

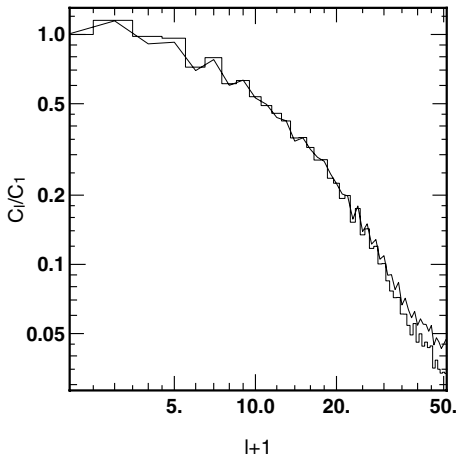

Figure 7. The angular power spectrum, C_ℓ/C_1 (equation 42), of the distribution of incoming matter, $\varpi_\rho(\boldsymbol{\Omega})$ (shown in Fig. 6) at $t\sim$ 11 Gyr, for our template halo. For a given ℓ, the corresponding angular scale is π/ℓ. The histogram corresponds to the power spectrum derived directly from the angular distribution of particles. The solid line is the power spectrum reconstructed from the coefficients.

This may be explained by the fact that a grid sampling tends to smooth the actual ϖ_ρ field. As a consequence, the amplitude of small-scale fluctuations is decreased, leading to a smaller $C_\ell^{\varpi_\rho}$. A more complete discussion on harmonic convergence can be found in Appendix A. For a given ℓ, the corresponding angular scale is π/ℓ in radians.

Note that the coefficients a_{00} are closely related to the accretion field averaged over all directions, $\Phi^{\rm M}(t)$, defined by

$$\Phi^{\rm M}(t) \equiv \overline{\varpi_\rho} = \frac{1}{4\pi}\int {\rm d}\boldsymbol{\Omega}\rho v_{\rm r}(\boldsymbol{\Omega}, t) = \frac{a_{00}}{\sqrt{4\pi}}. \tag{43}$$

Measuring $a_{00}(t)$ amounts to measuring the accretion flux density, i.e. the quantity of dark matter accreted per unit surface and per unit time.

3.4.2 *Advected mass: velocity space*

Integration over the sphere leads us to the distribution of accreted matter in velocity space:

$$\rho v_{\rm r}(\boldsymbol{\Gamma}, v, t) = \int {\rm d}\boldsymbol{\Omega} s^{\rm e}(v, \boldsymbol{\Omega}, \boldsymbol{\Gamma}, t), \tag{44}$$

$$= \sqrt{4\pi}\sum_{\alpha,\boldsymbol{m}'} c^0_{\alpha,\boldsymbol{m}'} g_\alpha(v) Y_{\boldsymbol{m}'}(\boldsymbol{\Gamma}). \tag{45}$$

Projections over Γ_2 and v give the probability distribution of the incidence angle Γ_1, $\vartheta(\Gamma_1, t)$, defined as

$$\begin{aligned}\vartheta(\Gamma_1, t) &= \int {\rm d}\Gamma_2 {\rm d}v v^2 \rho v_{\rm r}(\boldsymbol{\Gamma}, v, t),\\ &= 2\pi\sqrt{4\pi}\sum_{\alpha,\ell'} c^0_{\alpha,\{\ell',0\}}\left(\mu_\alpha^2 + \sigma^2\right) Y_{\ell',0}(\boldsymbol{\Gamma}).\end{aligned} \tag{46}$$

The impact parameter b of an incoming particle (measured in units of the virial radius) is related to Γ_1 by

$$\frac{b}{R_{200}} = \sin(\Gamma_1), \tag{47}$$

therefore the probability distribution of impact parameters, $\vartheta(b)$, is easily deduced from equation (46). At $t\sim 11$ Gyr, the $\vartheta(b)$ computed from the source coefficients is compared to that derived directly from the velocities of particles in Fig. 8. Note that for pure geometrical reasons small impact parameter b is less likely since there is only one trajectory passing through the centre, while there is a whole cone of trajectories with $b \neq 0$. As a consequence, errors are intrinsically larger for small values of b. The reconstruction from the source coefficients is clearly adequate. In this example, the high probability for infalling particles to have a small impact parameter ($b < 0.5$) implies that velocities are strongly radial. The object 'dives' into the halo's potential well.

Projection over Γ_1 leads to the probability distribution of particle velocities, $\varphi(v, t_{\rm s})$, as they pass through the virial sphere. The PDF $\varphi(v, t)$ is defined as

$$\varphi(v, t) \equiv v^2 \int {\rm d}\boldsymbol{\Omega}\, {\rm d}\boldsymbol{\Gamma} s^{\rm e}(v, \Omega, \boldsymbol{\Gamma}, t). \tag{48}$$

Here the v^2 weighting accounts for the fact that the probability distribution of measuring a velocity, v, within dv is of interest here. Using coefficients, it follows that

$$\varphi(v, t) = 4\pi\sum_\alpha v^2 g_\alpha(v) c^0_{\alpha,0}. \tag{49}$$

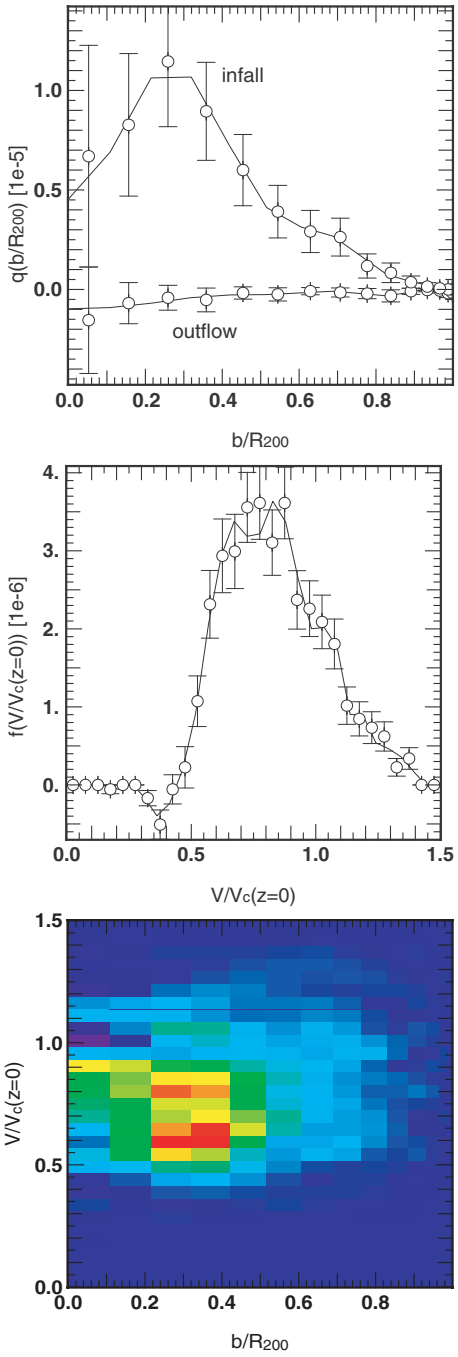

Figure 8. Top: excess probability distribution of impact parameters b and $\vartheta(b)$, derived from the $c^{\boldsymbol{m}}_{\alpha,\boldsymbol{m}'}(t)$ source coefficients (equation 34) of our template halo at $t_s \sim 11$ Gyr (line). The histogram corresponds to the same distribution derived directly from the positions and velocities of particles. Error bars stand for 3σ errors. The impact parameters are given in units of R_{200}. The unit in y-axis is $5 \times 10^9\,\mathrm{M}_\odot\,\mathrm{kpc}^{-2}\,\mathrm{Myr}^{-1}$. Infall is mainly radial. Middle: the velocity distribution of particles, $\varphi(v)$, accreted at $t_s \sim 11$ Gyr, for our template halo. Velocities are expressed in terms of the circular velocity at $z = 0$. The unit in y-axis is $5 \times 10^9\,\mathrm{M}_\odot\,\mathrm{kpc}^{-2}\,\mathrm{Myr}^{-1}$. The histogram corresponds to the velocity distribution obtained directly from the velocities of the particles. The solid line is the reconstructed distribution from the source coefficients. Bottom: the probability distribution, $\wp(b, v)$, of particles in the $b - v$ subspace. Units are the same as above. Red/blue stands for high/low densities. No correlation is found between b and v for this specific example.

The reconstructed velocity distribution is also shown in Fig. 8. It reproduces well the actual velocity distribution. For this specific halo, the satellite is being accreted with a velocity of $0.75\,V_{c0}$.

The correlation between the incidence angle Γ_1 and the velocity's amplitude v may be studied by integrating $\rho v_r(\Gamma, v, t)$ over Γ_2 only. The DF, $\wp(\Gamma_1, v)$, of particles in the (Γ_1, v) subspace is defined by

$$\wp(\Gamma_1, v) \equiv \int \mathrm{d}\Gamma_2 \mathrm{d}v v^2 \rho v_r(\mathbf{\Gamma}, v, t)\,,$$
$$= 2\pi\sqrt{4\pi} \sum_{\alpha,\ell'} c^{\mathbf{0}}_{\alpha,\{\ell',0\}} g_\alpha(v) Y_{\ell',0}(\Gamma_{1,0}). \quad (50)$$

Given the relation (equation 47), the correlation $\wp(b, v)$ between the impact parameter and the velocity's amplitude is easily obtained. The $\wp(b, v)$ distribution is shown in Fig. 8. Again, note that $\wp(b, v)$ represents an excess probability of finding an impact parameter b (with a velocity v) compared to isotropy. In this specific example, no real correlation may be found between the two quantities. Finally, the integration of $\wp(b, v)$, $\varphi(v, t)$ and $\vartheta(\Gamma_1)$ over their respective space leads to the same quantity, namely the integrated flux $\Phi^{\mathrm{M}}(t)$.

3.4.3 External potential

The final field needed on the virial sphere is the external tidal field created by the dark matter distribution around the halo.

Using equation (35), the external potential $\psi^{\mathrm{e}}(\mathbf{\Omega}, t)$ is easily computed from the positions of external particles, having restricted the sampling to particles within a 4 Mpc (physical) sphere centred on the halo. The position of external particles is linearly interpolated at a given measurement of time. The coefficients $b_{\boldsymbol{m}}$ for the template halo are computed at $t_s \sim 7$ Gyr (measured from the big bang). The reconstructed field $\psi^{\mathrm{e}}(\mathbf{\Omega}, t)$ is shown in Fig. 9 along with the modulus of the advected mass $|\rho v_r(\mathbf{\Omega})|$. The two reconstructions were restricted to harmonics $\ell \leqslant 20$.

The two spherical fields show the same main features. However, almost no small-scale feature is seen in the map of the external potential even though they have the same resolution. Since the gravitational potential is known to be smoother than the associated density and is dominated by the global tidal field, it is not surprising that $\psi^{\mathrm{e}}(\mathbf{\Omega}, t)$ appears smoother than the advected mass field $|\varpi_\rho(\mathbf{\Omega})|$.

The potential's angular power spectrum may also be computed by replacing $a_{\ell m}$ by $b_{\ell m}$ in equation (42) (see Fig. 10). The power spectrum of the potential, $C_\ell^{\varpi_\rho}$, sharply decreases with ℓ, while $C_\ell^{\varpi_\rho}$ has a gentler slope. Large scales are clearly more important for the potential than for the advected mass. Furthermore, C_ℓ^{ψ} systematically peaks for even ℓ values, reflecting the 'even' symmetry of the potential measured on the sphere.

4 SIMULATION SAMPLE AND STATISTICAL BIASES

Section 3.4 details the measurement strategy for a given typical halo. It is now possible to reproduce the above measurements for all the haloes of the simulation sample. Let us first describe in turn the construction of our sample, and the corresponding biases, which constrain our ability to convert a large set of simulations into the statistics of the source.

4.1 Simulations

In order to achieve a sufficient sample and ensure a convergence of the measurements, a set of ~500 simulations was produced

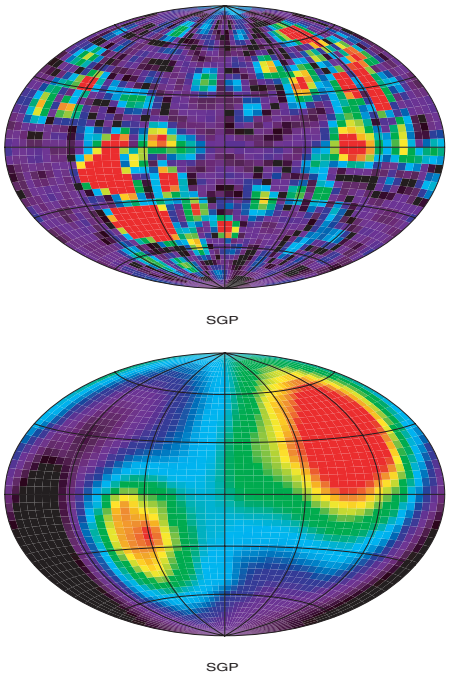

Figure 9. A comparison between the external potential, $\psi^{\rm e}(\mathbf{\Omega})$ and the modulus of the flux density of matter, $|\rho v_{\rm r}(\mathbf{\Omega})|$. The measurement is made at $t \sim 7$ Gyr (measured from the big bang) on our template halo. The two fields were, respectively, reconstructed from $c^{\boldsymbol{m}}_{\alpha,\boldsymbol{m}'}$ and $b_{\boldsymbol{n}}$ coefficients with $\ell_{\rm max} \leqslant 20$. Even though the two fields are similar and exhibit a strong quadrupolar component, $\psi^{\rm e}(\mathbf{\Omega})$ is smoother than $\rho v_{\rm r}(\mathbf{\Omega})$. It is expected that the corresponding expansion coefficients be statistically correlated.

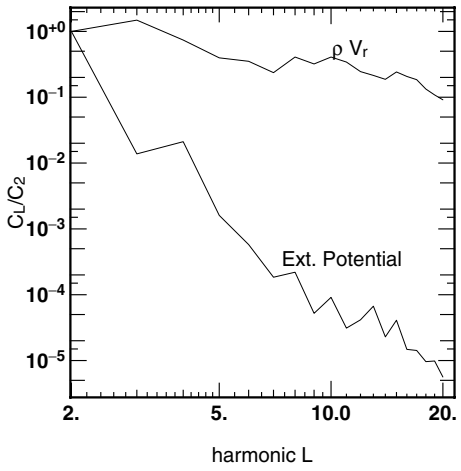

Figure 10. A comparison between the angular power spectrum of $\rho v_{\rm r}(\mathbf{\Omega})$ and $\psi^{\rm e}(\mathbf{\Omega})$ for our template halo (the two fields are shown in Fig. 9). The two power spectra C_ℓ are normalized by C_2, i.e. the quadrupole contribution. The slope of the potential's power spectrum is clearly stronger. Large scales (i.e. small-ℓ values) dominate the angular distribution of $\psi^{\rm e}(\mathbf{\Omega})$, as expected.

as discussed in Aubert et al. (2004). Each of them consists of a $50\,h^{-1}$ Mpc^3 box containing 128^3 particles. The mass resolution is $5 \times 10^9\,{\rm M}_\odot$. A ΛCDM cosmogony ($\Omega_{\rm m} = 0.3$, $\Omega_\Lambda = 0.7$, $h = 0.7$ and $\sigma_8 = 0.928$) is implemented with different initial conditions. These initial conditions were produced with GRAFIC (Bertschinger 2001), where a BBKS (Bardeen–Bond–Kaiser–Szalay; Bardeen et al. 1986) transfer function was chosen to compute the initial

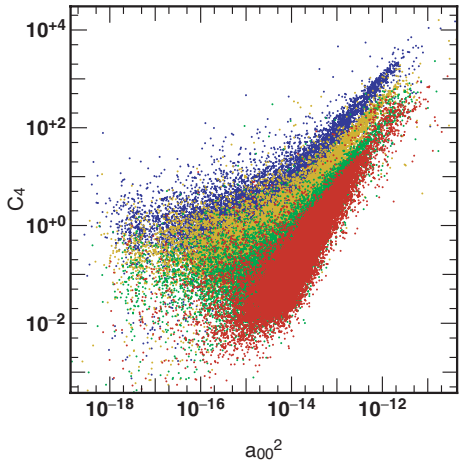

Figure 11. Scatter plot of $C_4^{\varpi_\rho}$ versus a_{00}^2 measured at lookback times $t = 7.8$ (red), 5.6 (green), 4.0 (yellow) and 2.9 (blue) Gyr. The quantity a_{00} scales as the average accretion rate of the haloes while $C_4^{\varpi_\rho}$ scales as the contribution of $\ell = 4$ structures in the flux density of mass measured on the sphere. This plot illustrates how a threshold on the accretion rate affects in a non-trivial way the typical clustering measured for ϖ_ρ. In particular, one should note how $C_4^{\varpi_\rho}$ remains constant at recent times for low accretion rates.

power spectrum. The initial conditions were used as inputs to the parallel version of the tree code GADGET (Springel, Yoshida & White 2001). The softening length was set to 19 h^{-1} kpc.[3] The halo detection was performed using the halo finder HOP (Eisenstein & Hut 1998). The density thresholds suggested by the authors ($\delta_{\rm outer} = 80$, $\delta_{\rm saddle} = 2.5\delta_{\rm outer}$, $\delta_{\rm peak} = 3.\delta_{\rm outer}$) were used.

4.2 Selection criteria

As shown in Aubert et al. (2004), the completion range in mass of the simulations spans from 3×10^{12} to $3 \times 10^{14}\,{\rm M}_\odot$. Since the emphasis is on $L_\star$ galaxies, the survey is focused mainly on galactic haloes and light clusters, only haloes with a mass smaller than $10^{14}\,{\rm M}_\odot$ at $z = 0$ were considered. The interest is for haloes already 'formed', i.e. which will not experience major fusions anymore. To satisfy these requirements, the focus is on the last 8 Gyr (redshifts $z < 1$ in a ΛCDM cosmogony). Since the history of a given halo is followed by finding its most massive progenitor, it is required not to accrete more than half its mass in a two-body fusion. As a final safeguard, a halo is rejected if it accretes more than $5 \times 10^{12}\,{\rm M}_\odot$ between two time-steps (i.e. per 500 Myr, see the next section). This mass corresponds approximately to the smallest haloes considered at $z = 0$. The final range of mass of haloes which satisfy these criteria is $\sim 5 \times 10^{12}$–$10^{14}\,{\rm M}_\odot$, the fraction of rejected haloes being ∼20 per cent. Clearly, such a priori selection criteria will modify the distributions of measured values and the related biases may be difficult to predict. For instance, Fig. 11 shows the scatter plot of the contribution of $\pi/(\ell = 4) = 45^\circ$ fluctuations to ϖ_ρ field versus a_{00}, i.e. the accretion rate. It appears from this plot that modifying the threshold for the accretion will modify the average angular scale of ϖ_ρ in a non-trivial way. Since only a small fraction of haloes are rejected, the biases are expected to be moderate, but as for now their

[3] A second set of simulations with a resolution increase by a factor of 2^3 (respectively 2^6) was carried in order to investigate the convergence of some measurements (see Section 6.2.2).

impact cannot be estimated accurately on the average source or its moments.

Let us emphasize that the above selection criteria should be added to those corresponding to the simulations themselves. Aside from the fact that a 50 $\mathrm{Mpc}^3\,h^{-1}$ box size implies a limited range of mass, the universe described in these simulations is more homogeneous than it should be, since each box must satisfy a given mean density. In other words, the probability of rare events is reduced. This effect should not influence the number of haloes with high accretion rate, since strong accretions are rejected a priori. On the other hand, it should influence the number of objects which experience low accretion history, which are probably less numerous in our simulations than in larger simulated volumes since voids are less likely. Furthermore, the intrinsic mass resolution sets a minimum accretion rate equals to one particle mass ($5 \times 10^9\,\mathrm{M}_\odot$) per time interval. One could imagine an object with a mass smaller than the particle's mass which would not be included in the simulation at the current resolution. Furthermore, an object with a mass equals to a few times the minimum mass is to be considered as diffuse accretion. Finally, this mass resolution is related to the spatial resolution, which limits intrinsically the angular description of fluxes on the virial sphere. For a given type of simulation, all these effects cannot be avoided and reduce the representability of the following measurements.

In short, this strategy involves a bias in mass, redshift, resolution and strength of a merging event. However, these biases should only influence somewhat extreme realizations (related to e.g. very low accretion or equal mass mergers) of the source or the external potential and since the focus is on the typical scales, presumably related to moderate interactions, hopefully they should not significantly affect the measurements.

4.3 Reduction procedure

In the following discussion, most of the distances (respectively velocities) will be expressed as functions of the virial radius R_{200} (respectively the circular velocity V_c) measured at $z = 0$. These quantities are related to the halo's virial mass by

$$V_\mathrm{c} = \sqrt{\frac{G M_{200}}{R_{200}}}. \tag{51}$$

Here $M_{200} = M(r < R_{200})$. The mass dependence of R_{200} and V_c is given in Fig. 12 and may be fitted by

$$R_{200} = 537 M^{1/3}\ , \quad V_\mathrm{c} = 400 M^{1/3}, \tag{52}$$

where R_{200} is expressed in (h^{-1} kpc), V_c in km s^{-1} and M in units of $10^{13}\,\mathrm{M}_\odot$. Here M stands for the total mass of the halo, returned by the halo finder HOP. In equation (52), R_{200} and V_c appear to be strongly correlated to the final masses of haloes, the few outliers being related to external subhaloes or peculiar halo geometries. Since the selection criteria are quite restrictive, most of the haloes experience the same relatively quiet history of accretion and account for the lack of scatter.

The simulations in that redshift interval involved 15 snapshots sampled with $\Delta(\log z) = \mathrm{cst}$ for $z \leqslant 1$ down to $z = 0.1$ plus a snapshot at $z = 0$. The gap between the last snapshot and the second to the last is nearly 1.4 Gyr. As a consequence, the assumption of ballistic trajectories is not valid anymore (see the Appendix). Simulations were resampled in 15 bins distributed regularly in *time* (i.e. not in redshift) using the procedure described in Section 3.2: the corresponding time-step is ∼500 Myr. To take into account the last gap, results obtained from the last three 'new' bins (which cover the last 1.4 Gyr) were averaged into a single bin centred on 0.8 Gyr.

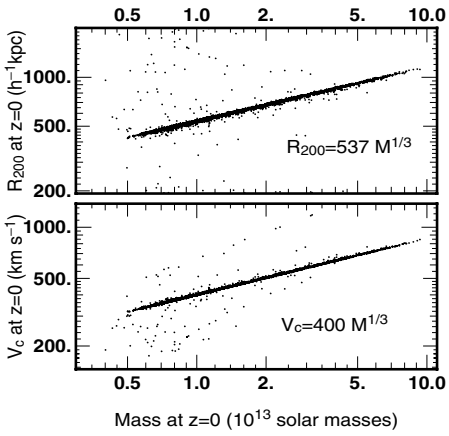

Figure 12. Virial radii (R_{200}) and circular velocities (V_c) as functions of haloes final masses. The quantities have been measured at redshift $z = 0$. Scaling relations between R_{200} or V_c and the final mass are also given.

The source coefficients, $c^{\boldsymbol{m}}_{\alpha,\boldsymbol{m}'}(t)$, were computed following the procedure described in Section 3.4. Maximum harmonic orders were set to $\ell_{\max} = 50$ for the position–angular description. For a typical halo with $R_{200} = 500$ kpc, $\ell_{\max} = 50$ corresponds to a spatial scale of 30 kpc, i.e. equals to 1.5 times the spatial resolution of the simulation. The harmonic description of the velocities angular dependence is restricted to $\ell'_{\max} = 15$. The velocity amplitude is projected on a Gaussian basis which involves 25 functions regularly spaced from $v/v_\mathrm{c} = 0$ to 1.5 with a rms of 0.03. These parameters allow a satisfying reproduction of distributions computed from particles.

The external potential coefficients, $b_{\boldsymbol{m}}(t)$, were computed following the procedure described in Section 3.4. Only particles within a 4-Mpc physical sphere centred on the halo are taken into account. Maximum harmonic orders were set to $\ell_{\max} = 20$.

A set of 100 simulations have been fully reduced allowing us to compute $c^{\boldsymbol{m}}_{\alpha,\boldsymbol{m}'}(t)$ and $b_{\boldsymbol{m}}(t)$ for 15 000 haloes. Since a well-defined (if only biased) sample of histories of haloes was constructed in our simulations, it may be projected on our basis, to compute the external potential and the flux density of mass, following Section 3.4. Let us now characterize the corresponding coefficients, via one-point (Section 5) and two-point (Section 5) statistics.

5 ONE-POINT STATISTICS

In this section, let us first describe the evolution and the statistical distributions of the global properties (i.e. integrated over the sphere) of the source and the potential. Let us discuss the evolution of the mean potential, of the mass flux $\Phi^\mathrm{M}(t)$ and the kinematical properties of s^e via the velocity distribution $\phi(v)$ and the impact parameter distribution $\vartheta(b)$.

Let us then describe in turn the statistical PDF, mean and variance of the integrated fluxes, their corresponding flux densities and finally their mean kinematical features, following the steps of Section 3.4.

5.1 Mean external potential

The mean external potential on the sphere is actually somewhat meaningless but is being used as a normalization value for potential

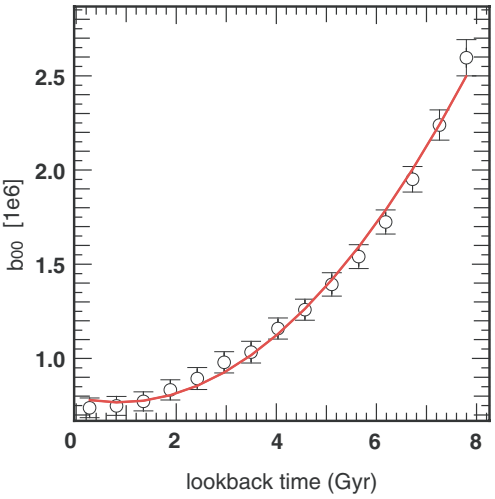

Figure 13. The time evolution of the monopole component of the external potential, $b_{00}(t)$. The time evolution is fitted by a second-order polynomial $-$ $b_{00}(t) = 35\,948 * t^2 - 61\,480.7 * t + 793\,067$. Lookback time t is expressed in Gyr, while b_{00} coefficients are expressed in units of GM/R. M is expressed in $10^{10}\,\mathrm{M}_\odot$, R in kpc h^{-1} and $G = 43\,007$ in internal units.

fluctuations (see Section 6.1). Because of isotropy, the mean potential is seen as a monopole and only the $b_{00}(t)$ coefficient is statistically different from zero. Furthermore, following equation (24), the three-dimensional potential component induced by the monopole is a constant potential throughout the sphere volume. As a consequence, it influences the halo's dynamics only through its temporal variation.

The time evolution of the $\langle\langle b_{00}\rangle\rangle$ coefficient is given in Fig. 13. The $b_{00}(t)$ distribution exhibits a tail due to large $-$ b_{00} values and is better fitted with a lognormal distribution than with a normal distribution (see Fig. C1). Hence, $\langle\langle b_{00}\rangle\rangle$ stands for the most probable value of the lognormal fitting distribution.[4] The evolution shown in Fig. 13 reflects the measurement procedure. Given that the potential is computed from all the particles contained within a fixed physical volume, the overall expansion implies that particles tend to exit the measurement volume with time. In other words, the average density in the measurement volume decreases with time. This effect leads naturally to the decline of the average potential within the virial sphere due to external material.

5.2 Mass flux: $\Phi^M(t)$

At each time-step, the $a_{0,0}$ distribution is fitted by a Gaussian function with mean $\langle a_{0,0}\rangle$ (see also Fig. C3). This Gaussian hypothesis is clearly verified for low redshifts while strong accretion events give rise to a tail in the $a_{0,0}$ distribution at high z. At these epochs (lookback time $t > 7$ Gyr), the Gaussian fit tends to slightly overestimate the mode position. Yet the Gaussian hypothesis remains a good approximation of the distribution, while the time evolution of the Gaussian mean value $\langle a_{0,0}\rangle$ (t) represents well the evolution of the mode of $a_{0,0}$.

The time evolution of the average flux of matter through the sphere, $\Phi^{\mathrm{M}}(t) = \overline{\varpi_\rho}$, is directly derived from the evolution of the monopole (see equation 43) and is shown in Fig. 14. It can be fitted by

$$\Phi^{\mathrm{M}}(t) \equiv \langle\overline{\varpi_\rho}\rangle(t) = -0.81t^3 + 10.7t^2 - 19.3t + 17.57, \qquad (53)$$

where $\Phi^{\mathrm{M}}(t)$ is in units of $\mathrm{M}_\odot\,\mathrm{Myr}^{-1}\,\mathrm{kpc}^{-2}$ and lookback time t is expressed in Gyr. As expected, the average quantity of material accreted by haloes decreases with time. For $z < 1$, a large fraction of the objects of interest are already 'formed' and only gain matter through the accretion of small objects or diffuse material. In a hierarchical scenario, such a source of matter becomes scarcer, inducing a decrease in the accretion rate. Furthermore, recall that $\Phi^{\mathrm{M}}(t)$ is measured as a net flux, i.e. the outflowing material may cancel a fraction of the infalling flux. Therefore, the decrease with time may also be the consequence of an increasing contribution of outflows: the measurement radius $R_{200}(z = 0)$ becomes the actual virial radius of the halo as time goes by, i.e. the radius where the inner material is reprocessed and where outflows are susceptible to be detected.

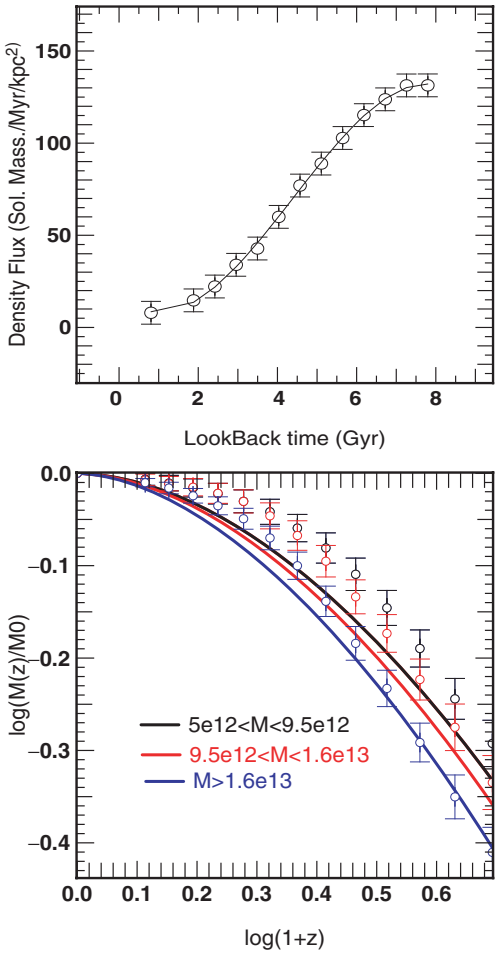

Figure 14. Top: the time evolution of the average flux density of matter through the virial sphere, $\langle\Phi^{\mathrm{M}}(t)\rangle = \langle\overline{\varpi_\rho}\rangle(t)$ (*symbols*). Bars stand for 3σ errors. Here Φ^{M} (t) is computed directly from a_{00} coefficients following equation (56). Its time evolution is fitted by a third-order polynomial (solid line). Bottom: the MAH $\log M(z)/M(z = 0)$ for three different classes of masses. Masses are expressed in solar masses. Symbols represent the median value of $\log M(z)/M(z = 0)$ within each classes. Lines represent the fitting function suggested by van den Bosch (2002b). Even though the global behaviour is reproduced by the fitting functions, the measured accretion rate is systematically smaller. This discrepancy has already been noted by van den Bosch (2002b).

[4] Since the measured distribution is quite peaked, fits made with a normal distribution (not shown here) return a very similar time evolution of the mode position.

As a check, the average mass accretion history (hereafter MAH) of the haloes was computed. The MAH $\Psi(t)$ is defined as

$$\Psi(t) \equiv \frac{M(t)}{M(z=0)}, \tag{54}$$

where $M(z)$ is the halo's mass at a given instant. Using the extended Press–Schechter formalism, van den Bosch (2002b) showed that haloes have an universal MAH, fitted by the following formula:

$$\log[\Psi(M(z=0),t)] = -0.301\left[\frac{\log(1+z)}{\log(1+z_f)}\right]^{\nu}, \tag{55}$$

where z_f and ν are two parameters which depend on the considered class of mass only. These two parameters are found to be correlated and for instance Wechsler et al. (2002) found a similar relation using a single parameter. For each halo, its mass evolution $M(t)$ was computed from its final mass $M(z=0)$ and its integrated flux of matter $\Phi^{\rm M}(t)$:

$$M(t) = M(t=0) - 4\pi R_{200}^2 \int_{t=0}^{t} {\rm d}t\,\Phi^{\rm M}(t). \tag{56}$$

From equation (54), $\Psi(t)$ was computed for each halo. The *median* value of $\Psi(t)$ for three classes of mass was compared to the fit suggested by van den Bosch (2002b) (see Fig. 14). For the three classes, the agreement with the fitting formula is qualitatively satisfying: the three measurements evolve in the expected manner while their relative positions are the same as the relative positions of the three fits. However, our measurements are quantitatively inconsistent with the three curves. At low redshift, $\Psi(t)$ is systematically larger than the expected value (i.e. the accretion rate is *smaller*). The median mass at $z=1$ is well recovered even though the two methods disagree slightly quantitatively. In other words, our measurements overestimate the accretion at high redshift and underestimates at low redshift. This may be related to the measurement procedure through the sphere: at higher redshift, accreted material is assumed to be added to the biggest progenitor, even though it has not yet reached the central object and its mass is overestimated. Still, this material ends up in the most massive progenitor and the final mass is recovered. Note that since specific selection criteria were applied, these haloes may not be completely representative of the whole halo population. Finally, recall that the *median* value of $\Psi(t)$ was represented here because of strong outliers, while the fitting formula is given for the *average* MAH (extracted from merger trees). A similar discrepancy between the extended Press–Schechter theory and the results obtained from numerical simulations had already been noticed by van den Bosch (2002b) and Wechsler et al. (2002). In particular, van den Bosch (2002b) found that the Press–Schechter models tend to underestimate the formation time haloes compared to simulations. Clearly, our measurements seem to confirm this discrepancy. Since the global behaviour of MAHs is recovered and since the median mass at $z=1$ is recovered, it is concluded that the measure of $\Phi^{\rm M}(t)$ through the virial sphere reproduces the accretion history of haloes.

5.3 Mean kinematics

Let us now turn to the kinematical properties of the flow, while averaging the source over the virial sphere.

5.3.1 probability distribution of the modulus of velocities

Given the source coefficients $c^{\boldsymbol{m}}_{\alpha,\boldsymbol{m}'}$, the average velocity distribution $\langle\varphi(v,t)\rangle$ (defined by equation 19) is easily computed since it only involves $\langle c^0_{\alpha,0}(t)\rangle$. The ensemble average of $\langle c^0_{\alpha,0}\rangle$ and the related ensemble dispersion $\sigma(c^0_{\alpha,0})(t) \equiv \langle(c^0_{\alpha,0} - \langle c^0_{\alpha,0}\rangle)^2\rangle$ are derived by fitting the $c^0_{\alpha,0}(t)$ distribution by a Gaussian function. From these two quantities, it follows

$$\langle\varphi(v,t)\rangle = 4\pi v^2 \sum_{\alpha} g_\alpha(v)\left\langle c^0_{\alpha,0}\right\rangle, \tag{57}$$

and

$$\sigma[\varphi(v,t)] = 4\pi v^2 \sqrt{\sum_{\alpha} g_\alpha(v)^2 \sigma\left(c^0_{\alpha,0}\right)^2}, \tag{58}$$

which are, respectively, the ensemble average and rms of the velocity distribution. The time evolution of $\langle\varphi(v,t)\rangle$ is given in Figs 15 and 16. Errors on $\langle\varphi(v,t)\rangle$ are computed as

$$\Delta[\langle\varphi(v,t)\rangle] = 3\frac{\sigma[\varphi(v,t)]}{\sqrt{N_{\rm haloes}}}. \tag{59}$$

At 'early times' ($t > 5$ Gyr), the distribution is unimodal with a maximum around $0.7V_{\rm c}$ ($z=0$). No outflows can be detected at

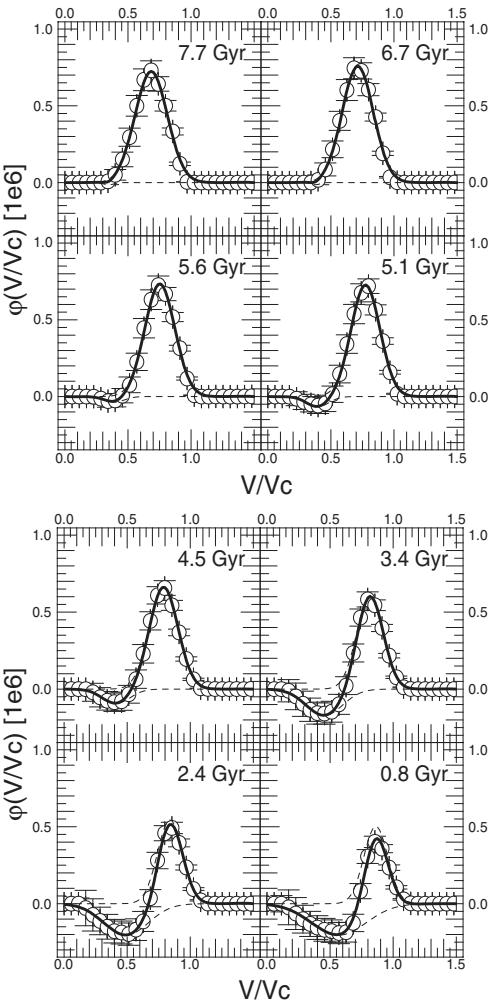

Figure 15. The time evolution of the average velocity distribution, $\langle\varphi(v,t)\rangle$, defined in equation (19), for $z<1$ (*symbols*). Ages are expressed as lookback times (i.e. $t=0$ for $z=0$). Velocities are given relative to the halo's circular velocity at $z=0$. The unit in y-axis is $5\times10^9\,{\rm M}_\odot\,{\rm kpc}^{-2}\,2\,{\rm Myr}^{-1}/V_{\rm c}$. Error bars stand for 3σ errors. Here $\varphi(v)$ is fitted by the sum of two Gaussians with opposite signs (solid line). Each Gaussian contribution is also shown (dashed lines).

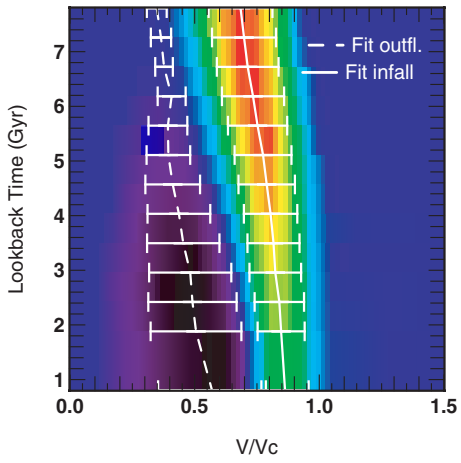

Figure 16. The time evolution of the average velocity distribution in the t–V/V_c plane. Red (online) colours stand for positive values of the distribution (i.e. infall), while blue (online) colours stand for negative ones (i.e. outflows). Each of these components is fitted by a Gaussian function in the V/V_c space. The time evolutions of the mean of the Gaussians are given by the two lines (*solid* for infall, *dashed* for outflows). The rms of Gaussians are also shown as bars.

any velocity and the infalling dark matter dominates. At later times, $\langle\varphi(v,t)\rangle$ drops below zero for velocities around $0.4V_c$ ($z=0$). Outflows dominate at 'low' velocities. Meanwhile, the amplitude of the previous peak decreases and shifts to higher velocities. The fraction of infall relative to the total amount of material passing through the sphere drops from 1. to 0.6 between $t=8$ and 0.8 Gyr.

This behaviour is likely to be due to our measurement at a *fixed* radius, $R_{200}(z=0)$. At 'early times', this measurement radius is bigger than the actual virial radius of haloes. Thus no sign of 'virialization' (outflows consecutive to accretion) is detected. Later, the actual R_{200} gets closer to the measurement radius. Outflows pass through the measurement radius as a sign of internal dynamical reorganization. The fact that accretion intrinsically decreases with time would provide another explanation of this trend. This decrease can actually be traced in Figs 15, 16 and D1.

The global behaviour of $\langle\varphi(v,t)\rangle$ can be modelled by summing two Gaussians representing the infalling and outflowing components:

$$\langle\varphi(v,t)\rangle = \frac{q_{\iota,3}(t)}{q_{\iota,2}(t)\sqrt{2\pi}}\exp\left\{-\frac{[v-q_{\iota,1}(t)]^2}{2q_{\iota,2}(t)^2}\right\} + \frac{q_{o,3}(t)}{q_{o,2}(t)\sqrt{2\pi}}\exp\left\{-\frac{[v-q_{o,1}(t)]^2}{2q_{o,2}(t)^2}\right\}. \quad (60)$$

Subscripts ι and o stand for infall and outflow. Note that $q_{\iota,3}(t)\geqslant 0$ and $q_{o,3}(t)\leqslant 0$. The coefficient time evolution is given in Fig. D1, where t can be expressed in Gyr and $\varphi(v,t)$ in $5\times 10^9\,\mathrm{M}_\odot\,\mathrm{kpc}^{-2}\,\mathrm{Myr}^{-1}/V_c$. Examples of fits are shown as solid lines in Fig. 15. Note that all the six coefficients evolve roughly linearly with time (see Fig. D1). Their linear fitting parameters are given in Table D1. Using equation (60) and the linear parametrization of the Gaussian coefficients, $\langle\varphi(v,t)\rangle$ is reproduced accurately. The only restriction concerns the negative amplitude of the Gaussian ($q_{o,3}$) which should not be greater than 0. Since this condition is not naturally satisfied by a linear fit, it should be set manually.

The evolution of the relative positions of two Gaussians is given in Fig. 16. For $t>5$ Gyr, it is consistent with the 'no outflow' hypothesis, the amplitude of the negative Gaussian being close to zero at this epoch. Both Gaussians mean values seem to drift to higher velocities as a function of time. Even though the relative velocity of accreted material is determined by the initial conditions (namely large-scale clustering), the velocity of an infalling satellite should partly reflect the properties of the accreting body. A dense massive halo will not accrete like a fluffy light one. In other words, the velocity of infalling material should reflect the actual circular velocity of the accreting body. As a consequence, it is expected that accretion velocity drifts with time towards V_c ($z=0$).

Furthermore, the mean values of both Gaussians evolve roughly linearly over the whole time range with comparable rate of change (see Fig. D1 and the following discussion). As a consequence, their relative positions remain roughly constant (see Fig. 16). This indicates that these two components may be physically related, outflows being the consequence of a past accretion. Mamon et al. (2004) mention the existence of a *backsplash* population, rebounding through the virial radius and this population is known to have a different velocity (e.g. Gill et al. 2004). The outflows detected via our description of the source are consistent with this backsplash component. The difference in velocity may be explained if outflows are representative of an earlier accretion with a velocity typical of earlier times. Also past accreted material is influenced by the halo's internal dynamics. Its velocity distribution would be 'reprocessed' (e.g. via dynamical friction, tidal stripping or phase mixing) to lower velocities as the material exits through the measurement radius.

However, recall that the distribution shown here is a 'net' distribution. In other words, it is quite plausible that an outflowing component may be completely cancelled by an infalling component which has an exact opposite distribution. This effect is illustrated in Fig. 17, where the velocity distribution of infall and outflows is being shown separately. This distribution has been computed from 300 haloes at $t=2.3$ Gyr. This distribution is quite representative of the average ones, except a few high velocities events which skew the distribution of the infalling component and which are induced by outliers. If the Gaussian fits are removed from these two separate distributions, two almost identical distributions appear for the two components, centred on $V/V_c\sim 0.6$. These two identical distributions are related to the virialized component of infall, which already interacted with the inner region of the halo. The overall shape of these two distributions may provide insights on the typical dynamical state in the haloes' inner regions.

5.3.2 *Impact parameters and incidence angles*

The average distribution of incidence angle, $\langle\vartheta(\Gamma_1,t)\rangle$ has been computed following the same procedure described above for $\langle\varphi(v,t)\rangle$. Defining $\tilde{c}_{\ell'}(t)$ as

$$\tilde{c}_{\ell'}(t) = 2\pi\sqrt{4\pi}\sum_\alpha c_{\alpha,0,\{\ell',0\}}\left(\mu_\alpha^2+\sigma^2\right), \quad (61)$$

yields

$$\langle\vartheta(\Gamma_1,t)\rangle = \sum_{\ell'} Y_{\ell',0}(\mathbf{\Gamma})\langle\tilde{c}_{\ell'}(t)\rangle \quad (62)$$

and

$$\sigma(\vartheta(\Gamma_1,t)) = \sqrt{\sum_{\ell'} Y_{\ell',0}(\mathbf{\Gamma})^2\sigma(\tilde{c}_{\ell'}(t))^2}, \quad (63)$$

where $\langle\vartheta(\Gamma_1,t)\rangle$ and $\sigma(\vartheta(\Gamma_1,t))$ are derived by fitting the $\tilde{c}_{\ell'}(t)$ distribution by a Gaussian function. Errors on $\langle\vartheta(\Gamma_1,t)\rangle$ are computed

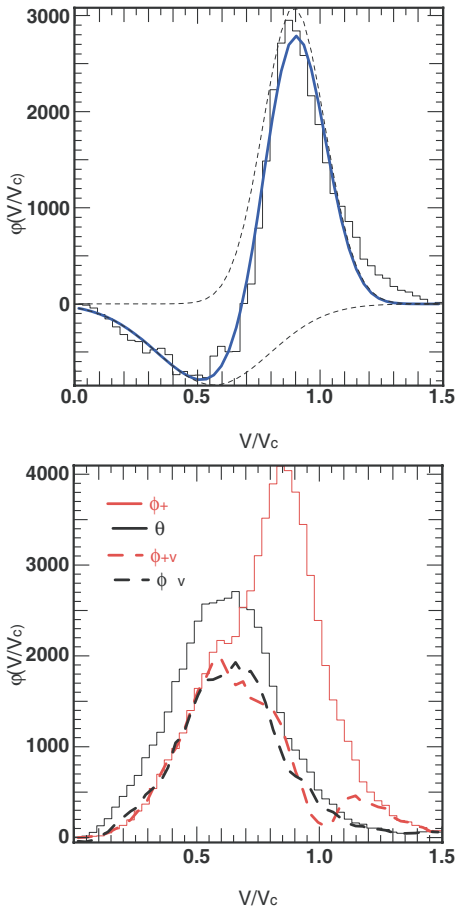

Figure 17. Top: the net velocities distribution (histogram) measured from 300 haloes at $t = 3.4$ Gyr. This distribution is the representative of the distribution computed from coefficients and averaged over 15 000 haloes. Velocities are given in circular velocity units, while units in y-axis are arbitrary. The two components are fitted by two Gaussians (dashed lines). Bottom: the separate velocities distribution of accretion (red histogram) and outflows (black histogram). The dashed curves represent the difference between these two distributions and their respective fits shown above. It results in two residual distributions, centred on the same velocity and displaying nearly the same shape. These two residual distributions describe the material which already experienced one passage through the virial sphere.

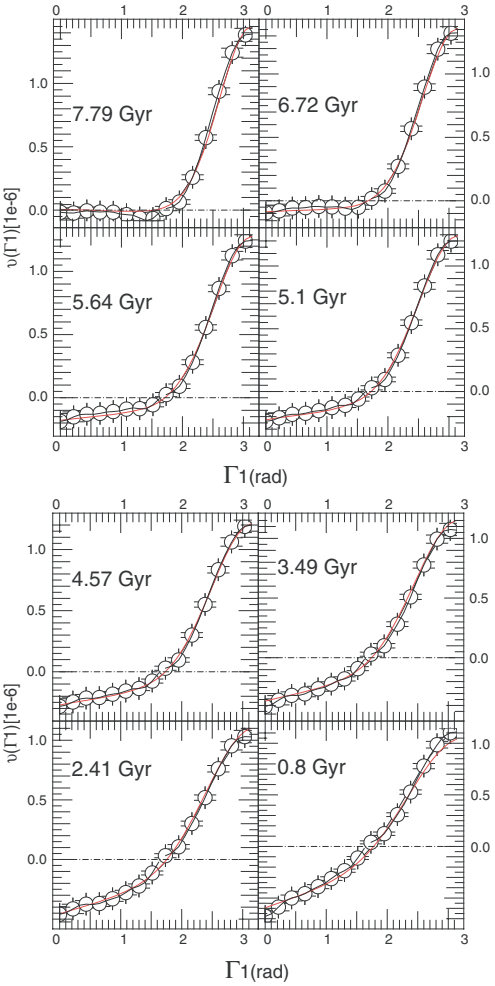

Figure 18. The time evolution (symbols) of the distribution of the average incidence angle Γ_1 $\langle\vartheta(\Gamma_1)\rangle$ is defined by equation (46). Ages are expressed as lookback time. Bars stand for 3σ errors. The unit in y-axis is 5 $\times$ 10^9 $M_\odot$ kpc^{-2} Myr^{-1}. Outflows are counted negatively, leading to negative values of $\langle\vartheta(\Gamma_1)\rangle$ for $\Gamma_1 < \pi/2$. The result of the model described in equation (64) is also shown (red line).

similarly to errors on $\langle\varphi(v,t)\rangle$ (see equation 59). The time evolution of $\langle\vartheta(\Gamma_1, t)\rangle$ is shown in Fig. 18. Since the impact parameter and the incidence angle are simply related by $b/R_{200} = \sin(\Gamma_1)$, $\langle\vartheta(b, t)\rangle$ is also easily computed (Fig. 19).

The infall ($\Gamma_1 > \pi/2$ or the upper branch in $\langle\vartheta(b, t)\rangle$ diagrams) is clearly mostly radial. The infalling part of the distribution peaks for $\Gamma_1 \sim \pi$ instead of having a uniform behaviour and this trend can be observed for all redshifts below 1. The distribution slightly widens with but remains skewed towards large values of Γ_1. In the $\langle\vartheta(b, t)\rangle$ representation, the higher branch becomes flatter with time. The outflows ($\Gamma_1 < \pi/2$ or lower branch in $\langle\vartheta(b, t)\rangle$ diagrams) are mainly undetectable at early times, as mentioned earlier. As time increases, the outflow contribution becomes stronger and radial orbits ($\Gamma_1 \sim 0$) also appear to be dominant. However, the behaviour of the 'outflowing' part of the $\langle\vartheta(\Gamma_1, t)\rangle$ distribution is almost linear and does not peak. Tangential orbits cannot be neglected for this component.

The evolution of $\langle\vartheta(\Gamma_1, t)\rangle$ can be fitted by the following parametrization:

$$\langle\vartheta(\Gamma_1, t)\rangle = \frac{p_0}{\sqrt{2\pi}p_1(t)} \exp\left[-\frac{(\Gamma_1 - \pi)^2}{2p_1(t)^2}\right] + p_2(t)\Gamma_1 + p_3(t), \quad (64)$$

where $p_0 = 2 \times 10^{-6}$ in our units. The 'infalling' part is modelled as a Gaussian, while the 'outflowing' part is fitted linearly. The time evolution of the three parameters $p_k(t), k = 1, 2, 3$, can be fitted by a linear evolution and the related linear parameters are given in Table D2. The evolution of $p_1(t)$ confirms that the 'infalling' part of the distribution, $\langle\vartheta(\Gamma_1, t)\rangle$ widens with time.

This result implies that the material experiences a circularization as it interacts with the halo. Consequently, orbits are more tangential as particles *exit* and *re-enter* the halo's sphere. Such an effect has already been measured by e.g. Gill et al. (2004). Dynamical friction would provide a natural explanation for this evolution of the orbits, but this argument is refuted by e.g. Colpi, Mayer & Governato (1999) or Hashimoto, Funato & Makino (2003). Gill et al. (2004) mention the secular evolution of haloes to explain this circularization: the

time evolution of the potential well induced by the halo would affect the orbits of infalling material and satellites. Other processes, such as tidal stripping or satellite–satellite interactions, may also modify the orbital parameters of dark matter fluxes. Clearly, the interactions between the infall and the halo drive this circularization, but the detailed process still has to be understood.

This dynamical circularization could also explain why the 'outflowing' part of the $\langle\vartheta(\Gamma_1)\rangle$ (or $\langle\vartheta(b)\rangle$) is flatter than the infalling one: by definition this component interacted with the halo in the past, unlike most of the infall. Finally, the Γ_1 or b representation explicitly separates infall and outflows. It implies that *virialized* particles which pass through the sphere do not 'cancel' each other and do contribute to the distributions. Such a 'relaxed' material is likely to have a non-zero tangential motion, flattening the distributions as its contribution becomes important. Since the actual size of the halo gets closer to the measurement radius as time advances, this component contributes more with time and its flattening effect on the incidence angle (or impact parameter) distributions should increase as well.

Fig. 20 presents a correlation between the velocity amplitude v and the impact parameter b, at four different instances and for both the infall and the outflow components. Considering these two components separately, no correlation can be found: the incidence does not depend on the amplitude of the first approximation. The only notable result comes from the fact that accreted material has systematically a higher velocity than outflows, which confirms the results obtained from the distribution of velocities only. Again, this effect is related to the separate origin of these two fluxes, accretion, being dominated by newly accreted material, and outflows, which were processed by the inner dynamics of haloes.

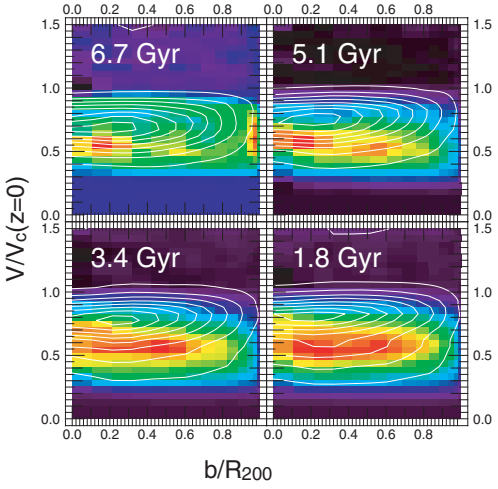

Figure 20. Top: the distribution, $\langle\wp(b, v)\rangle$, of particles in the (b, v) subspace at lookback time $t = 1.8$, 3.4, 5.1 and 6.7 Gyr; the infall (contour plot) and outflow (density plot) are represented separately. Beyond the bimodal feature, no residual correlation appears.

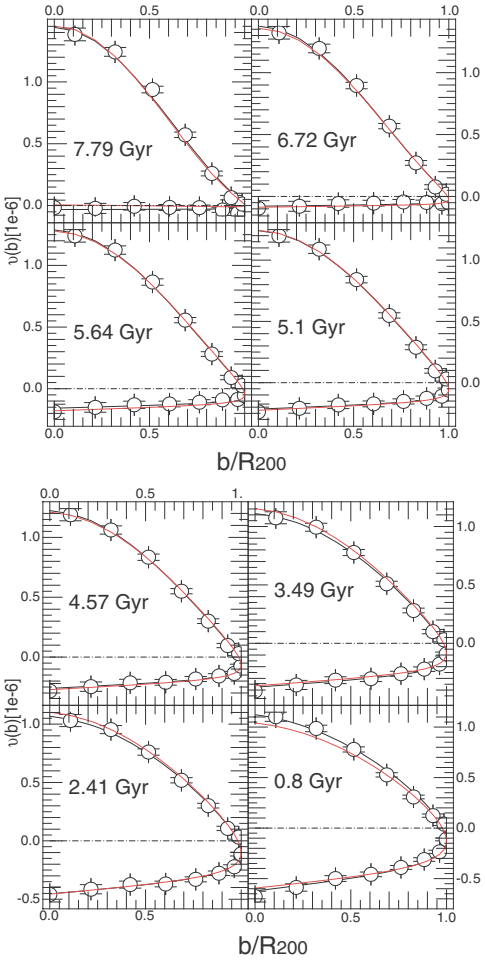

Figure 19. The time evolution (symbols) of the impact parameter b distribution $\langle\vartheta(b, t)\rangle$ is defined by equation (46). Ages are expressed as lookback time. Bars stand for 3σ errors. The unit in y-axis is 5×10^9 $M_\odot$ kpc^{-2} Myr^{-1}. The lower (respectively higher) branch is the $\langle\vartheta(b, t)\rangle$ distribution for outflows (respectively infall). The result of the model described in equation (64) is also shown (red line).

6 TWO-POINT STATISTICS

Let us now focus on the second-order statistics, through the correlations on the virial sphere. The two-point correlations are assessed through the angular power spectrum and the angulo-temporal correlation function for both the external potential, $\psi^{\rm e}$ and the first moment of the source term, i.e. the flux density of mass, ϖ_ρ.

6.1 External potential

6.1.1 Angular power spectrum

The potential's angular power spectrum $C_\ell^{\psi^{\rm e}}$ is computed for each halo from the $\tilde{b}_{\ell,m}$ coefficients (Aubert et al. 2004),

$$\tilde{b}_{\ell,m} \equiv \sqrt{4\pi}\left(\frac{b_{\ell,m}}{\langle b_{00}\rangle} - \delta_{\ell 0}\frac{b_{0,0}}{\langle b_{00}\rangle}\right), \tag{65}$$

related to the potential contrast

$$\delta_{[\psi^{\rm e}]}(\boldsymbol{\Omega}) \equiv \frac{\psi^{\rm e}(\boldsymbol{\Omega}) - \overline{\psi^{\rm e}}}{\langle\overline{\psi^{\rm e}}\rangle} = \sum_{\ell,m}\tilde{b}_{\ell,m}Y_{\ell,m}(\boldsymbol{\Omega}). \tag{66}$$

The probability distribution of $C_\ell^{\psi^{\rm e}}(t)$ was weighted as described in Appendix A. For each time-step and each harmonic ℓ, $C_\ell^{\psi^{\rm e}}$ was fitted by a lognormal distribution (see Fig. C2). Let us define $\langle\!\langle C_\ell^{\psi^{\rm e}}\rangle\!\rangle(t)$ as the mode of the fitting distribution. The time evolution of the external potential's power spectrum is shown in Fig. 21. Globally, the power spectrum is dominated by large scales and is quite insensitive to time evolution. However, two regimes may be distinguished. For

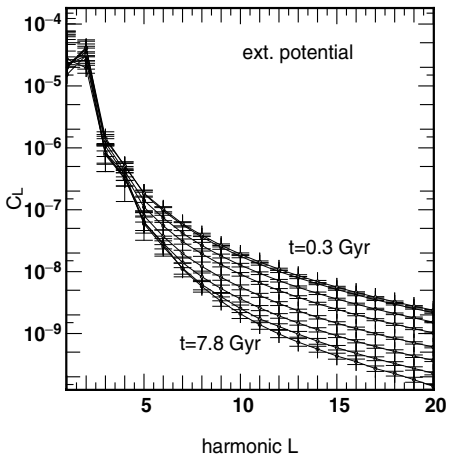

Figure 21. The angular power spectrum of the external gravitational potential $\psi^e(\mathbf{\Omega}, t)$. Symbols represent the *mode* of the $C_\ell^{\psi^e}$ distribution for each harmonic ℓ and each time-step. Times are lookback times. Bars stand for 3σ errors on the mode value. The large-scale contribution remains constant with time, while the small-scale contribution smoothly increases with time. The bump for the $\langle C_2 \rangle$ component indicates a strong quadrupolar configuration for $\psi^e(\mathbf{\Omega}, t)$.

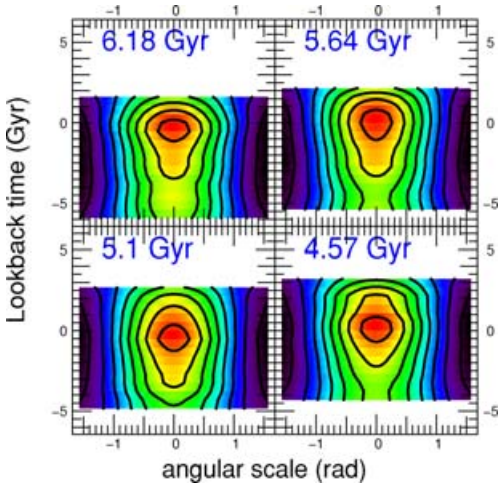

Figure 22. The angulo-temporal correlation function, $w^e(\theta, \Delta t) = \langle \delta_{[\psi^e]}(\mathbf{\Omega}, t) \delta_{[\psi^e]}(\mathbf{\Omega} + \Delta\mathbf{\Omega}, t + \Delta t) \rangle$. Blue (respectively red) colours stand for low (respectively high) values of the correlation. Isocontours are also shown. Large angular scale isocontours ($\theta \sim \pi/2$) have large temporal extent, due to the quadrupole dominance over the potential seen in the virial sphere.

low-order harmonics, $\langle\!\langle C_\ell^{\psi^e} \rangle\!\rangle(t)$ remains mostly constant. For smaller scales ($\ell > 5$), $\langle\!\langle C_\ell^{\psi^e} \rangle\!\rangle(t)$ increases along time. As a consequence, the power spectrum's amplitude does not change but its shape evolves while smaller scales become more important relative to larger scales.

These two regimes reflect the two-fold nature of tidal interactions of a halo with its environment. Small angular variations of the potential relate to small spatial scales and presumably track the presence of objects which are getting closer or going through the virial sphere. Since small-scale contribution increases, it suggests that these objects tend to get smaller with time. It would be consistent with the global decrease of the accretion rate, as long as the merger rate does not increase strongly during this epoch. However, the rise of small scales may also be related to an increasing contribution of weak and poorly resolved accretion events. In such a case, the isolated particles' contribution to the potential should be measured. This possibility is investigated in Section 6.2.

Meanwhile, large-scale fluctuations of potential ($\ell \leqslant 4$) may reflect the 'cosmic tidal field' resulting from the distribution of matter around the halo on scales larger than the radius of the halo. The amplitude of such a tidal field should remain fairly constant, as indeed measured. Furthermore, the peripheral distribution of matter is not spherically distributed but is rather elongated along some direction: haloes tend to be triaxial with their ellipsoid aligned with the surrounding distribution of satellites. The intersection of an elongated distribution of matter with the virial sphere would induce a quadrupolar component, as detected in our measurements. These two effects cannot be easily disentangled, since they actually are two sides of the same effect. Large-scale distribution of matter is responsible for both the 'cosmic tidal field' and the halo triaxiality (via the distribution of satellites). In other words, it is not clear whether the large-scale behaviour of $\langle\!\langle C_\ell^{\psi^e} \rangle\!\rangle(t)$ reflects the tidal field or the reaction of the halo to this tidal field.

6.1.2 *Angulo-temporal correlation*

6.1.2.1 Correlations and coherence time. To further investigate these two regimes of tidal interactions, let us compute the angulo-temporal correlation function of the external potential contrast, defined as

$$\langle\langle w^e(\theta, t, t + \Delta t) \rangle\rangle = \langle\langle \delta_{[\psi^e]}(\mathbf{\Omega}, t) \delta_{[\psi^e]}(\mathbf{\Omega} + \Delta\mathbf{\Omega}, t + \Delta t) \rangle\rangle, \quad (67)$$

which is related to $T_\ell^{\psi^e}$ (t, t + Δt) coefficients by

$$w^e(\theta, t, t + \Delta t) = \sum_\ell T_\ell^{\psi^e}(t, t + \Delta t)(2\ell + 1) P_\ell[\cos(\theta)], \quad (68)$$

where

$$T_\ell^{\psi^e}(t, t + \Delta t) \equiv \frac{1}{4\pi} \frac{1}{2\ell + 1} \sum_m \tilde{b}_{\ell m}(t) \tilde{b}^*_{\ell m}(t + \Delta t). \quad (69)$$

Here, θ stands for the angular distance between two points on the sphere located at $\mathbf{\Omega}$ and $\mathbf{\Omega} + \Delta\mathbf{\Omega}$. The $T_\ell^{\psi^e}(t, t + \Delta t)$ coefficients were computed for each halo and each pair of time-step, for each harmonic. The $T_\ell^{\psi^e}(t, t + \Delta t)$ distributions were fitted by a lognormal distribution and $\langle\!\langle T_\ell^{\psi^e}(t, t + \Delta t) \rangle\!\rangle$ was deduced from it. The corresponding $\langle\!\langle w^e(\theta, t, t + \Delta t) \rangle\!\rangle$ are shown in Fig. 22.

For large angular scales (>45°), isocontours remain open during the whole time range. Large scales have a long coherence time (∼5 Gyr) and are consistent with a 'cosmic tidal field' resulting from the large-scale distribution of matter. The latter is not expected to evolve significantly with time at our redshifts and the triaxiality of the halo is also a fairly constant feature. The innermost isocontours are closed around the measurement time t_1. Small angular scales (<45°) have shorter coherence time (∼1.5 Gyr). This is consistent with a contribution to the potential due to objects, where satellites pass by or dive into the halo and apply a tidal field only for a short period.

This difference between large and small scales can also be investigated through the time matrices of the $T_\ell^{\psi^e}(t, t + \Delta t)$ coefficients (see Fig. 23). The diagonal terms describe the time evolution of the angular power spectrum, $T_\ell^{\psi^e}(t, t) = C_\ell^{\psi^e}(t)$. A smooth (respectively peaked) distribution of values around the diagonal indicates a long (respectively short) coherence time. Clearly, different scales have different characteristic time-scales. The non-diagonal elements of the quadrupole matrix ($\ell = 2$) decrease slowly with the distance to the diagonal while the T_{20} matrix is almost diagonal. Not surprisingly, the smaller the angular scale, the smaller is the coherence

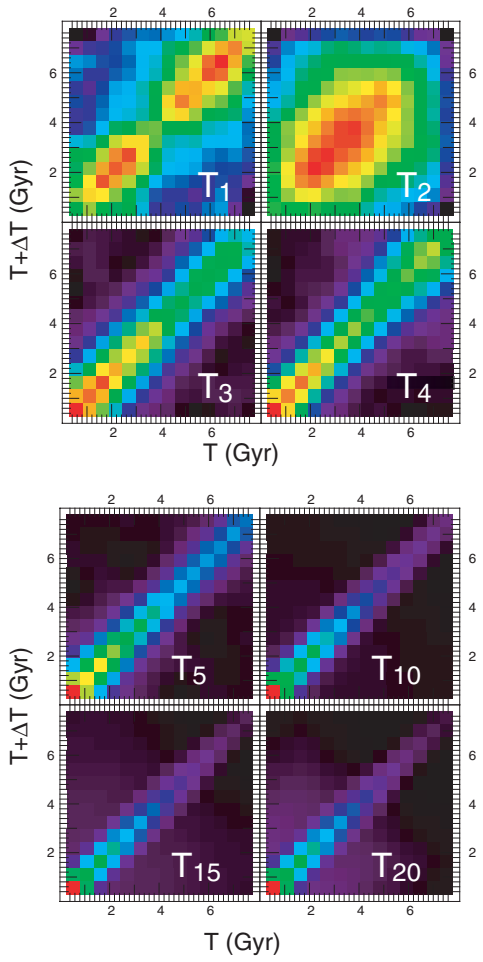

Figure 23. The time matrices of the $T_\ell^{\psi^e}(t, t+\Delta t)$ coefficients. Blue (respectively red) colours stand for low (respectively high) values of the coefficients. The diagonal terms are equal to the angular power spectrum, i.e. $T_\ell^{\psi^e}(t,t) = C_\ell^{\psi^e}(t)$. As can be seen from Fig. 21, fluctuations observed for T_1 are within the error bars. A smooth (respectively sharp) decrease of $T_\ell^{\psi^e}(t, t+\Delta t)$ with the distance to the diagonal implies a long (respectively short) coherence time. Here, coherence time decreases with angular scale.

time: a small 3D object passing through the sphere is likely to have a small angular size on the sphere.

For a given ℓ and a given t, the correlation coefficients $T_\ell^{\psi^e}$ can be fitted by a Lorentzian function defined by

$$T_\ell(t, t+\Delta t) = \frac{q_3^{\rm Te}(t)}{2/\pi} \frac{q_2^{\rm Te}(t)}{\left[\Delta t - q_1^{\rm Te}(t)\right]^2 + \left[q_2^{\rm Te}(t)/2\right]^2} + q_4^{\rm Te}(t), \quad (70)$$

where the characteristic time-scale, $\Delta T_{T_\ell^e}$, is given by $q_2^{\rm Te}(t)$ and the reference time t is equal to $q_1^{\rm Te}(t)$. Examples of fits are shown in Fig. 24.

For example, the time evolution of $\Delta T_{T_\ell^e} = q_2^{\rm Te}(t)$ is given in Fig. 24 for different ℓ values. Given the error bars, the characteristic time-scales are constant over time (except for the $\ell = 4$ mode). In the prospect of the regeneration of the potential, the stationary hypothesis can then be considered as valid for most of the angular scales. Meanwhile, the $\ell = 4$ potential fluctuations display a decreasing $\Delta T_{T_\ell^e}$ with time. The same effect exists at a 1σ level for $\ell = 5$. One interpretation would be that satellites achieve higher velocities along time: for a given typical size, a faster satellite would

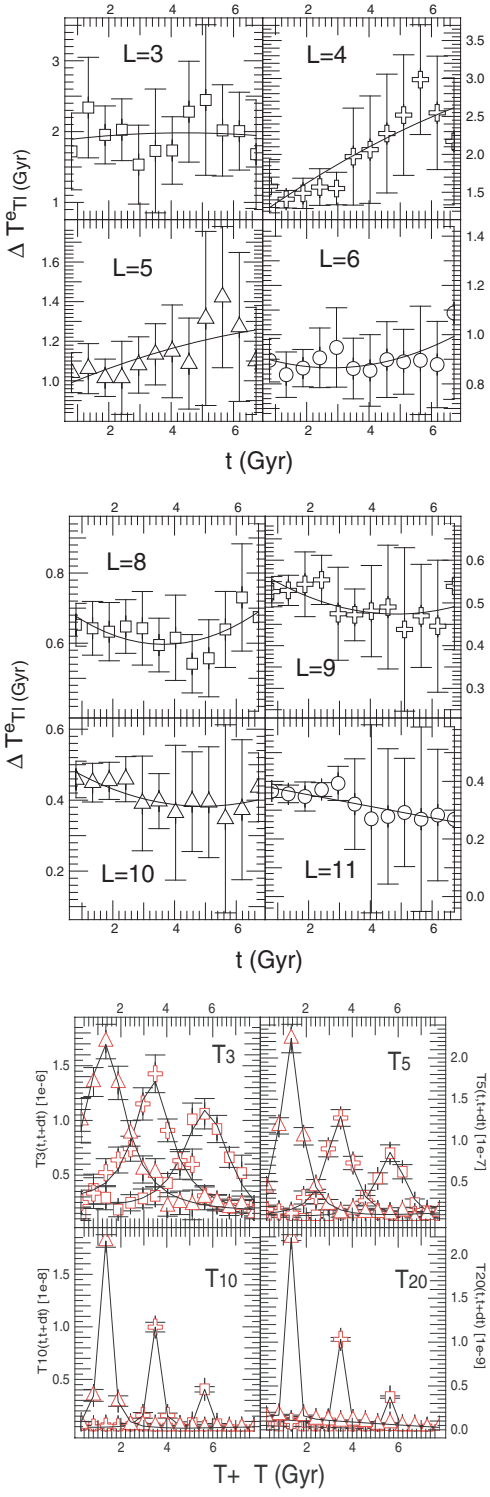

Figure 24. Top and middle: the time evolution of the characteristic time-scale $\Delta T_{T_\ell^e}$, obtained by fitting $T_\ell^{\psi^e}(t, t+\Delta t)$ with equation (70). Symbols are the measurements while bars stand for 3σ fitting error bars. The second-order fit of the time evolution of each $T_\ell^{\psi^e}$ is also shown. Except for the $\ell = 4$ and (marginally) for the $\ell = 5$ modes, no time evolution is observed. The time resolution is 0.53 Gyr. Bottom: examples of $T_\ell^{\psi^e}(t, t+\Delta t)$ fitted by Lorentzian functions.

spend less time to be accreted and the associated potential would be detected on a smaller time-scale. This picture is supported by the results shown in Section 5.3.1, where the mean velocity of infalling material increases along time. Another possibility would be that $\ell = 4$ fluctuations had a longer radial extent in the past. Since there is no reason for potential fluctuations to have such a property, one could imagine *successive* potential fluctuations which overlapped, leading to an apparent longer radial extent. This possibility is further investigated in the following paragraphs, by comparing the coherence time variation of the potential fluctuations to the evolution of the typical velocity of the infall.

6.1.2.2 Correlations without the dipole and the quadrupole. In order to focus on the coherence time of small angular scales, the correlation function $\langle\!\langle w^{\rm e}(\theta, t, \Delta t)\rangle\!\rangle$ was also computed without the dipole ($\ell = 1$) and the quadrupole ($\ell = 2$) component of the potential (see also equation 68). The angulo-temporal correlation function is shown in Fig. 25. Again, the isocontours of the correlation function are closed around $\Delta t = 0$. This shows that the potential on the sphere has a finite coherence time. In contrast to coherence times measured on the $T_\ell^{\psi^{\rm e}}$ coefficients, all the angular scales are mixed and the typical time-scales are those of structures as they are 'really' seen from a halocentric point of view, where 'potential blobs' appear and disappear on the sphere. To evaluate the related typical time-scale $\Delta T_{\psi^{\rm e}}$, $\langle\!\langle w^{\rm e}(\Delta\Omega, t, \Delta t)\rangle\!\rangle$ was fitted with a 2D function for different values of t. The model used is given by

$$\langle\langle w^{\rm e}(\theta, t, \Delta t)\rangle\rangle = q_6^{\rm we}(t) + \frac{q_5^{\rm we}(t)}{2\pi} \frac{q_4^{\rm we}(t)}{\left[\Delta t - q_3^{\rm we}(t)\right]^2 + \left[\frac{q_4^{\rm we}(t)}{2}\right]^2} \times \frac{\sin\left\{2\pi\left[\Delta\Omega - q_1^{\rm we}(t)\right]/q_2^{\rm we}(t)\right\}}{\Delta\Omega}, \quad (71)$$

where the angular dependence is fitted by a cardinal sine function while the time dependence is fitted by a Lorentzian function. Examples of 2D fits are shown in Fig. 25. The correlation function was also computed using only harmonics with $\ell \geqslant 4$, 5, 6, 7 and the same fitting procedure is applied. The evolution of the resulting characteristic time-scales $\Delta T_{\rm w^e} = q_4^{\rm we}(t)$ is shown in Fig. 26. Bars stand for 3σ fitting errors.

Note that $\Delta T_{\rm w^e}$ tends to decrease with time for every truncation order. The $\ell \geqslant 3$ and 4 correlation function displays a rise of $\Delta T_{\rm w^e}$ before it drops to lower values. Furthermore, $\Delta T_{\rm w^e}$ tends to decrease with $\ell_{\rm min}$, suggesting that the $\ell_{\rm min}$ contribution dominates each $w^{\rm e}$ reconstruction. Correlation functions with $\ell_{\rm min} \geqslant 5$ show marginal $\Delta T_{\rm w^e}$ variation but recall that our time resolution is 0.53 Gyr, hence any fluctuations on smaller scales should be taken in caution. Still, the 0.81-Gyr variation observed for $\ell \geqslant 3$ between $t = 5.1$ and 0.8 Gyr is significant and so is the variation observed for $\ell \geqslant 4$ (1.3 Gyr).

6.1.2.3 A longer coherence length. As mentioned above, the variation of the characteristic time-scale can be explained by the measured increase in mean velocity. Conversely, the decrease of coherence time may be the consequence of smaller potential blobs as time passes: a 'large' (three-dimensional) potential takes longer to

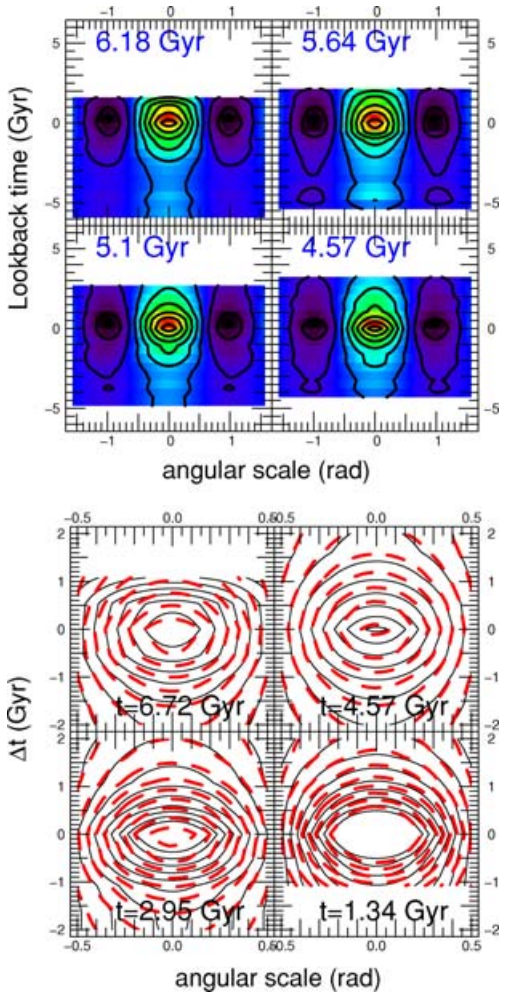

Figure 25. Top: the angulo-temporal correlation function, $w^{\rm e}(\theta, \Delta t) = \langle\delta_{[\psi^{\rm e}]}(\mathbf{\Omega}, t)\delta_{[\psi^{\rm e}]}(\mathbf{\Omega} + \Delta\mathbf{\Omega}, t + \Delta t)\rangle$. The dipole ($\ell = 1$) and the quadrupole ($\ell = 2$) components were removed. Blue (respectively red) colours stand for low (respectively high) values of the correlation. Isocontours are also shown. The main axes of the 'ellipses' centred on ($\Delta\mathbf{\Omega} = 0$, $\Delta t = 0$) give indications on the characteristic time and angular scales of $\psi^{\rm e}(\mathbf{\Omega}, t)$. Bottom: comparison between the measured 2D correlation function (solid lines) and the fit obtained using equation (71) (dashed lines).

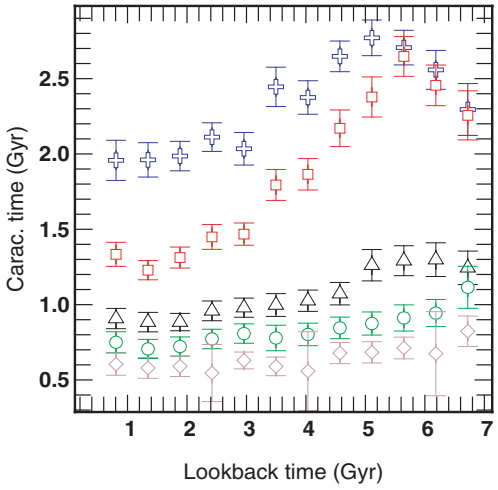

Figure 26. The cosmic evolution of the potential's coherence time. This characteristic time-scale is obtained by fitting the 2D correlation function $w^{\rm e}(\theta, \Delta t)$ with the function given in equation (71). The correlation function is computed using harmonics coefficients with $\ell \geqslant 3$ (*crosses*), $\ell \geqslant 4$ (*squares*), $\ell \geqslant 5$ (*triangle*), $\ell \geqslant 6$ (*circle*) and $\ell \geqslant 7$ (*diamonds*). Bars stand for 3σ fitting errors. The time resolution is 0.53 Gyr.

disappear than a smaller one. One crude approximation could be

$$\frac{L_1}{L_2} = \frac{V_1 \Delta T_1}{V_2 \Delta T_2}, \tag{72}$$

where L is the radial size, V is the radial velocity and ΔT is the coherence time of the potential blob. It is assumed that the $\ell \geqslant 4$ truncation is the representative of the potential due to infalling objects, i.e. $\Delta T_1/\Delta T_2 \sim 1.95$. Let us also consider that the radial velocity variation is equal to the one measured for the mean velocity of infall (see Section 5.3.1): $V_1/V_2 = 0.77$. Following equation (72), it suggests that $L_1 \sim 1.5 L_2$, i.e. the radial size decreases with time. The same calculation with $\ell \geqslant 3$ leads us to $L_1 \sim 1.1 L_2$: the results remain qualitatively the same. In other words, the coherence length was longer in the past and the velocity variation cannot explain the variation of coherence time. The only other way to explain a longer coherence length involves potential blobs falling successively through the sphere, coming from roughly the same direction. To induce a decreasing coherence time, these blobs would have to be either bigger before or more numerous. Such a crude picture is coherent with the measured decrease of accretion with time and the anisotropic nature of accretion by haloes (see e.g. Aubert et al. 2004; Knebe et al. 2004; Zentner et al. 2005).

6.2 Flux density of mass: $\varpi_\rho \equiv \rho v_r$

The mode $\langle\!\langle C_\ell^{\varpi_\rho} \rangle\!\rangle$ of the distribution of the ϖ_ρ angular power spectrum is computed using equations (41) and (42). In order to deal with adimensional quantities, the reduced harmonic coefficients, $\tilde{a}_{\ell,m}$, are defined as

$$\tilde{a}_{\ell,m} \equiv \sqrt{4\pi} \left(\frac{a_{\ell,m}}{\langle a_{00} \rangle} - \delta_{\ell 0} \frac{a_{0,0}}{\langle a_{00} \rangle} \right). \tag{73}$$

The accretion contrast, $\delta_{[\varpi_\rho]}$, and the $\tilde{a}_{\ell,m}$ coefficients are linked by

$$\delta_{[\varpi_\rho]}(\mathbf{\Omega}) \equiv \frac{\varpi_\rho(\mathbf{\Omega}) - \overline{\varpi_\rho}}{\langle \overline{\varpi_\rho} \rangle} = \sum_{\ell,m} \tilde{a}_{\ell,m} Y_{\ell,m}(\mathbf{\Omega}). \tag{74}$$

6.2.1 *Angular power spectrum*

Given $\langle a_{00} \rangle(t)$, the angular power spectrum $C_\ell^{\varpi_\rho}(t)$ is computed for each halo. At each time-step and for each harmonic order ℓ, the $C_\ell^{\varpi_\rho}(t)$ distribution was fitted by a lognormal distribution (see Fig. C4). The probability distribution of $C_\ell^{\varpi_\rho}(t)$ is weighted as described in Appendix A.

The evolution of $\langle\!\langle C_\ell^{\varpi_\rho}(t) \rangle\!\rangle$ with time is shown in Fig. 27. The shape of $\langle\!\langle C_\ell^{\varpi_\rho}(\mathrm{t}) \rangle\!\rangle$ remains mostly the same with time and is fitted by a simple function

$$\langle \langle C_\ell^{\varpi_\rho} \rangle \rangle(t) = q_1^{\varpi_\rho}(t) + \frac{q_2^{\varpi_\rho}(t)}{\left[\ell + q_3^{\varpi_\rho}(t)\right]^2}. \tag{75}$$

The time evolutions of $q_1^{\varpi_\rho}$, $q_2^{\varpi_\rho}$ and $q_3^{\varpi_\rho}$ are shown in Fig. D2 and can be fitted by decreasing the exponential

$$q^{\varpi_\rho}(t) = h + k \exp\left(-\frac{t}{u^2}\right). \tag{76}$$

Only the dipole ($\ell = 1$) harmonic does not fit with the previous functional form and is systematically lower than the contribution of the other harmonics. If particle velocities were measured in an absolute referential, the dipole strength would reflect the motion of the halo in the surrounding matter. Also strong mergers may cover a 180° angle on the sphere and would contribute to the dipole. Since velocities are measured in the rest frame of the halo and strong mergers are excluded, the dipole strength is substantially lowered, as is measured.

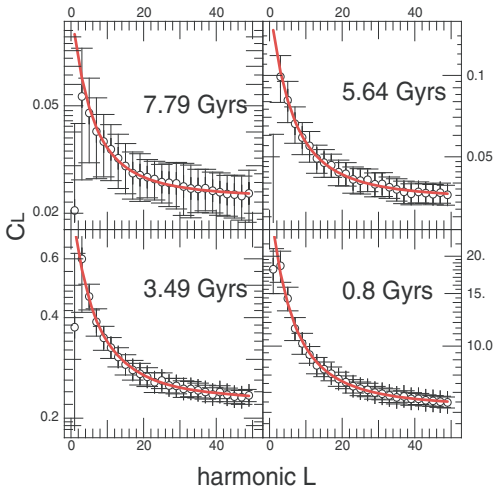

Figure 27. The average angular power spectrum, $\langle\!\langle C_\ell^{\varpi_\rho} \rangle\!\rangle(t)$, at $t = 0.8$, 3.5, 5.7, 7.8 Gyr (symbols). $\langle\!\langle C_\ell^{\varpi_\rho} \rangle\!\rangle(t)$ is taken as the mode of the lognormal function used to fit the C_ℓ distribution. Bars stand for 3σ errors. For a given ℓ, the corresponding angular scale is π/ℓ. $\langle\!\langle C_\ell^{\varpi_\rho} \rangle\!\rangle(t)$ may be fitted by a generic model given by equation (75) (solid line).

The values for h, k and u are given in Table D3. The offset $q_1^{\varpi_\rho}$ of $\langle\!\langle C_\ell^{\varpi_\rho}(t) \rangle\!\rangle$ increases with time. From equation (73), one can see that $\langle\!\langle C_\ell^{\varpi_\rho}(t) \rangle\!\rangle$ is proportional to the square of the accretion contrast. If the power spectrum experiences a global shift towards higher values with time, it implies that the accretion contrast increases with time. Since the average velocity does not vary strongly with time, this suggests that objects are getting denser with time. This effect is similar to the global increase of the 3D power spectrum $P(k)$ with time due to the density growth. Also, the $q_2^{\varpi_\rho}$ coefficient is found to evolve as $q_1^{\varpi_\rho}$. This illustrates the fact that the amplitude of $\langle\!\langle C_\ell^{\varpi_\rho}(t) \rangle\!\rangle$ remains mainly constant. The $q_3^{\varpi_\rho}$ coefficient should be seen as a typical scale and varies slightly from $q_3^{\varpi_\rho} = 6$ at $z = 1$ to $q_3^{\varpi_\rho} = 11$ at $z = 0.1$. $\langle\!\langle C_\ell^{\varpi_\rho}(t) \rangle\!\rangle$ becomes marginally 'flatter' as time passes, implying that small scales contribute more to the spatial distribution of $\varpi_\rho(\mathbf{\Omega}, t)$, consistently with the evolution of $\langle\!\langle C_\ell(t)^{\psi^c} \rangle\!\rangle$. The flat power spectrum measured for ϖ_ρ on small scales suggests that isolated particles contribute significantly and increasingly with time. In other words, the accretion becomes low enough to be poorly resolved in terms of particles.

6.2.2 *Resolution in mass and particle number*

In order to assess these environments/resolution effects, $\langle\!\langle C_\ell^{\varpi_\rho}(t) \rangle\!\rangle$ was computed for three different classes of mass (see Fig. 28) at a lookback time of 800 Myr. For the heaviest haloes, the power spectrum is peaked towards low-ℓ values. The contribution of large scales is quite important. For smaller masses, the power spectrum gets flatter and all scales almost contribute equally for the lightest class of mass. Recall that the harmonic decomposition of a Dirac function leads to $C_\ell =$ constant, thus a flat power spectrum indicates that isolated particles contribute significantly to the distribution of matter on the sphere. The relative behaviour of the three $\langle\!\langle C_\ell^{\varpi_\rho}(t) \rangle\!\rangle$ confirms that larger haloes still experience important mergers (i.e. on large scales) while small ones are in quiet environments at our simulation resolution. The effect of the mass resolution on the

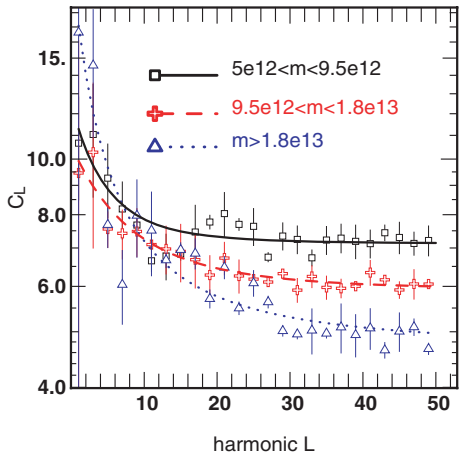

Figure 28. The average angular power spectrum, $\langle\langle C_\ell^{\varpi_\rho}\rangle\rangle(t)$, at $t = 0.8$ Gyr (symbols) for three different classes of masses. $\langle\langle C_\ell^{\varpi_\rho}\rangle\rangle(t)$ is taken as the mode of the lognormal function used to fit the $C_\ell^{\varpi_\rho}$ distribution. Bars stand for 3σ errors. Masses are expressed in solar masses. For a given ℓ, the corresponding angular scale is π/ℓ. The three measurements are fitted by equation (75) (solid line). The power spectrum gets flatter for small haloes. Accretion by small haloes is dominated by small objects or even isolated particles.

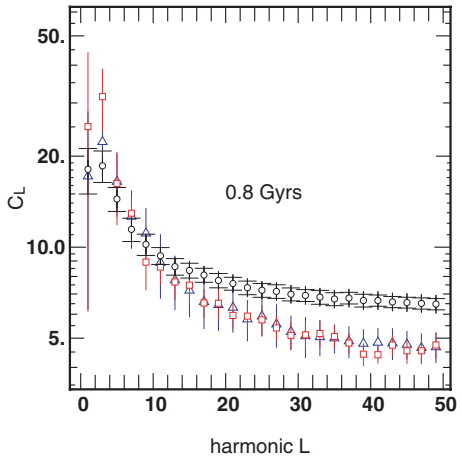

Figure 29. The average angular power spectrum, $\langle\langle C_\ell^{\varpi_\rho}\rangle\rangle(t)$, at $t = 0.8$ Gyr for three different mass resolutions in the simulations. $\langle\langle C_\ell^{\varpi_\rho}\rangle\rangle(t)$ is taken as the mode of the lognormal function used to fit the $C_\ell^{\varpi_\rho}$ distribution. For a given ℓ, the corresponding angular scale is π/ℓ. Circles stand for the measurements performed on the main set of simulations (50 Mpc h^{-1}, 128^3 particles), while error bars stand for 3σ errors. Square and triangles stand for measurements performed on simulation with higher mass resolution, respectively, 50 Mpc h^{-1} for 256^3 particles (1532 haloes analysed) and 20 Mpc h^{-1} for 256^3 particles (545 haloes analysed). In these two cases, error bars stand for 1σ errors.

angular structure of accretion was also investigated with two smaller sets of simulations: the first one involves 10 simulations with 256^3 particles in 50 Mpc h^{-1} boxes and the second in five simulations with the 256^3 particles in 20 Mpc h^{-1} boxes. The related $\langle\langle C_\ell^{\varpi_\rho}\rangle\rangle$ measured at a lookback time of 800 Myr are shown in Fig. 29. Here, 1532 and 545 haloes satisfying the conditions described in Section 4.2 were detected in these two additional sets of simulations. For clarity, 1σ error bars are shown for the two high-resolution measurements, while the 'larger statistics' power spectrum is still represented with 3σ bars. For large scales ($\ell < 10$), the three power spectra are consistent, thus suggesting that convergence was achieved there. On smaller scales, the two higher resolution spectra differ significantly from the one measured using the other set of simulations (50 Mpc/128^3 particles): high-ℓ holds significantly less power. This confirms that the lack of resolution tends to overestimate the importance of small scales and implies that the study of ϖ_ρ requires simulations at higher resolution in order to understand, e.g., the detailed statistics of small infalling objects. Interestingly, the two higher resolution simulations have identical $\langle\langle C_\ell^{\varpi_\rho}\rangle\rangle$, given the admittedly large error bars. This suggests that statistical convergence at scales $\ell < 50$ does not require extremely resolved simulations and simulation boxes with a mass resolution only 8–10 times greater than that used in this paper should suffice.

Finally, it clearly appears from Figs 27 and D2 that the angulo-temporal correlation function related to $\langle\langle C_\ell^{\varpi_\rho}\rangle\rangle(t)$ is dominated by the overall shift of the angular power spectrum towards higher values and consequently no coherence time should be detectable. It is shown in Appendix E that how the evolution of $\langle\langle C_\ell^{\varpi_\rho}\rangle\rangle(t)$ is related to mass biases and possible resolution effects. The previous measurements on the potential were not sensitive to these effects because of the smoother nature of the field.

In Appendix E, the measured secular evolution is avoided by using an alternative definition of $\langle\langle C_\ell^{\varpi_\rho}\rangle\rangle(t)$. It is found that the angular power spectrum of ϖ_ρ can be fitted by a simple power law (see Fig. E1) at every time:

$$\left\langle\left\langle C_\ell^{'\varpi_\rho}\right\rangle\right\rangle(t) \sim \ell^{-1.15}. \tag{77}$$

The corresponding angulo-temporal correlation function is given in Fig. E3. As expected, there is a shorter coherence time for the ϖ_ρ field than that for the potential, because of the 'sharper' nature of the former. Overall, these results strongly suggest that the class of mass and resolution biases should be systematically investigated beyond what was shown here.

7 A SCENARIO FOR THE ACCRETION OF A TYPICAL HALO AT $z \leqslant 1$

Let us draw a summary of the previous results, in order to get a synthetic picture of the flux properties at the virial radius. A typical halo in our sample has a mass of $10^{13}\,M_\odot$ and a radius $R_{200} \sim 500$ kpc at $z = 0$. It is embedded in a quasi-stationary gravitational potential, ψ^e. Such a potential is highly quadrupolar and is likely to be induced by the large-scale distribution of matter around the halo. The halo accretes material between $z = 1$ and 0 at a rate which declines with time. At high redshift, only accretion is detected at R_{200}. It is mainly radial and occurs at a velocity close to 75 per cent times the circular velocity. As time advances, accretion of new material decreases, while outflows become significant. Outflows occur at lower velocities and on more circular orbits. A fraction of the outflowing component is due to a backsplash population made of material which already passed through the virial sphere. Another fraction of outflows corresponds to 'virialized' material of the halo which goes further than R_{200} and is being 'cancelled' by its infalling counterpart. The clustering on the sphere of the gravitational potential drifts towards smaller scales, while the clustering of matter follows marginally the same trend at our level of resolution. It reflects the increasing contribution with time of weak/diffuse accretion, poorly sampled at our resolution. In parallel, the coherence time of potential fluctuations is found to be decreasing with time by the halocentric observer. This decrease may be related with the accretion of satellites, where objects were numerous enough to 'overlap' in the past,

which implies that accretion occurs mainly in the same direction on the virial sphere.

This scenario seems consistent with most of the past studies made on the subject using the full 3D information contained in simulations. The decline of accretion rate has been already measured by e.g. van den Bosch (2002a) even though our measurements are in a slight quantitative disagreement. The 'rebound' of matter through the virial sphere has already been measured by e.g. Mamon et al. (2004) or Gill et al. (2004). Furthermore, the velocity bimodality is recovered together with the circularization of orbits measured by Gill et al. (2004) in high-resolution simulations. Finally, the variation of the coherence time of the potential is found to be related to the anisotropy of accretion, already demonstrated by e.g. Aubert et al. (2004), Knebe et al. (2004) or Zentner et al. (2005).

8 SUMMARY AND DISCUSSION

This paper, the second in a series of three, presents measurements of the detailed statistical properties of dark matter flows on small scales ($\leqslant$ 500 kpc) in the near environment of haloes using a large set of ΛCDM cosmological simulations. The purpose of this investigation was two-fold: (i) characterize statistically (via one- and two-point statistics) the detailed (angular and kinematic) incoming fluxes of dark matter entering the virial sphere of a biased (described in Section 4.2) sample of haloes undergoing minor mergers for the broader interest of astronomers concerned with the environment of galaxies; (ii) compute the first two moments of the linear coefficients, c_n (respectively b_n), of the source term (respectively external potential) entering equations (13) and (14) (Paper I).

We concentrated on flows at the haloes' virial radius while describing the infalling matter via flux densities through a spherical shell. In parallel, we measured the statistical properties of the tidal potential reprojected back on to the boundary. The statistical one- and two-point expectations of the inflow were tabulated both kinematically and angularly on the R_{200} virtual sphere. All measurements were carried for 15 000 haloes undergoing minor (as defined) mergers between redshifts $z = 1$ and 0. The two-point correlations are carried both angularly and temporally for the flux densities and the tidal field. We also provided a method to regenerate realization of the field, via equations (37) and (F6).

We briefly demonstrated how a perturbative description of the dynamics of haloes could propagate the statistical properties of environments down to the statistical properties of the halo's response. The description of the environment involved the projection of the potential and the source on a basis of functions. This basis allowed us to decouple the time evolution from the angular and velocity dependence of these two quantities. Hence, the accretion and the tidal potential were completely described by the projection coefficients and their statistical properties, which depend on time only. We also discussed how the flux densities of matter, momentum and energy could be related to the source and its expansion coefficients. We restricted ourselves to the one- and two-statistical descriptions of the tidal field $\psi^{\rm e}$ and the flux density of mass ϖ_ρ and postponed to Paper III (Aubert & Pichon, in preparation), the full description of the higher moments. Since these measurements will be used as an entry to a perturbative description of the inner dynamics of haloes, only objects with quiet accretion history were selected as discussed in Section 4.2. Throughout this biased sample of haloes, we made statistical measurements of the kinematic properties of accretion and derived results on the following quantities.

(i) The evolution of the accretion rate at the virial sphere: the net accretion is found to decrease with time, probing both the increasing contribution of outflows and the decline of strong interactions.

(ii) The evolution of the net velocity distribution of the accretion: infall exhibits a typical velocity of $0.75V_{\rm c}$. A backsplash component is detected at recent times with a significant outflowing component at a lower velocity ($\sim 0.6V_{\rm c}$).

(iii) The evolution of the impact parameters/incidence angle distribution of the infall. The infall is found to be mainly radial while outflows are on more circular orbits.

(iv) The angulo-temporal two-point correlation of the external potential on virial sphere. The potential appears to be mainly dominated by a strong and constant quadrupole. The coherence time of smaller angular scales provides hints of an anisotropic accretion.

(v) The angular power spectrum of accreted matter. The clustering is dominated by small angular scales, possibly at the resolution limit.

(vi) The angulo-temporal correlation of the flux density of mass. The coherence time appears shorter than that for potential fluctuations, as expected.

These results can be interpreted in terms of properties of accreted objects or of smooth accretion and are coherent with previous studies (e.g. Ghigna et al. 1998; van den Bosch 2002a; Aubert et al. 2004; Gill et al. 2004; Knebe et al. 2004; Mamon et al. 2004; Benson 2005). These studies were mainly focused on to the properties of accreted satellites. Properties of accreted subhaloes could also be directly derived from these results, once a clear definition allows us to distinguish structures within the general flow of matter. Substructures are expected to form a distinct 'phase' of the accreted fluid: for instance, the velocity dispersion is expected to be quite different in compact objects than in the smooth accreting component. This phase separation will be assessed in Paper III where a systematic comparison of the current approach with an analysis in terms of pre-identified satellites will be carried, in the spirit of Aubert et al. (2004). The contribution of outflows, the lack of a standard definition for subhaloes, resolution issues and the fact that properties are measured at one radius (which could be statistically propagated towards inner regions) are all issues which must be assessed before a complete and rigorous comparison can be performed. Yet, the current agreement between a fluid description of the environment and these above mentioned published results is clearly encouraging hits for the reliability of the method presented here.

These kinematic signatures provide insights in the processes which occur in the inner regions of haloes. In particular, the kinematic discrepancies between the different components of the mass flux should be understood in terms of dynamical friction, tidal stripping or even satellite–satellite interactions within the halo. The kinematical properties of accreted matter may be transposed to the kinematical properties of satellites observed around galaxies. Newly accreted material exhibits kinematic signatures (radial, high-velocity trajectories) different from the ones measured for matter which already interacted with the halo (tangential, low-velocity orbits). Admittedly, it is not straightforward to apply directly these results to the luminous component (see Paper I, for a discussion of thresholding), and to see how projection effects may affect the distributions. Nevertheless, the corresponding observational measurements on satellites should provide information on the past history of these objects.

As discussed in Paper I, these measurements can be used as an entry to the perturbative theory of the response of the open halo. Phenomena related to accretion can be consistently assessed via

this framework: dynamical friction, tidal stripping and phase mixing. With the statistical description of the tidal field presented in this paper only, we may already implement the theory presented in Paper I in the regime of pure tidal excitation. The complete knowledge of the source (which will be completed in Paper III) should considerably extend the realm of application provided by this theory. Specifically, we have shown in Paper I that the internal dynamics of substructures within galactic haloes (distortion, clumps as traced by X-ray emissivity, weak lensing, dark matter annihilation, tidal streams, etc.) and the implication for the disc (spiral structure, warp, etc.) could be predicted within this framework. Conversely, the knowledge of the observed properties of a statistical sample of galactic haloes could be used to (i) constrain observationally the statistical nature of the infall (ii) predict the observed distribution and correlations of upcoming surveys, (iii) time reverse the observed distribution of clumps, and finally (iv) weight the relative importance of the intrinsic (via the unperturbed DF) and external (tidal and/or infall) influence of the environment in determining the fate of galaxies.

The current measurements reduce the degree of freedom that still exists in the setting of numerical experiments in a galactic context. For instance, given that the structure of the external tidal field is found to be simple, it can easily be modelled as an external component in numerical simulations (or even in analytical studies). It would provide a simple but statistically relevant contribution of the large-scale structure to the dynamical states of haloes. The temporal coherence of the first $\ell > 2$ angular harmonics of the tidal field should allow one to draw more accurate representations of external contribution to the field that would include the fluctuations due to smaller structures. The kinematics of accretion is not random as well and the distribution of velocities at R_{200} follows a Gaussian-shaped curve which characteristics evolve with time and exhibit a certain distribution of the impact parameter. These results put prescriptions that could be used to generate encounters between satellites and galactic discs that follow the ones measured in cosmological simulations at large radii. We also presented first constrains on the angulo-temporal correlation function of the accretion. Even though it is not completely clear yet how resolution will eventually affect these results, such functions contain some glimpses of information regarding the angular distribution of encounters with external systems but also regarding the frequency of accretion events. This frequency can also be probed by the temporal coherence of the fluctuations in the tidal field. The apparent contradiction that exists between the observed number of discs and the predicted large number of mergers may be solved by a better knowledge of the frequency of the latter: it may be low enough to solve this contradiction. In this context, simulations of successive mergers between a galaxy and satellites should be consistent with large-scale simulations and we provide first constrains on the rate of minor encounters at the outer boundary of the halo.

As argued in Paper I, we emphasize that an a priori discrimination between 'objects' and diffuse matter may not constitute the best way to describe accretion: it is not clear that luminous matter is always attached to dark matter overdensities, there is no unambiguous definition of substructures and their state change with time under the influence of tidal shocks or dynamical friction. The generation of objects that follow the current results is admittedly the easiest way to proceed but should be followed by a more general description of matter in terms of 'fluid approach', where 'objects' only constitute a specific phase of such a fluid. The statistical measurements on both $\psi^{\rm e}$ and ϖ_ρ allow the regeneration of synthetic environments. Knowing the average evolution and the angular power spectra of these quantities, the generation of spherical maps in the Gaussian regime is straightforward. We describe such a regeneration procedure in Appendix F. Such maps would efficiently provide realistic environments of haloes, consistent (up to two-point statistics) with those measured in cosmological simulations and could be 'embedded' into simulation of galaxies. Again, virialized structures would be naturally included (since they have their own statistical signature on the virial sphere) without relying on any ad hoc prescription on their nature.

Extensions to non-Gaussian fields are also possible (following e.g. Contaldi & Magueijo 2001) but would rely on higher order correlations. It was assumed throughout these investigations that fields could be approximated as Gaussian fields, fully described by their two-point statistics. Yet a simple visual inspection of ϖ_ρ maps reveals that they are not strictly Gaussian, a finding confirmed by preliminary analysis of their bispectrum. Furthermore, Paper I demonstrated that a dynamical description which takes into account non-linear effects, such as dynamical friction, requires higher order correlations. Therefore, extensions to non-Gaussian fields are in order in the long run.

It should again be emphasized that some aspects of the present work are exploratory only, in that the resolution achieved ($M_{\rm halo} > 5 \times 10^{12}\,{\rm M}_\odot$) is somewhat high for $L_\star$ galaxies. In fact, it will be interesting to confirm that the properties of infall do not asymptote for lower mass ($M_{\rm halo} < 5 \times 10^{12}\,{\rm M}_\odot$) together with the intrinsic properties of galaxies. In addition, a systematic study of biases induced by our estimators of angular correlations should be conducted. For a fixed halo mass, our lack of resolution implies that we overestimate the clumsiness of the infall.

As demonstrated in Section 6.2.2, the limited resolution (both spatially and in mass) of our simulations appeared to be an issue for some of the results presented here (e.g. the angular power spectrum of ϖ_ρ). The systematic use of higher resolution simulations (in the spirit of Section 6) will be required to fully assess these limitations. In particular, a fraction of the accretion detected as a weak/diffuse component may be associated with unresolved objects; the influence of small-mass satellites should therefore be explored. With the prospect of deducing the properties of galaxy from haloes environments, lower mass haloes are more likely to host only one galaxy, making them more suitable for such a study. Cosmological simulation of small volumes also tends to prevent the formation of rare events which may be relevant for the representativity of the study: for example, some discs seem to indicate that they were formed in 'very quiet' environments. The right balance between resolution and volume should be found. Aside from these biases induced by simulations, we also introduced selection criteria on both the mass or the accretion history of haloes and the influence of these arbitrary choices on our statistical distribution should be assessed precisely.

Eventually using hydrodynamical codes which include baryonic effects in simulations and introducing the physics of gas in our model, we would construct a complete semi-analytic tool to study the detailed inner dynamics of galaxies.

ACKNOWLEDGMENTS

We are grateful to S. Colombi and J. Devriendt for useful comments and helpful suggestions. We would like to thank D. Munro for freely distributing his YORICK programming language (available at ftp://ftp-icf.llnl.gov:/pub/Yorick), together with its MPI interface, which we used to implement our algorithm in parallel. DA thanks the Institute of Astronomy for its hospitality and funding from a Marie Curie studentship. We acknowledge support from the

Observatoire de Strasbourg computer facility and the *HORIZON* project (http://www.projet-horizon.fr). Finally, we would like to thank the anonymous referee for useful remarks on the manuscript.

REFERENCES

Abadi M. G., Navarro J. F., Steinmetz M., Eke V. R., 2003, ApJ, 597, 21
Appel W., 2002, Mathematiques Pour la Physique et les Physiciens. H&K Editions, Paris
Aubert D., Pichon C., Colombi S., 2004, MNRAS, 352, 376
Bardeen J. M., Bond J. R., Kaiser N., Szalay A. S., 1986, ApJ, 304, 15
Benson A. J., 2005, MNRAS, 358, 551
Benson A. J., Frenk C. S., Baugh C. M., Cole S., Lacey C. G., 2001, MNRAS, 327, 1041
Bernardeau F., Colombi S., Gaztañaga E., Scoccimarro R., 2002, Phys. Rep., 367, 1
Bertschinger E., 2001, ApJS, 137, 1
Binney J., Jiang I., Dutta S., 1998, MNRAS, 297, 1237
Blaizot J. et al., 2006, MNRAS, 369, 1009
Bond J. R., Cole S., Efstathiou G., Kaiser N., 1991, ApJ, 379, 440
Cole S., Aragon-Salamanca A., Frenk C. S., Navarro J. F., Zepf S. E., 1994, MNRAS, 271, 781
Colpi M., Mayer L., Governato F., 1999, ApJ, 525, 720
Contaldi C. R., Magueijo J., 2001, Phys. Rev. D, 63, 103512
Eisenstein D. J., Hut P., 1998, ApJ, 498, 137
Flores R. A., Primack J. R., 1994, ApJ, 427, L1
Ghigna S., Moore B., Governato F., Lake G., Quinn T., Stadel J., 1998, MNRAS, 300, 146
Gill S. P. D., Knebe A., Gibson B. K., Dopita M. A., 2004, MNRAS, 351, 410
Hashimoto Y., Funato Y., Makino J., 2003, ApJ, 582, 196
Hunter C., Toomre A., 1969, ApJ, 155, 747
Ibata R. A., Gilmore G., Irwin M. J., 1995, MNRAS, 277, 781
Jiang I., Binney J., 1999, MNRAS, 303, L7
Kalnajs A. J., 1977, ApJ, 212, 637
Kauffmann G., White S. D. M., 1993, MNRAS, 261, 921
Kauffmann G., Colberg J. M., Diaferio A., White S. D. M., 1999, MNRAS, 303, 188
Klypin A., Kravtsov A. V., Valenzuela O., Prada F., 1999, ApJ, 522, 82
Knebe A., Gill S. P. D., Gibson B. K., Lewis G. F., Ibata R. A., Dopita M. A., 2004, ApJ, 603, 7
Lacey C., Cole S., 1993, MNRAS, 262, 627
Lynden-Bell D., Kalnajs A. J., 1972, MNRAS, 157, 1
Mamon G. A., Sanchis T., Salvador-Solé E., Solanes J. M., 2004, A&A, 414, 445
McConnachie A. W., Irwin M. J., Ibata R. A., Ferguson A. M. N., Lewis G. F., Tanvir N., 2003, MNRAS, 343, 1335
Moore B., 1994, Nat, 370, 629
Moore B., Ghigna S., Governato F., Lake G., Quinn T., Stadel J., Tozzi P., 1999, ApJ, 524, L19
Murali C., 1999, ApJ, 519, 580
Murali C., Tremaine S., 1998, MNRAS, 296, 749
Navarro J. F., Steinmetz M., 1997, ApJ, 478, 13
Ostriker E. C., Binney J. J., 1989, MNRAS, 237, 785
Peacock J. A., 1999, Cosmological Physics. Cambridge Univ. Press, Cambridge
Peebles P. J. E., 1980, The Large-Scale Structure of the Universe. Princeton Univ. Press, Princeton, NJ, p. 435
Pichon C., Aubert D., 2006, MNRAS, 368, 1657 (Paper I)
Quinn P. J., Hernquist L., Fullagar D. P., 1993, ApJ, 403, 74
Reshetnikov V., Combes F., 1998, A&A, 337, 9
Roukema B. F., Quinn P. J., Peterson B. A., Rocca-Volmerange B., 1997, MNRAS, 292, 835
Somerville R. S., Kolatt T. S., 1999, MNRAS, 305, 1
Sparke L. S., Casertano S., 1988, MNRAS, 234, 873
Springel V., Yoshida N., White S. D. M., 2001, New. Astron., 6, 79
Toomre A., Toomre J., 1972, ApJ, 178, 623
Tormen G., 1997, MNRAS, 290, 411
Tremaine S., Weinberg M. D., 1984, MNRAS, 209, 729
Tsuchiya T., 2002, New. Astron., 7, 293
van den Bosch F. C., 2002a, MNRAS, 331, 98
van den Bosch F. C., 2002b, MNRAS, 332, 456
van Haarlem M., van de Weygaert R., 1993, ApJ, 418, 544
Velazquez H., White S. D. M., 1999, MNRAS, 304, 254
Walker I. R., Mihos J. C., Hernquist L., 1996, ApJ, 460, 121
Wechsler R. H., Bullock J. S., Primack J. R., Kravtsov A. V., Dekel A., 2002, ApJ, 568, 52
Weinberg M. D., 1998, MNRAS, 299, 499
Weinberg M. D., 2001, MNRAS, 328, 321
Zentner A. R., Kravtsov A. V., Gnedin O. Y., Klypin A. A., 2005, ApJ, 629, 219

APPENDIX A: HARMONIC CONVERGENCE

As explained in Section 3.1, the angular dependence of the source function is expanded over a basis of spherical harmonics $Y_{\ell m}(\mathbf{\Omega})$. In order to set the maximal order of this expansion, $\ell_{\max}$, we compared the two-point correlation function of the spherical field $\rho v_{\rm r}(\mathbf{\Omega})$ to the one inferred from harmonic coefficients, $a_{\ell m}$, and power spectrum C_ℓ (see equations 41 and 42). Within a set of randomly distributed particles, let $d_{\rm poisson}(\theta)$ be the probability of finding two particles with an angular separation θ. If $d(\theta)$ is the same probability for a given distribution of particles then its two-point correlation function $\xi(\theta)$ is defined as

$$\xi(\theta) \equiv \frac{d(\theta)}{d_{\rm poisson}(\theta)} - 1. \tag{A1}$$

The correlation function $\xi(\theta)$ and the $a_{\ell m}$ coefficients are related by (e.g. Peacock 1999)

$$\xi(\theta) = \sum_{\ell=0}^{\ell_{\max}} C_\ell (2\ell+1) P_\ell(\cos\theta), \tag{A2}$$

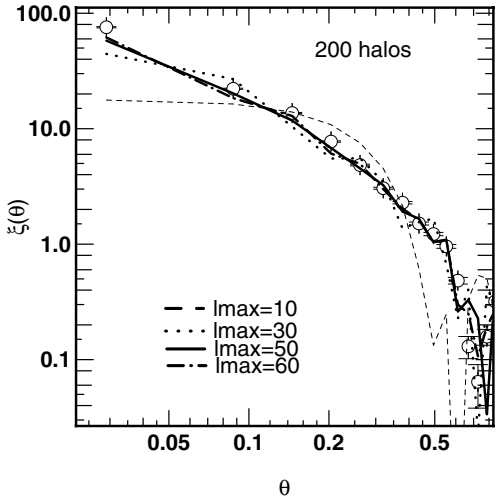

Figure A1. The average angular two-point correlation function, $\langle\!\langle \xi(\theta) \rangle\!\rangle$, of the advected mass spherical field $\rho v_{\rm r}(\mathbf{\Omega})$. The correlation function is shown as a function of the angular distance on the sphere θ given in radians. Using the positions of accreted particles around 200 haloes at $z = 1$, the average correlation function can be computed (*dots*). Lines represent the correlation function deduced from the harmonic coefficients of the $\rho v_{\rm r}(\mathbf{\Omega})$ fields around the same 200 haloes, with $\ell_{\max} = 10, 30, 50, 60$. The convergence is ensured for $\ell_{\max} \geqslant 50$.

where θ is an angular distance of the sphere and $P_\ell(x)$ is a Legendre function. The average angular correlation function $\langle\langle\xi(\theta)\rangle\rangle_{\rm pair}$ is defined as

$$\langle\langle\xi(\theta)\rangle\rangle_{\rm pair} \equiv \frac{1}{\sum_p n_p^2}\sum_p n_p^2 \xi_p(\theta), \tag{A3}$$

where $\xi_p(\theta)$ is the two-point correlation function of the pth halo computed using n_p particles passing through the virial sphere. From a set of 200 haloes extracted from a simulation, we computed $\langle\langle\xi(\theta)\rangle\rangle$ using different values for $\ell_{\rm max}$ (see Fig. A1). From the same set of haloes, we also computed the average two-point correlation function directly from the particles' positions using equation (A1).

From Fig. A1, it clearly appears that $\langle\langle\xi(\theta)\rangle\rangle_{\rm pair}$ has not converged for $\ell_{\rm max} \leqslant 30$. For $\ell_{\rm max} \geqslant 50$, the actual two-point correlation function is well reproduced. Since no real difference can be distinguished between $\ell_{\rm max} = 50$ and 60, we chose to limit the harmonic expansion of the source term to $\ell \leqslant 50$. Note that the truncation in $\ell_{\rm max}$ defines an effective resolution beyond which the distribution is effectively coarse grained.

APPENDIX B: ANGULO-TEMPORAL CORRELATION

Let us consider a spherical field $X(\mathbf{\Omega}, t)$ which can be expanded over the spherical harmonic basis

$$X(\mathbf{\Omega}, t) = \sum_{\ell m} x_{\ell m}(t) Y_{\ell m}(\mathbf{\Omega}). \tag{B1}$$

The correlation w^X between two successive realizations of X is defined as

$$w^X(\mathbf{\Omega}, \mathbf{\Omega}', t, t') \equiv \langle X(\mathbf{\Omega}, t) X(\mathbf{\Omega}', t')\rangle, \tag{B2}$$

where $\langle\cdot\rangle$ stands for the statistical average. If $X(\mathbf{\Omega}, t)$ is *isotropic*, the correlation should not depend on $\mathbf{\Omega}$ or $\mathbf{\Omega}'$ but only on the distance θ between the two points. It implies that w^X can be expanded on the basis of Legendre polynomials, $P_{\rm L}(y)$,

$$w^X(\mathbf{\Omega}, \mathbf{\Omega}', t, t') = w^X(\theta, t, t') = \sum_{\rm L}(2L+1) T_{\rm L} P_{\rm L}[\cos(\theta)]. \tag{B3}$$

How are $T_{\rm L}$ and $x_{\ell m}$ related? Rewriting equation (B2) as

$$w^X(\theta, t, t') = \sum_{\ell m}\sum_{\ell' m'} \langle x_{\ell m}(t) x^*_{\ell' m'}(t')\rangle Y_{\ell m}(\mathbf{\Omega}) Y^*_{\ell' m'}(\mathbf{\Omega}'), \tag{B4}$$

one can write

$$\int {\rm d}\mathbf{\Omega}{\rm d}\mathbf{\Omega}' Y^*_{\ell_1 m_1}(\mathbf{\Omega}) Y_{\ell_2 m_2}(\mathbf{\Omega}') w^X = \left\langle x_{\ell_1 m_1}(t) x^*_{\ell_2 m_2}(t')\right\rangle. \tag{B5}$$

Meanwhile, assuming isotropy, one can also write

$$\begin{aligned}
&\int {\rm d}\mathbf{\Omega}{\rm d}\mathbf{\Omega}' Y^*_{\ell_1 m_1}(\mathbf{\Omega}) Y_{\ell_2 m_2}(\mathbf{\Omega}') w^X \\
&\quad = \sum_{\rm L}(2L+1) T_{\rm L} \int {\rm d}\mathbf{\Omega}{\rm d}\mathbf{\Omega}' Y^*_{\ell_1 m_1}(\mathbf{\Omega}) Y_{\ell_2 m_2}(\mathbf{\Omega}') P_{\rm L}[\cos(\theta)] \\
&\quad = \sum_{\rm LM}(4\pi) T_{\rm L} \int {\rm d}\mathbf{\Omega}{\rm d}\mathbf{\Omega}' Y^*_{\ell_1 m_1}(\mathbf{\Omega}) Y_{\ell_2 m_2}(\mathbf{\Omega}') Y_{\rm LM}(\mathbf{\Omega}) Y^*_{\rm LM}(\mathbf{\Omega}') \\
&\quad = \sum_{\rm LM}(4\pi) T_{\rm L} \delta_{{\rm L}\ell_1}\delta_{{\rm L}\ell_2}\delta_{Mm_1}\delta_{Mm_2},
\end{aligned} \tag{B6}$$

where $P_{\rm L}$ is expressed in terms of spherical harmonics using the spherical harmonics addition theorem. In the end, we get

$$T_\ell = \frac{1}{4\pi}\left\langle x_{\ell m}(t) x^*_{\ell m}(t')\right\rangle. \tag{B7}$$

For a given realization of $X(\mathbf{\Omega}, t)$, T_ℓ can be estimated by

$$T_\ell = \frac{1}{4\pi}\frac{1}{2\ell+1}\sum_m x_{\ell m}(t) x^*_{\ell m}(t'). \tag{B8}$$

APPENDIX C: DISTRIBUTIONS

In this appendix, we present the various distributions fitted either by normal or by lognormal PDF. For each quantity, the mode (or most probable value) of the distribution has been obtained from these fits. The Gaussian distribution is defined by

$$\mathrm{N}(x) = \frac{A}{\sigma\sqrt{2\pi}}\exp\left[-\frac{(x-\mu)^2}{2\sigma^2}\right], \tag{C1}$$

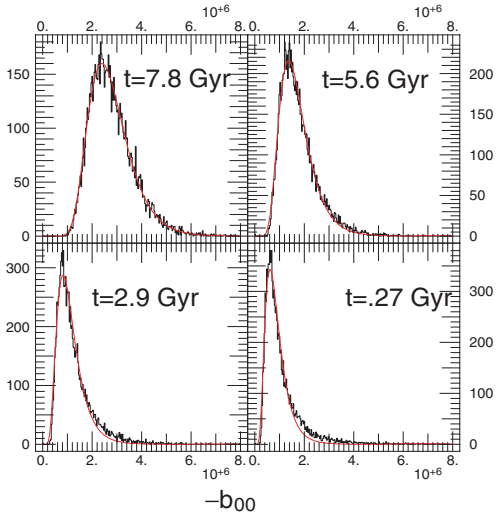

Figure C1. The probability distribution of b_{00} at four different times. This coefficient is proportional to the external potential averaged on the sphere. The lognormal fit is also shown.

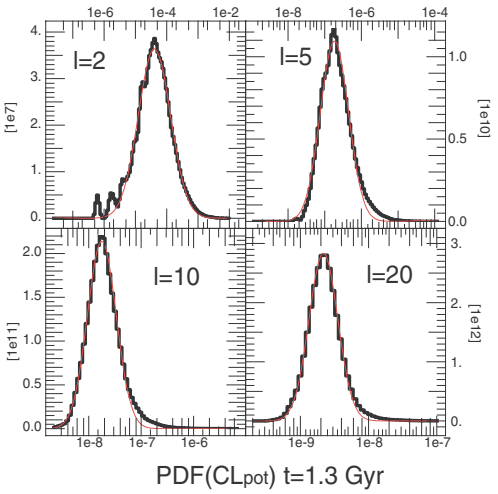

Figure C2. The probability distribution of $C_\ell^{\psi^{\rm e}}$ for $\ell = 2$, 5, 10, 20 at the lookback time $t = 1.9$ Gyr. Note that x-axis is sampled logarithmically; the corresponding lognormal fit of the mode is also shown.

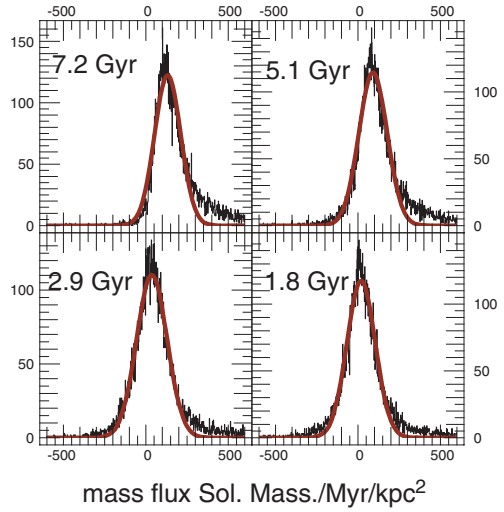

Figure C3. The probability distribution of the mean flux $\Phi^{\rm M}$ (t) for four different times. The normal fit is also shown.

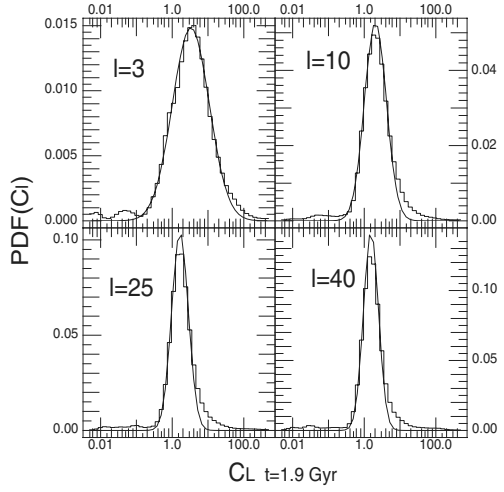

Figure C4. The probability distribution of the C_ℓ for $\ell = 3$, 10, 25, 40 at the lookback time $t = 1.9$ Gyr. Note that x-axis is sampled logarithmically; the corresponding lognormal fit of the mode is also shown.

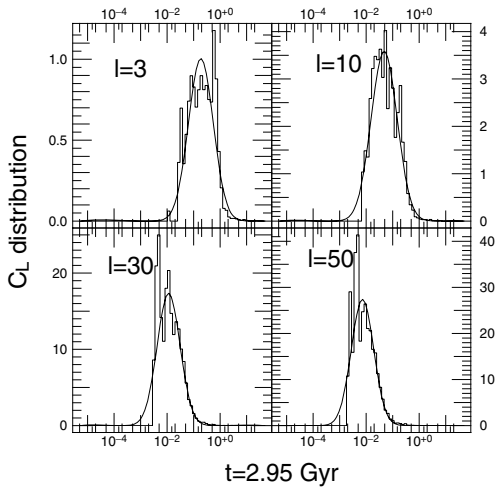

Figure C5. The probability distribution of $C_\ell^{\varpi_{\rho'}}$ for $\ell = 3$, 10, 25, 40 at the lookback time $t = 1.9$ Gyr. Note that x-axis is sampled logarithmically; the corresponding lognormal fit of the mode is also shown.

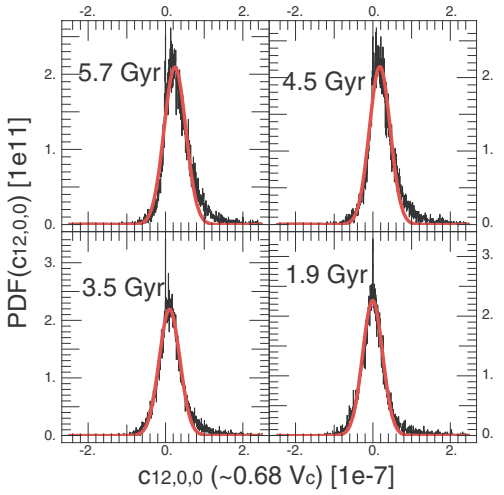

Figure C6. The probability distribution of the $c^{0,0}_{12,0,0}$ for the lookback times $t = 1.9$, 3.5, 4.5 and 5.7 Gyr. Note that x-axis is sampled linearly; the corresponding fit of the mode is also shown.

while the mode is equivalent to the mean μ. The lognormal distribution is given by

$$\mathrm{LN}(x) = \frac{A}{\sigma\sqrt{2\pi}} \exp\left\{-\frac{[\log(x/\mu)]^2}{2\sigma^2}\right\}, \tag{C2}$$

while the mode is given by $\mu \exp(-\sigma^2)$. The different fits mentioned in the main text are described in the following figures.

(i) Fig. C1 shows the distributions of the harmonic coefficient $b_{00}(t)$ which is proportional to the potential averaged on the sphere. It is expressed in units of GM/R, where M is expressed in $10^{10}\,\mathrm{M}_\odot$, R in kpc h^{-1} and $G = 43\,007$ in internal units.

(ii) Fig. C2 shows the distributions of the external potential's power spectrum for four different harmonics $\ell = 2$, 5, 10, 20 at $t =$ 1.3 Gyr. The distribution has been fitted by a lognormal function.

(iii) Fig. C3 shows the distributions of the mean flux $\Phi^{\rm M}(t)$. The mean flux is proportional to the harmonic coefficient a_{00}. The distribution is fitted by a normal distribution. The normal model agrees well with the measured distribution at recent times but fails to reproduce the outliers' tail at high redshift. Consequently, the mode position is underestimated at these times.

(iv) Fig. C6 shows the distributions of one of the coefficients involved in the computation of the velocity distribution $\phi(v)$. Four different times are being represented. The coefficient distribution has been fitted by a Gaussian distribution.

(v) Fig. C4 shows the distributions of the power spectrum values $C_\ell^{\varpi_\rho}$ for four different harmonic orders, ℓ. The fits were made at $t =$ 1.9 Gyr. This distribution has been fitted by a lognormal distribution.

(vi) Fig. C5 shows the distributions of the power spectrum values $C_\ell^{\varpi_{\rho'}}$ for four different harmonic orders, ℓ. The fits were made at $t = 2.95$ Gyr. This distribution has been fitted by a lognormal distribution.

APPENDIX D: FITS AND TABLES

In the main text, some statistics are fitted by simple laws and the time evolution of these statistics can be described by the time evolution of

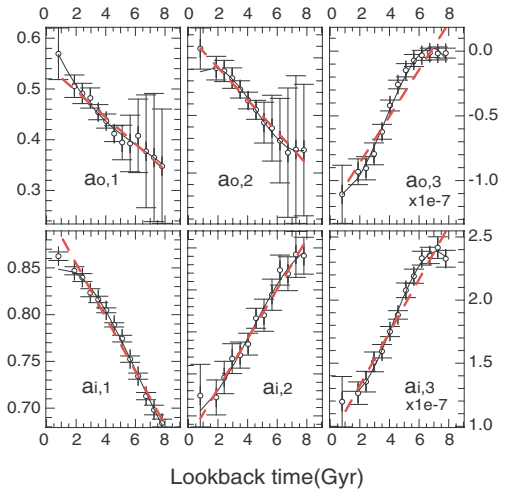

Figure D1. Time evolution of the fitted coefficients (given in Table D1) of the PDF $\langle\varphi(v,t)\rangle$ for the parametrization suggested in equation (60) (*symbols*). Bars stand for the 3σ errors on the determination of the coefficients. $q_{\imath,k}$, $k=1,2,3$, are, respectively, the mean, the rms and the amplitude of the positive Gaussian (i.e. infalling component). $q_{o,k}$, $k=1,2,3$ are the corresponding values for the negative Gaussian (i.e. outflowing component). The trend is accurately fitted by a linear relation (red dashed line).

Table D1. Fitting parameters for the time evolution of Gaussian coefficients, $q(t)=m\times t\,(\mathrm{Gyr})+n$. These coefficients, together with equation (60), allow us to compute the time evolution of $\langle\varphi(v,t)\rangle$. (*) By definition, $q_{o,3}\leqslant 0$.

	m	n
$q_{\imath,1}$	-0.028	0.912
$q_{\imath,2}$	0.0059	0.084
$q_{\imath,3}$	2.1×10^{-8}	9.03×10^{-8}
$q_{o,1}$	-0.026	0.54
$q_{o,2}$	-0.028	0.23
$q^{(*)}_{o,3}$	1.79×10^{-8}	-1.22×10^{-7}

Table D2. Fitting parameters for the time evolution of $p_k(t)$, $k=1,2,3$ parameters. $p(t)=m\times t\,(\mathrm{Gyr})+n$. Together with equation (64), these coefficients allow us to predict the time evolution of $\langle\vartheta(\Gamma_1,t)\rangle$.

	m	n
p_1	-0.038	0.83
p_2	-3.12×10^{-8}	2.29×10^{-7}
p_3	8.59×10^{-8}	-6.64×10^{-7}

the fitting parameters. In this appendix, we present the time evolution of these parameters.

(i) Fig. D1 and Table D1 present the time evolution of the velocity distribution of accretion. It can be fitted by two Gaussians drifting towards higher velocities with time.

(ii) Table D2 summarizes the time evolution of the distribution of incidence angles. This distribution can be fitted by a Gaussian (for the inflows) and a linear relation (for the outflows). The fitting parameters present a linear evolution with time.

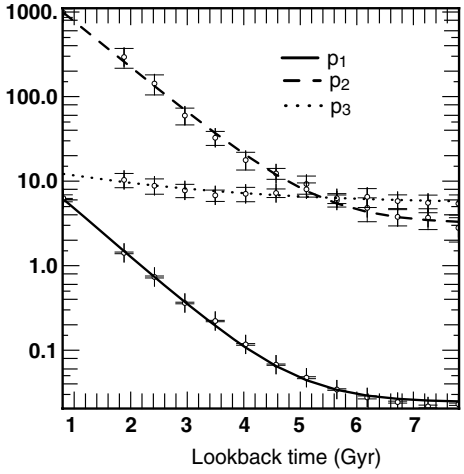

Figure D2. Time evolution of the coefficients for the $\langle\!\langle C_\ell^{\varpi_\rho}\rangle\!\rangle(t)$ model (see equation 75) (*symbols*). The three time evolutions may be described accurately by decreasing exponentials (see equation 76) (solid lines).

Table D3. Fitting parameters for the time evolution of $\langle\!\langle C_\ell\rangle\!\rangle^{\varpi_\rho}$ model's coefficients (see equation 75). $q_3^{\varpi_\rho}(t)=h+k\mathrm{e}^{-\frac{t}{u^2}}$ with lookback time t expressed in Gyr.

	h	k	u
$q_1^{\varpi_\rho}$	0.0242	17.86	0.867
$q_2^{\varpi_\rho}$	3.153	2699.0	0.8933
$q_3^{\varpi_\rho}$	5.4105	9.44	1.55

(iii) Fig. D2 and Table D3 summarize the time evolution of the angular power spectrum of ϖ_ρ. The power spectrum can be fitted by equation (75), where fitting parameters decrease exponentially with time.

APPENDIX E: ALTERNATIVE CONTRAST AND ANGULO-TEMPORAL CORRELATION

It appears clearly from the time evolution of $\langle\!\langle C_\ell^{\varpi_\rho}\rangle\!\rangle(t)$ presented in the main text, that no angulo-temporal correlation can be computed, since it would be completely dominated by the secular evolution of the power spectrum. For this reason, an alternative definition of the flux density contrast has been used

$$\delta'_{[\varpi_\rho]}(\mathbf{\Omega})\equiv\frac{\varpi_\rho(\mathbf{\Omega})-\overline{\varpi_\rho}}{\overline{\varpi_\rho}}=\sum_{\ell,m}\tilde{a}'_{\ell,m}Y_{\ell,m}(\mathbf{\Omega}),\tag{E1}$$

or in terms of harmonic coefficients

$$\tilde{a}'_{\ell,m}\equiv\sqrt{4\pi}\left(\frac{a_{\ell,m}}{a_{00}}-\delta_{\ell0}\right).\tag{E2}$$

Using this new definition, the fluctuations of ϖ_ρ on the sphere are measured relative to the mass flux of each individual halo. The main drawback of such a definition is that it couples the a_{00} and the $a_{\ell m}$ coefficients from the beginning. For example, the resimulation of such fields would require the knowledge of conditional probabilities, i.e. what is the distribution of $a_{\ell m}$ for a given value of a_{00}, while the previous definition (given by equation 73) only acted as specific choice of (non-constant) units. Furthermore, this new definition is more sensitive to outliers with low a_{00} values.

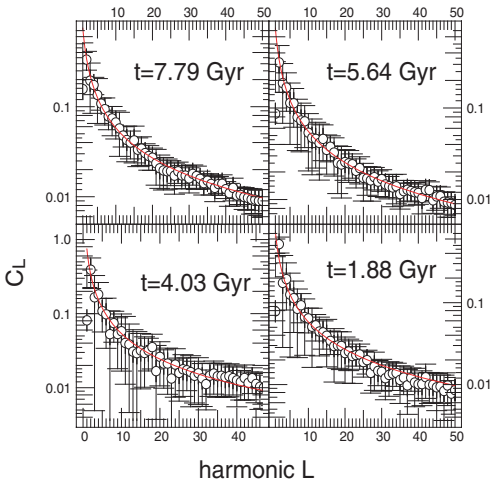

Figure E1. The angular power spectrum of the external potential, $\langle\langle C'^{\varpi_\rho}_\ell \rangle\rangle(t)$, at four different lookback times (symbols). Harmonics coefficients were normalized using equation (E2), halo by halo. $\langle\langle C'^{\varpi_\rho}_\ell \rangle\rangle(t)$ is taken as the mode of the lognormal function used to fit the $C'^{\varpi_\rho}_\ell$ distribution. Bars stand for 3σ errors. For a given ℓ, the corresponding angular scale is π/ℓ. The power spectra maybe fitted by a generic model given by equation (E3) (solid line). Unlike $\langle\langle C'^{\varpi_\rho}_\ell \rangle\rangle(t)$, $\langle\langle C'^{\varpi_\rho}_\ell \rangle\rangle(t)$ remains the same with time because of a different normalization.

Still, the angular power spectrum $\langle\langle C'^{\varpi_\rho}_\ell \rangle\rangle(t)$ of $\delta'_{[\varpi_\rho]}(\mathbf{\Omega})$ is much more regular than the one obtained from the previous definition. Its overall amplitude remains constant over the last 8 Gyr, while its shape seems to be less dominated by small-scale contributions. This alternative power spectrum is well fitted by a single power law

$$\langle\langle C'^{\varpi_\rho}_\ell \rangle\rangle(t) = 0.75\ell^{-1.15}, \tag{E3}$$

for the whole time range covered by the current measurements. This constant shape suggests that harmonic coefficients scale like a_{00}, i.e. the mass flux. Such a scaling is not obvious, since a strongly clustered ϖ_ρ field may coexist with a nil net flux (i.e. $a_{00} \sim 0$). It also implies that the evolution measured on the previous definition of the power spectrum, $\langle\langle C^{\varpi_\rho}_\ell \rangle\rangle(t)$, is more related to the evolution of the average flux (traced by a_{00}) than to the modification of the fluctuations amplitude (traced by the others $a_{\ell m}$). Still, the evolution of $\langle a_{00} \rangle$ spans over one magnitude, while the evolution of $\langle\langle C^{\varpi_\rho}_\ell \rangle\rangle(t)$ spans over several order of magnitudes: this strongly suggests that two different populations of haloes contribute to the two types of power spectrum. In Fig. E2, the scatter plot of C_{40} and C'_{40} as a function of a_{00} shows that the haloes which experience strong accretion dominate the peak of the C'_{40} distribution, while haloes with low accretion dominate the peak of the C_{40}. Furthermore, C_{40} does not scale anymore like a_{00} as it drops below some level, providing hints of resolution and isolated particles' effects. To conclude, $\delta'_{[\varpi_\rho]}(\mathbf{\Omega})$ appears as better way to rescale the fluctuations' amplitude since it provides a more regular behaviour of the power spectrum, but it is a more complex quantity to manipulate. Meanwhile, $\delta_{[\varpi_\rho]}(\mathbf{\Omega})$ is probably the correct way to proceed but is clearly more sensitive to resolution effects, which should be assessed with bigger simulations in the future.

Since the behaviour of $\delta'_{[\varpi_\rho]}(\mathbf{\Omega})$ is more regular than the previous contrast definition, the angulo-temporal correlation function of the flux density of mass has been computed from this new definition. Since this definition is different from that used for the potential, we restrict ourselves to a qualitative description. The correlations are

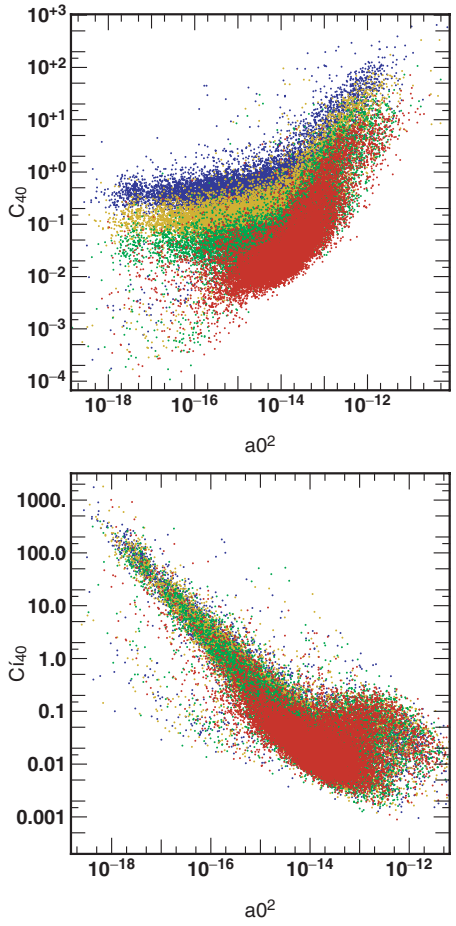

Figure E2. Scatter plots of the power spectra $C^{\varpi_\rho}_{40}$ (top) and $C'^{\varpi_\rho}_{40}$ (bottom) as a function of a^2_{00}. The four colours stand for different lookback times: $t = 7.8$ (red), 5.6 (green), 4.0 (yellow) and 2.8 Gyr (blue). The monopole a_{00} scales like the integrated flux of matter. The quantities $C^{\varpi_\rho}_{40}$ and $C'^{\varpi_\rho}_{40}$ differ by the normalization applied to the harmonic coefficients $a_{\ell m}$. See the main text for more details.

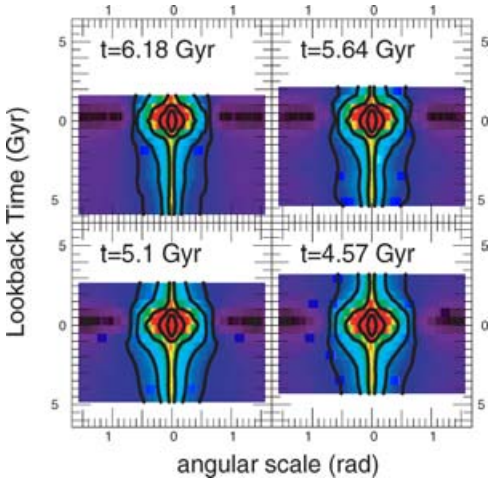

Figure E3. The angulo-temporal correlation function, $w'^{\varpi}(\theta, \Delta t) = \langle \delta_{[\varpi]}(\mathbf{\Omega}, t)\delta_{[\varpi]}(\mathbf{\Omega} + \Delta\mathbf{\Omega}, t + \Delta t)\rangle$. Blue (respectively red) colours stand for low (respectively high) values of the correlation. Isocontours are also shown. Large angular scale isocontours ($\Delta\mathbf{\Omega} \sim \pi/2$) have large temporal extent, due to the quadrupole dominance over the potential seen in the virial sphere.

given in Fig. E3. Clearly, the correlation is more peaked around $\Delta t = 0$ and more generally w^{ϖ_ρ} is sharper than w^{ψ}. Note that no multipole ℓ has been removed during the computation of w^{ϖ_ρ}, implying that the quadrupole effect measured in the potential correlation is simply not detected for this field. This strongly suggests a large-scale 'cosmic' origin for the quadrupolar tidal field rather than an artefact of the spherical intersection of an ellipse. Furthermore, the correlation time is smaller than the one measured for the potential, even compared to the correlation time of the potential without the $\ell = 2$ component. This is coherent with the fact that density blobs should be 'sharper' than potential blobs as they pass through the sphere.

APPENDIX F: REGENERATING GALACTIC TIME LINES

Given the measurements in Sections 5 and 6, let us describe here how to regenerate realizations of the history of the environment of haloes, first for the tidal field only, and then for the full accretion history.

F1 Regenerating tidal fields

Let us first focus on the generation of the potential tidal field generated by fly bys, hence neglecting the influence of the infall through the virial sphere.[5]

First, we consider two time variables: T (the 'slow time') which describes the secular evolution of the field and $t_{\rm f}$ (the 'fast time') which describes the temporal evolution around a given value of T, hence describing high-frequency variations. We assume that correlations exist only on small time-scales, while variations on the 'slow time' scale describe secular drifts. Therefore, the field's regeneration should include both correlations on short time-scales and long-term evolution.

Let us call $\hat{\mathbf{\Psi}} = \hat{\psi}_{\boldsymbol{m},\omega}(T)$ the temporal (with respect to the fast time) and angular Fourier transforms of the potential, at fixed slow time, T. The probability distribution of $\hat{\mathbf{\Psi}}$, $p(\hat{\mathbf{\Psi}})$ is given by

$$p(\hat{\mathbf{\Psi}}) = \frac{\exp\left[-\frac{1}{2}(\hat{\mathbf{\Psi}} - \langle\hat{\mathbf{\Psi}}\rangle)^{\top}\cdot\boldsymbol{C}_{\hat{\Psi}}^{-1}\cdot(\hat{\mathbf{\Psi}} - \langle\hat{\mathbf{\Psi}}\rangle)\right]}{(2\pi)^{1/2}\det{}^{1/2}|\boldsymbol{C}_{\hat{\Psi}}|}, \tag{F1}$$

where the variance reads

$$\boldsymbol{C}_{\Psi}(T) = \langle(\hat{\Psi}_{\boldsymbol{m},\omega} - \langle\hat{\Psi}_{\boldsymbol{m},\omega}\rangle).(\hat{\Psi}_{\boldsymbol{m},\omega} - \langle\hat{\Psi}_{\boldsymbol{m},\omega}\rangle)\rangle, \tag{F2}$$

and the mean field obeys

$$\langle\hat{\mathbf{\Psi}}\rangle(T) = \left\langle\hat{\Psi}_{\boldsymbol{m},\omega}\right\rangle. \tag{F3}$$

Since the potential is isotropic, $\langle\hat{\mathbf{\Psi}}\rangle(T)$ is essentially zero (see also Fig. F1), while $\boldsymbol{C}_{\Psi}$ stands for the angular power spectrum described in Section 6.1. Let us call $\{\hat{\mathbf{\Psi}}_{\boldsymbol{m},\omega}(T_i)\}_{i\leqslant N}$, the set of sampled $\hat{\mathbf{\Psi}}$ a fixed slow time, T_i. Relying on a linear interpolation between two such realizations, the corresponding external potential reads in real space

$$\psi^{\rm e}(t,\mathbf{\Omega}) = \sum_i\sum_{\boldsymbol{m}}\int {\rm d}\omega\exp({\rm i}\boldsymbol{m}\cdot\mathbf{\Omega} + {\rm i}\omega t)\,\mathcal{K}_i^{\boldsymbol{m}}(t,\omega), \tag{F4}$$

[5] Note that this assumption is not coherent with the way the measurements are carried, since it implies that the infalling material somehow disappears after crossing R_{200}.

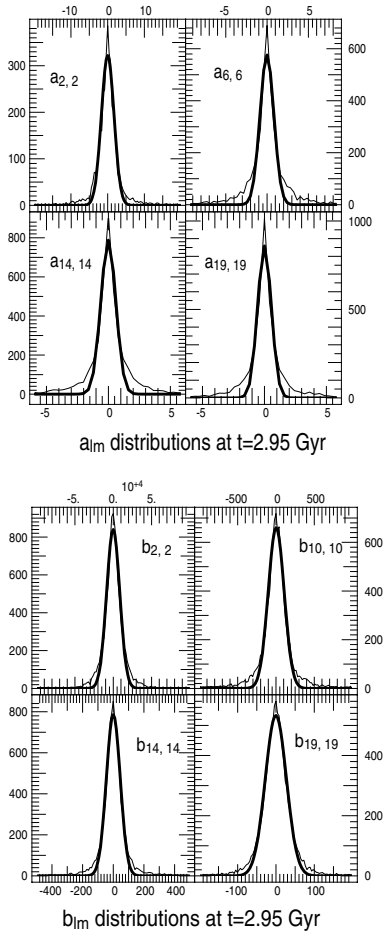

Figure F1. Probing the Gaussianity of the harmonic expansions $a_{\ell m}$, describing the flux density of mass (top) and $b_{\ell m}$, describing the potential $\psi^{\rm e}$ (bottom). Units are arbitrary. Only the real part of the coefficients is shown here, but the imaginary parts have similar distributions. Clearly, the distributions are quasi-Gaussians.

where the kernel, $\mathcal{K}_i^{\boldsymbol{m}}(t,\omega)$, reads

$$\mathcal{K}_i^{\boldsymbol{m}}(t,\omega) = \left[\hat{\Psi}_{\boldsymbol{m},\omega}(T_{i+1})\frac{t-T_i}{T_{i+1}-T_i} + \hat{\Psi}_{\boldsymbol{m},\omega}(T_i)\frac{T_{i+1}-t}{T_{i+1}-T_i}\right] \times\Theta(T_{i+1}-t)\Theta(t-T_i), \tag{F5}$$

recalling that $\Theta(x)$ is the Heaviside function.

To sum up, the computation of $\hat{\Psi}_{\boldsymbol{m},\omega}$ following F1 and F3 ensures that correlations on short periods are reproduced, while the interpolation procedure allows us to take into account the long-period evolution of the field. This procedure can be repeated for an arbitrary number of virtual tidal histories.

F2 Regenerating tidal fields and infall history

Let us assume briefly that the fields are stationary both in time and angle, and that their statistics is Gaussian. As shown in Fig. F1, this assumption is essentially valid for the expansions of the potential and the flux density of mass. Let us call the 11-dimensional vector $\mathbf{\Pi}(t) \equiv (\varpi_\rho, \varpi_{\rho v}, \varpi_{\rho\sigma\sigma}, \psi^{\rm e})$; and $\hat{\mathbf{\Pi}}_{\boldsymbol{m},\omega}$ the temporal and angular Fourier transforms of the fields. The joint probability of the field,

$p(\hat{\mathbf{\Pi}}_{\boldsymbol{m},\omega})$, reads

$$p(\hat{\mathbf{\Pi}}_{\boldsymbol{m},\omega}) = \frac{\exp\left[-\frac{1}{2}(\hat{\mathbf{\Pi}} - \langle\hat{\mathbf{\Pi}}\rangle)^{\top}\cdot\boldsymbol{C}_{\hat{\Pi}}^{-1}\cdot(\hat{\mathbf{\Pi}} - \langle\hat{\mathbf{\Pi}}\rangle)\right]}{(2\pi)^{11/2}\det^{1/2}|\boldsymbol{C}_{\hat{\Pi}}|}, \tag{F6}$$

where

$$\boldsymbol{C}_{\Pi} = \left[\left\langle(\hat{\Pi}^{i}_{\boldsymbol{m},\omega} - \langle\hat{\Pi}^{i}_{\boldsymbol{m},\omega}\rangle)\cdot\left(\hat{\Pi}^{j}_{\boldsymbol{m},\omega} - \left\langle\hat{\Pi}^{j}_{\boldsymbol{m},\omega}\right\rangle\right)\right\rangle\right]_{i,j\leqslant 11} \tag{F7}$$

and

$$\langle\hat{\mathbf{\Pi}}\rangle = \left[\left\langle\hat{\Pi}^{i}_{\boldsymbol{m},\omega}\right\rangle\right]_{i\leqslant 11}. \tag{F8}$$

Since these fields are mostly isotropic, their expansion coefficients are nil on average. Hence, the quantity $\boldsymbol{C}_{\Pi}$ stands for the angular power spectrum of the 11 fields. For, respectively, the potential and the flux density of mass, its *temporal* evolution is described in Sections 6.1 and 6.2. These measured power spectra are sufficient to generate environments restricted to the flux density of mass and the potential. We emphasize that these two fields would not be coherent if no cross-correlations is specified. These cross-correlations and the power spectra for higher moments of the source are postponed to Paper III.

Assuming the full knowledge of these 11 fields and their cross-correlation, it is therefore straightforward to generate for each ($\boldsymbol{m}$, ω) a 11-dimensional vector which satisfies equation (F6), and repeat the draw for all modes (both $\boldsymbol{\omega}$ and $\boldsymbol{m}$). Inverse Fourier transform yields $\Pi(t)$. Once $\Pi(t)$ is known, we can regenerate the whole five-dimensional phase-space source as a function of time via equation (37). This process can also be repeated for an arbitrary number of virtual halo histories. The assumption of stationarity in time can be lifted following the same route as that sketched in Section F1 (see equation F5).

APPENDIX G: FROM EXPANSION COEFFICIENTS TO FLUX DENSITIES

G1 From expansion coefficients to advected momentum

The phase-space distribution of advected momentum is given by

$$\varpi_{\rho v}(\mathbf{\Omega}, v, \mathbf{\Gamma}, t) \equiv s^{\mathrm{e}}(\mathbf{\Omega}, v, \mathbf{\Gamma}, t)\boldsymbol{v} \tag{G1}$$

$$= \sum_{\alpha,\boldsymbol{m},\boldsymbol{m}'} c^{\boldsymbol{m}}_{\alpha\boldsymbol{m}'}(t) g_{\alpha}(v) Y_{\boldsymbol{m}}(\mathbf{\Omega}) Y_{\boldsymbol{m}'}(\mathbf{\Gamma})\boldsymbol{v}, \tag{G2}$$

where the velocity vector may be written as a function of spherical harmonics

$$\begin{aligned}\boldsymbol{v} = &-v\sqrt{\frac{2\pi}{3}}\left[-Y^{*}_{1-1}(\mathbf{\Gamma}) + Y^{*}_{11}(\mathbf{\Gamma})\right]\boldsymbol{e}_{\theta}\\ &-\mathrm{i}v\sqrt{\frac{2\pi}{3}}\left[Y^{*}_{1-1}(\mathbf{\Gamma}) + Y^{*}_{11}(\mathbf{\Gamma})\right]\boldsymbol{e}_{\phi}\\ &v\sqrt{\frac{\pi}{3}}Y^{*}_{10}(\mathbf{\Gamma})\boldsymbol{e}_{\mathrm{r}}.\end{aligned} \tag{G3}$$

Then, one can write

$$\varpi_{\rho v}(\mathbf{\Omega}, t) \equiv \int \mathrm{d}v\mathrm{d}\mathbf{\Gamma} v^2 s^{\mathrm{e}}(\mathbf{\Omega}, v, \mathbf{\Gamma}, t)\boldsymbol{v} \tag{G4}$$

$$= \sum_{\alpha,\boldsymbol{m},\boldsymbol{m}'} [\varpi_{\rho v}]_{\boldsymbol{m}}(t) Y_{\boldsymbol{m}}(\mathbf{\Omega}), \tag{G5}$$

where

$$[\varpi_{\rho v}]_{\boldsymbol{m}}(t) = \sum_{\alpha}\left(3\sigma^2\mu_{\alpha} + \mu^3_{\alpha}\right)\boldsymbol{T}_{\boldsymbol{m}}(t), \tag{G6}$$

and

$$\begin{aligned}\boldsymbol{T}_{\boldsymbol{m}}(t) = &\sqrt{\frac{2\pi}{3}}\left[c^{\boldsymbol{m}}_{\alpha,1,-1}(t) - c^{\boldsymbol{m}}_{\alpha,1,1}t\right]\boldsymbol{e}_{\theta}\\ &+\mathrm{i}\sqrt{\frac{2\pi}{3}}\left[-c^{\boldsymbol{m}}_{\alpha,1,-1}(t) - c^{\boldsymbol{m}}_{\alpha,1,1}t\right]\boldsymbol{e}_{\phi}\\ &+2\sqrt{\frac{\pi}{3}}c^{\boldsymbol{m}}_{\alpha,1,0}(t)\boldsymbol{e}_{\mathrm{r}}.\end{aligned} \tag{G7}$$

G2 From coefficients to advected velocity dispersion

The distribution of advected velocity dispersion is given by

$$\varpi_{\rho\sigma_i\sigma_j}(\mathbf{\Omega}, v, \mathbf{\Gamma}, t) = s^{\mathrm{e}}(\mathbf{\Omega}, v, \mathbf{\Gamma}, t)[\boldsymbol{v} - \boldsymbol{V}(\mathbf{\Omega}, t)]_I[\boldsymbol{v} - \boldsymbol{V}(\mathbf{\Omega}, t)]_j, \tag{G8}$$

where the subscripts i and j stand for r, θ, ϕ and

$$\boldsymbol{V}_i(\mathbf{\Omega}, t) \equiv \frac{\int \mathrm{d}v\,\mathrm{d}\mathbf{\Gamma} v^2 s^{\mathrm{e}}(\mathbf{\Omega}, v, \mathbf{\Gamma}, t) v_i}{\int \mathrm{d}v\,\mathrm{d}\mathbf{\Gamma} v^2 s^{\mathrm{e}}(\mathbf{\Omega}, v, \mathbf{\Gamma}, t)} = \frac{\varpi_{\rho v_i}(\mathbf{\Omega}, t)}{\varpi_{\rho}(\mathbf{\Omega}, t)}. \tag{G9}$$

Using equations (G8) and (G9), we find

$$\begin{aligned}&\varpi_{\rho\sigma_i\sigma_j}(\mathbf{\Omega}, t) + \frac{\varpi_{\rho v_i}(\mathbf{\Omega}, t)\varpi_{\rho v_j}(\mathbf{\Omega}, t)}{\varpi_{\rho}(\mathbf{\Omega}, t)}\\ &\quad= \int \mathrm{d}v\mathrm{d}\mathbf{\Gamma} v^2 s^{\mathrm{e}}(\mathbf{\Omega}, v, \mathbf{\Gamma}, t) v_i v_j \qquad \text{(G10)}\\ &\quad= \sum_{\boldsymbol{m}} [\boldsymbol{q}_{ij}(t)]_{\boldsymbol{m}} Y_{\boldsymbol{m}}(\mathbf{\Omega}). \qquad \text{(G11)}\end{aligned}$$

The six independent elements of the symmetric tensor $\boldsymbol{q}(t)$ can be computed from $c^{\boldsymbol{m}}_{\alpha\boldsymbol{m}'}(t)$ coefficients using equation (G3) and recalling that

$$\begin{aligned}\int \mathrm{d}\mathbf{\Omega} Y_{\ell_1,m_1} Y_{\ell_2,m_2} Y_{\ell_3,m_3} = &\sqrt{\frac{(2\ell_1+1)(2\ell_2+1)(2\ell_3+1)}{4\pi}}\\ &\times\begin{pmatrix}\ell_1 & \ell_2 & \ell_3\\ 0 & 0 & 0\end{pmatrix}\begin{pmatrix}\ell_1 & \ell_2 & \ell_3\\ m_1 & m_2 & m_3\end{pmatrix},\end{aligned} \tag{G12}$$

where $\begin{pmatrix}\ell_1 & \ell_2 & \ell_3\\ m_1 & m_2 & m_3\end{pmatrix} = W^{\ell_1,\ell_2,\ell_3}_{m_1,m_2,m_3}$ is the Wigner 3j symbol. One can find

$$\begin{aligned}[\boldsymbol{q}_{rr}(t)]_{\boldsymbol{m}} =&\sum_{\alpha\boldsymbol{m}'}\mathcal{H}^{\boldsymbol{m}}_{\alpha\boldsymbol{m}'}(t) 2W^{11\ell'}_{000}W^{11\ell'}_{00m'}\\
[\boldsymbol{q}_{r\phi}(t)]_{\boldsymbol{m}} =&\sum_{\alpha\boldsymbol{m}'}\mathcal{H}^{\boldsymbol{m}}_{\alpha\boldsymbol{m}'}(t)\mathrm{i}\sqrt{2}W^{11\ell'}_{000}\left(W^{11\ell'}_{1-1m'} + W^{11\ell'}_{11m'}\right)\\
[\boldsymbol{q}_{r\theta}(t)]_{\boldsymbol{m}} =&\sum_{\alpha\boldsymbol{m}'}\mathcal{H}^{\boldsymbol{m}}_{\alpha\boldsymbol{m}'}(t)\sqrt{2}W^{11\ell'}_{000}\left(W^{11\ell'}_{1-1m'} - W^{11\ell'}_{11m'}\right)\\
[\boldsymbol{q}_{\phi\phi}(t)]_{\boldsymbol{m}} =&\sum_{\alpha\boldsymbol{m}'}\mathcal{H}^{\boldsymbol{m}}_{\alpha\boldsymbol{m}'}(t)(-1)W^{11\ell'}_{000}\left(W^{11\ell'}_{11m'} + 2W^{11\ell'}_{1-1m'} + W^{11\ell'}_{-1-1m'}\right)\\
[\boldsymbol{q}_{\phi\theta}(t)]_{\boldsymbol{m}} =&\sum_{\alpha\boldsymbol{m}'}\mathcal{H}^{\boldsymbol{m}}_{\alpha\boldsymbol{m}'}(t)\mathrm{i}W^{11\ell'}_{000}\left(W^{11\ell'}_{-1-1m'} - W^{11\ell'}_{11m'}\right)\\
[\boldsymbol{q}_{\theta\theta}(t)]_{\boldsymbol{m}} =&\sum_{\alpha\boldsymbol{m}'}\mathcal{H}^{\boldsymbol{m}}_{\alpha\boldsymbol{m}'}(t)W^{11\ell'}_{000}\left(W^{11\ell'}_{11m'} - W^{11\ell'}_{-1-1m'} - 2W^{11\ell'}_{1-1m'}\right),\end{aligned} \tag{G13}$$

where $\mathcal{H}^{\boldsymbol{m}}_{\alpha\boldsymbol{m}'}(t) = \sqrt{4\pi(2\ell'+1)}(6\sigma^2\mu^2_{\alpha} + \mu^4_{\alpha})c^{\boldsymbol{m}}_{\alpha\boldsymbol{m}'}(t)$.

APPENDIX H: NOTATIONS

Table H1. A summary of the notations used throughout the paper.

Symbol	Meaning
$(\boldsymbol{r}, \boldsymbol{v})$	Position and velocity
t, τ	Lookback time variables
R_{200}	Virial radius measured at $z = 0$
$V_{\rm c}$	Circular velocity measured at R_{200}
F	The phase-space DF of the halo
ψ	The self-gravitating potential
$\psi^{\rm e}$	The external potential, induced by external perturbations
$s^{\rm e}$	The source function in phase space
ϖ_x	The flux density of x
ϖ_ρ	The flux density of mass
$\varpi_{\rho\boldsymbol{v}}$	The flux density of momentum
$\varpi_{\rho\sigma\sigma}$	The flux density of velocity dispersion
$\psi^{[n]}(\boldsymbol{r})$	3D projection basis of the potential
$\phi^{[n]}(\boldsymbol{r})$	6D projection basis of the source term
$\boldsymbol{a}(t)$	Expansion coefficients of the potential/density response
$\boldsymbol{b}(t)$	Expansion coefficients of the external potential perturbation
$\boldsymbol{c}(t)$	Expansion coefficients of the source perturbation
$\boldsymbol{\Omega}$	Angular position on the virial sphere (two angles)
$\boldsymbol{\Gamma}$	Angular orientation of the velocity vector on the virial sphere (two angles)
v	Velocity's amplitude
$\bar{X}$	Angular average of X
$\underline{\rm X}$	Temporal average of X
$\langle X \rangle$	Statistical expectation (or average value) of X
$\langle\!\langle X \rangle\!\rangle$	Most probable value (or mode) of X
$\delta_{[X]}(\boldsymbol{\Omega})$	Contrast density of X measured on the virial sphere
$\boldsymbol{m} = (\ell, m)$	Harmonic coefficients related to $\underline{0}$
$\boldsymbol{m}' = (\ell', m')$	Harmonic coefficients related to $\boldsymbol{\Gamma}$
$a_{\ell,m}(t)$	Harmonic expansion coefficients of $\delta_{[\varpi_\rho]}$
$b_{\ell,m}(t)$	Harmonic expansion coefficients of $\delta_{[\psi^{\rm e}]}$
$C_\ell(t)$	Angular power spectrum
$T_\ell(t, t + \Delta t)$	Angular-temporal power spectrum
$w(\theta, t, t + \Delta t)$	Angulo-temporal correlation function measured on the sphere for an angulo-temporal separation θ and Δt
$\Phi^{\rm M}(t)$	Accretion rate measured at the virial radius (averaged over all directions)
$\vartheta(\Gamma_1, t)$	PDF of the velocity's incidence angle
b	Impact parameter
$\varphi(v, t)$	PDF of the velocity's amplitude
$\wp(v, t)$	Joint PDF of the velocity's incidence angle and amplitude

This paper has been typeset from a TEX/LATEX file prepared by the author.